TÉCNICO LISBOA

Numerical Implementation of a Frequency-Domain Panel Method for Flutter Prediction of a 3D Wing

Eduardo Manuel Pizarro Gomes Pepe

Thesis to obtain the Master of Science Degree in

Aerospace Engineering

Supervisor: Prof. Afzal Suleman

Examination Committee

Chairperson: Prof. Fernando José Parracho Lau
Supervisor: Prof. Afzal Suleman
Members of the Committee: Prof. André Calado Marta

April 2015

"When everything seems to be going against you, remember that the airplane takes off against the wind, not with it"

Henry Ford

ABSTRACT

Within the field of linear methods for aeroelastic flutter prediction, the Doublet Lattice Method (DLM) and the Strip-Theory are considered standard methodologies. These methods are formulated in the convenient frequency domain, thus allowing computationally efficient solution techniques to extract the aeroelastic system's eigenvalues and infer about its dynamic stability.

Panel methods are based on potential aerodynamic theory and offer greater capability to model complex 3D surfaces, thickness effects, and allow unconstrained surface discretization schemes. However, Panel Methods are seldom applied to flutter analysis since, in general, they are formulated in the time-domain. L. Morino presented a frequency-domain integral solution for the linearized compressible aerodynamic potential equation which constituted the foundations of a unique frequency-domain panel method.

In this thesis, this frequency-domain panel method has been implemented in a MATLAB® environment as part of an in-house aeroelastic design tool specialized in the flutter prediction of 3D cantilever wing structures. A large portion of the work is focused on the implementation aspects and numerical studies concerning convergence and computational efficiency. The modified p-k method is based on the original p-k method and has been developed in order to enforce physical consistency and to increase the accuracy in the process of extracting the system's eigenvalues. The linear flutter analysis of a high-aspect-ratio wing has been performed for validation purposes. While the work completed constitutes a full implementation of the panel method in the frequency domain, the results have shown large discrepancies that require further validation and evaluation of the proposed numerical tool.

Keywords: aeroelastic flutter, potential aerodynamics, panel method, frequency-domain, p-k method

RESUMO

Dentro do campo das teorias lineares para o cálculo de flutter aeroelástico, a *Doublet Lattice Method* (DLM) e a *Strip-Theory* são consideradas metodologias convencionais. O facto de serem formuladas no domínio da frequência permite que métodos eficientes a nível computacional sejam aplicados para extrair os valores próprios do sistema aeroelástico e de seguida concluir acerca da estabilidade dinâmica do mesmo.

Os métodos de painel são alicerçados na teoria aerodinâmica potencial e superam as metodologias convencionais na modelação de superfícies 3D, inclusão de efeitos de espessura e maior liberdade na discretização das superfícies. Sendo geralmente formulados no domínio do tempo, os métodos de painel praticamente não são aplicados em análises de flutter. L. Morino apresentou uma solução integral para a equação potencial compressível linearizada, que constitui o ponto de partida para um método de painel único, formulado no domínio da frequência.

Nesta dissertação, este método de painel foi implementado em ambiente MATLAB® como parte integrante de um programa especializado na previsão de flutter de uma asa 3D. Uma grande parte do trabalho foca-se na implementação do programa e em estudos paramétricos relacionados com convergência numérica e eficiência computacional. O método p-k modificado baseia-se no método p-k original e foi desenvolvido com o propósito de melhorar o processo de extração de valores próprios, nomeadamente a nível da consistência física e da precisão dos resultados. A fim de validar o programa, realizou-se um estudo de flutter linear de uma asa de elevada razão de aspeto. Apesar do trabalho representar uma implementação completa de um método de painel no domínio da frequência, os resultados revelaram elevada discrepância numérica, sugerindo uma reavaliação e subsequente nova validação da ferramenta numérica.

Palavras-chave: flutter aeroelástico, aerodinâmica potencial, método de painel, domínio da frequência, método p-k

TABLE OF CONTENTS

LIST OF FIGURES

LIST OF TABLES

LIST OF ACRONYMS

2D: two-dimensional

3D: three-dimensional

AIC: Aerodynamic Influence Coefficient

AR: Aspect Ratio

CAE: Computational Aeroelasticity

CFD: Computational Fluid Dynamics

CSD: Computational Solid Dynamics

DLM: Doublet Lattice Method

DoF(s): Degree(s)-of-Freedom

FEM: Finite Element Method

FSI: Fluid Structure Interaction

HALE: High-Altitude-Long-Endurance

LCO: Limit Cycle Oscillations

POD: Proper Orthogonal Decomposition

ROM: Reduced Order Method

LIST OF SYMBOLS

a_∞ : Free-stream speed of sound

a : Local speed of sound

$[A]$: Aerodynamic DoFs – unsteady pressure matrix

$\{A\}$: Real part of $\{V\}$

$[AIC]$: Aerodynamic influence coefficients' matrix

$[AIC_R]$: Real part of $[AIC]$

$[AIC_I]$: Imaginary part of $[AIC]$

$\{B\}$: Imaginary part of $\{V\}$

$[B], B_{ij}$: Source influence coefficients' matrix

c : Wing's mean chord

C : Theodorsen's Function

$[C]$: Damping matrix, doublets influence coefficients matrix

C_{ij} : Doublet influence coefficients' matrix

$\mathbf{d}$: Aerodynamic displacement vector

(d_x, d_y, d_z) : Cartesian components of the aerodynamic displacement vector $\mathbf{d}$

$\mathbf{d'}$: Aerodynamic rotation vector

$\left(\frac{\partial d_x}{\partial x}, \frac{\partial d_y}{\partial x}, \frac{\partial d_z}{\partial x}\right)$: Cartesian components of the aerodynamic rotation vector $\mathbf{d'}$

$\frac{D_c}{Dt}$: Substantial derivative

$\frac{d}{dt}$: Small-perturbation substantial derivative

D_{ik} : DoFs matrix

E : Panel method surface parameter

EI_{xx} : Spanwise bending rigidity

EI_{zz} : Chordwise bending rigidity

F : Non-linear function

$\{\tilde{F}_n\}$: Unsteady aerodynamic normal force vector

$\{\tilde{F}\}$: Unsteady aerodynamic force vector

$\{f_A\}, \{F\}$: Generalized aerodynamic force vector

G : Green's function

GJ : Torsional rigidity

h : Vertical displacement of the elastic axis (DoF)

$\bar{h}$: Unsteady amplitude of the vertical displacement h

$[I]$: Identity matrix

I_α : Wing's cross section moment of inertia

J : Wing's cross section torsion constant, Jacobian

k : Reduced frequency

$[K]$: Stiffness matrix

L : Equivalent beam's length, wing's semi-span

$\overline{\Delta L}$: Unsteady amplitude of the lift per unit span

$[M]$: Mass matrix

M_∞ : Free-stream Mach number

M_F : Flutter Mach number

$\overline{\Delta M}$: Unsteady amplitude of the pitching moment per unit span

n : Exterior surface normal direction

n_0 : Transformed surface normal n

N_B : Number of wing panels

N_W : Number of wake panels

p : Non-dimensional complex eigenvalue, local pressure

p_∞ : Free-stream pressure

$\tilde{p}$: Unsteady amplitude of the pressure p

$\hat{p}$: Transformed unsteady amplitude of the pressure p

p_S : Steady part of the pressure p

Δp : Local pressure difference at surface

$\Delta\tilde{p}_{wake}$: Unsteady perturbation pressure difference across wake

$[P]$: Transformed potential – unsteady pressure matrix

$\{q\}$: Vector of DoFs

$\{\tilde{q}\}$: Vector of unsteady amplitudes of $\{q\}$

$\{\hat{q}\}$: Transformed vector of unsteady amplitudes of $\{q\}$

$\{\tilde{q}_A\}$: Vector of unsteady amplitudes of aerodynamic DoFs

$\{\tilde{q}_S\}$: Vector of unsteady amplitudes of structural DoFs

Q_i : Generalized aerodynamic force for DoF i

Q_n : Normal perturbation velocity

$Q_{n,S}$: Steady part of Q_n

$Q_{n,U}$: Unsteady part of Q_n

$\tilde{Q}_n$: Unsteady amplitude of Q_n

$\hat{Q}_n$: Transformed unsteady amplitude $\tilde{Q}_n$

r_β : Hyperbolic radius

r_0 : Transformed hyperbolic radius r_β, distance between two control points

$[R]$: Aerodynamic force rotation matrix

s : Dimensional complex eigenvalue

s_0 : Transformed variable s

S : Surface function

$[S]$: Panels' area matrix

S_0 : Transformed surface function S

S_α : Inertial coupling integral

S_{B0} : Transformed wing surface function

ΔS : Unsteady deviation of the surface S

S_S : Steady part of S

S_U : Unsteady part of S

S_{W0} : Transformed wake surface function

[T] : DoFs transformation matrix

T : Retarded time, Kinetic energy

Δt : Time-step

U_∞ : Free-stream air speed

U_F : Flutter speed

V : Potential energy

V : Local airflow speed vector

{V} : Eigenvector of the flutter equation

{V^*} : Complex conjugate of {V}

$\overline{w}$: Unsteady amplitude of w_a

w_a : Downwash at airfoil

W_{NC} : Work of non-conservative forces

(x, y, z) : Global Cartesian coordinates

(x_1, y_1, z_1) : Global Cartesian integration coordinates

(x_0, y_0, z_0) : Transformed global Cartesian coordinates

(x_{01}, y_{01}, z_{01}) : Transformed global Cartesian integration coordinates

$x_{0_{wake}}$: Transformed x coordinate of a control point in a wake panel

$x_{0_{TE}}$: Transformed x coordinate of the trailing edge panel control point

z_a : Vertical displacement of airfoil

Greek letters:

α : Angle-of-attack, angular displacement about Y axis (DoF)

$\overline{\alpha}$: Unsteady amplitude of the angular displacement α

β : Mach number factor, Newmark's scheme stability parameter

γ : Aeroelastic damping, Newmark's scheme stability parameter

δ : Dirac's delta, exponential grow/decay

ε : Perturbation's amplitude

Λ : Leading edge sweep angle

ρ_∞ : Free-stream air density

Φ : Velocity potential

φ : Perturbation velocity potential, shape function

$\tilde{\varphi}$: Unsteady amplitude of φ

$\hat{\varphi}$: Transformed unsteady amplitude $\tilde{\varphi}$

φ_S : Steady part of φ

$\Delta\hat{\varphi}_{TE}$: $\Delta\hat{\varphi}_{wake}$ at the trailing edge

$\Delta\tilde{\varphi}_{wake}$: Unsteady amplitude difference of φ across the wake

$\Delta\hat{\varphi}_{wake}$: Transformed $\Delta\tilde{\varphi}_{wake}$

ω : Circular frequency of oscillations

ω_0 : Transformed circular frequency ω

ω_f : Flutter frequency of oscillations

Program variables:

"k_freq" : Active reduced frequency

"n_panels" : Total number of panels

"n_wake" : Number of panels in the wake

"nseg_wake" : Number of panels in the free-stream direction on the wake

"nseg_X" : Number of panels in the chordwise direction (one side)

"nseg_Y" : Number of panels in the spanwise direction, number of structural nodes

1 INTRODUCTION

Aeroelastic flutter is a physical phenomenon characterized by the non-sustained vibration of a structure due to its interactions with the surrounding fluid flow. In lifting surfaces, such as airplane wings, the mechanism of flutter involves a positive feedback between the wing's deflections and the forces exerted by the fluid flow. Since these deflections result from the aerodynamic forces, the oscillatory behavior is self-excited and, unless some sort of non-linearity bounds the motion, the vibration amplitudes will continuously increase until the eventual structural failure. For this reason, aeroelastic flutter is classified as a type of dynamic instability. Flutter is more prone to develop in very flexible structures and usually requires some kind of initiation mechanism such as local perturbations induced by flying maneuvers or turbulence. Its destructive effects on structures, in particular aircrafts, had led to several tests and studies focusing on determining the flutter speed, the minimum flying speed above which flutter is predicted to occur. Due to the hazards of flutter testing, most of today's research involves developing and implementing efficient numerical methods known as the Computational Aeroelasticity (CAE) codes. These numerical techniques couple Computational Fluid Dynamics (CFD) and Computational Solid Dynamics (CSD) codes in order to track or detect the onset of flutter instability. Despite the multidisciplinary nature of flutter, the main effort has been toward the improvement of the unsteady aerodynamic models. These are responsible for the complex self-feeding mechanisms involved and, because of its intrinsic nonlinear character, the aerodynamic models are still an active field of research.

2 BIBLIOGRAPHICAL REVIEW

2.1 HISTORICAL REVIEW

Flutter has been affecting aircrafts since the early aviation years at the beginning of the past century [1]. The first known flutter occurrence was documented in 1916 by F. W. Lanchester [2] after observing violent antisymmetric oscillations in the fuselage and tail of the Handley-Page 0/400 biplane bomber. Before knowing the true origin of the problem, Lanchester claimed that the oscillations were not the result of resonance induced vibratory sources but were self-excited instead. Later, Bairstow and Fage provided analytical backup for the investigation in a paper [3] that was considered the first flutter analytical analysis, and confirmed Lanchester's conclusions. The analysis consisted in a stability analysis of a binary model using the twisting of the fuselage and deflection of the elevators as degrees-of-freedom (DoFs), while quasi-steady, frequency independent, aerodynamic derivatives were used for modelling the lifting forces. In the 1920s, similar unstable oscillations began to be recognized as a matter of concern within the aircraft community, which led to several investigations. For instance, von Baumhauer and Koning in 1923 [4] proceeded with an experimental and theoretical investigation of a long distance reconnaissance monoplane following severe aileron flutter. Using similar binary models, they concluded that modifying the inertial proprieties (mass balancing) in the aileron region could eliminate the problem. The study was successfully verified by wind tunnel and flight tests and the concept of mass balancing became the standard aircraft modification for preventing flutter.

2.1.1 Aerodynamic Theories

In the following year (1924), Birnbaum [5] makes the first contribution towards the modeling of the unsteady aerodynamic effects on airfoils in 2D flows. In his model, the wing was essentially an infinite flat plate immersed in a steady, incompressible potential flow. The unsteady effects were modeled by placing vortex singularity lines of harmonically oscillating strengths in the airfoil and wake regions. The solution featured an integral relation between the pressure difference and the normal velocity but it could not be evaluated analytically. Although Birnbaum was able to express the numerical solution using a series expression in terms of the reduced frequency "k", his results had serious convergence problems for k > 0,1. After Birnbaum, some important contributions followed, namely the ones by Wagner [6] and Glauert [7]. However, the first major contribution in 2D unsteady aerodynamics for flutter calculations was achieved by Theodorsen [8] in 1934. He presented a succinct theory of the 2D oscillating flat plate undergoing translation, torsion and aileron-type motions and derived the sectional lift and moment formulas in terms of the plate's DoFs and the reduced frequency. These formulas were essentially the same as in quasi-steady aerodynamics, but with additional terms accounting for the inertial effects (non-circulatory part) and the unsteady wake (circulatory part). The circulatory part involves the special function C(k), known as the Theodorsen's Function, which basically accounts for the lags between the airfoil motion and the aerodynamic forces, caused by the influence of the wake. Since Theodorsen's Function can be evaluated exactly by means of tabulated Bessel functions, this theory was remarkably the simplest exact theory available for the idealized flat plate airfoil performing harmonic oscillations and

for long years it was the standard aerodynamic model for flutter calculations. Theodorsen's theory is often referred as the "Strip Theory" [9] because of its systematic application to a full 3D wing discretized by several spanwise "strips". In the Strip Theory, the sectional lift and moment for each strip are calculated using Theodorsen's formulas, and the structure (usually a beam), is modeled by the classic elasticity formulas in terms of the bending and torsion DoFs. Then, for instance, the Rayleigh-Ritz method can be applied to the wing in order to obtain the equations of motion.

With the increase of aircraft speed in the mid-30s, the compressibility effects in flight were becoming relevant and incompressible theories could no longer accurately predict the pressure field over the lifting surfaces. In the branch of the linear, small-perturbations unsteady potential aerodynamics, Prandtl [10] introduced the concept of acceleration potential, in contrast to the usual velocity potential. The acceleration potential is proportional to the local aerodynamic pressure difference at the surface. The use of this concept allows a simplification in the definition of the unsteady wake because, as the wake does not sustain forces, the acceleration potential vanishes there. Based on Prandtl's work, Possio [11] developed a new theory, possibly the first compressible aerodynamic theory aimed at flutter calculations. He applied Prandtl's acceleration potential to the 2D unsteady problem and arrived at an integral equation (Possio's equation), the solution of which gives the loading over a flat plate airfoil in an airstream, for a known motion of the plate (i.e., for a given downwash).

Kussner [12] in 1941, developed an aerodynamic theory that would set the basis for most of the modern flutter calculations. He formulated the first general lifting surface theory, valid within the linear subsonic potential flow. Using the concept of moving singularities (doublets), Küssner was able to express the normal velocity at the wing for every instant in time, in terms of an integral over the wing that was considered a flat surface. The integrand involved the product of the local pressure difference and a function known as the "Subsonic Kernel Function". However, the Kernel was written as a singular integral and could only be evaluated approximately using inefficient numerical techniques. An explicit formula for the Kernel was obtained several years later in 1954 by Wollston *et al* [13], after restricting Kussner's formulation to harmonic oscillations.

The systematic application of lifting surface theories to actual wings became feasible with the improvement of digital computers in the 50s. An early approach was known as the Kernel Function Method [14] and consisted in approximating the pressure in the integral formula by a series expansion of unknown coefficients. These coefficients were related to the known downwash at a number of points equal to the number of terms retained in the series, producing a set of linear algebraic equations. This required choosing a function such that the wing edge conditions (Kutta condition) were satisfied. The Kernel Function Method would eventually lose its popularity with the advent of the Doublet Lattice Method (DLM) in 1968 by Rodden *et al* [15]. The DLM is essentially the conversion of the subsonic theory developed by Küssner to an aerodynamic finite element method. Each element is a portion of the wing surface (quadrilateral box) in which two of its sides are aligned with the incoming flow. Each box contains a control point at ¾ chord, and a distribution of doublets along the ¼ chord line, whose unknown strengths are proportional to the surface pressure. The pressure difference and downwash are assumed constant at each box and their value is assigned to the respective control point. The

relation between downwash and pressure is given by the integral of the subsonic kernel along the doublet line. Computationally, such relation is written in terms of a square matrix called the influence coefficient matrix, with as many rows as the number of boxes in the wing:

$$w_i = D_{ij}\Delta p_j \qquad (1)$$

In the derivation of matrix D, Rodden used the harmonic subsonic Kernel derived by Vivian and Andrew [16] – which was an extension of the work by Woolston *et al.* [13] for non-planar surfaces – so that the actual DLM could be applied to complex aircraft surfaces. Within the frame of linear aerodynamics, the DLM is the most sophisticated aerodynamic theory for aircraft flutter prediction and has been used extensively in the literature and industry until today. For instance, it is the default aerodynamic theory used by the commercial software MSC NASTRAN [17] for predicting the flutter speed.

An alternative methodology for calculating the aerodynamic loads in slender bodies performing an arbitrary motion are the Panel Methods [18] [19]. These methods are also based on linear potential theory and share some aspects with the lifting surface methods, like the distribution of singularities, however they differ in the formulation and implementation aspects. The main differences reside in the arbitrary discretization process (paneling), collocation method and the possibility of modeling 3D closed surfaces. Although they are seldom used for flutter calculations, there has been some successful flutter studies using this method. A possible cause for their lack of popularity towards flutter calculations is their restriction to steady and time-domain unsteady formulations. For instance, Jones *et al.* [20] used an unsteady panel method for measuring the time dependent oscillations of both single and two-airfoil systems under incompressible, inviscid flow. The structural model consisted in an elastic spring supporting both translational and rotational stiffness. After the unstable, growing oscillatory behavior have been detected (flutter), the results were compared with equivalent frequency domain studies showing good agreement. In addition, it has was shown that flutter of a trailing airfoil can be controlled by proper oscillation and phasing of a leading edge airfoil.

2.1.2 Aeroelastic Solutions

In theory, the general aeroelastic problem can be written as a system of partial differential equations in space and time, featuring the relations between inertial, structural and aerodynamic forces. The explicit form of the aeroelastic equations depends on the theories involved for modeling both structural and aerodynamic forces. Since, by practical and historical reasons, these contributions have been formulated independently, there isn't a single unified aeroelastic theory. The usual approach is to resort to energy methods and the concept of generalized displacements for space discretization in order to realize the aeroelastic system of equations:

$$[M]\{\ddot{q}\} + [C]\{\dot{q}\} + [K]\{q\} = \{f_A(t)\} \qquad (2)$$

The matrices M, C and K are the structural mass, damping and stiffness matrices respectively and can be computed using Finite Element Method (FEM) or the Rayleigh-Ritz method [21]. The vector f_A contains the contribution of the aerodynamic forces at each structural node at each instant of time, and the vector q contains the several DoFs. Both structural and aerodynamic quantities above depend on

the respective theories which can be either linear or nonlinear. In general, equation (2) is solved for several instants in time using time marching techniques such as the Runge-Kutta [22] scheme or the Newmark [23] algorithm. Doing so requires setting an initial displacement field and determining the structural matrices and aerodynamic force vector at each time step. This is the time-domain formulation of the equilibrium equations and its general form is compatible with any aeroelastic problem.

Historically, the flutter analyses have been formulated in the frequency domain by assuming simple harmonic motion of the wing $\{q\} = \{\bar{q}\}e^{i\omega t}$. In conjunction with linear theories, this approach leads to a system of homogeneous equations that can be solved by obtaining the eigenvalues of the system and then the stability of the system is inferred from them. Such procedure is possible because of the linear theories involved in the analysis. It is also a more convenient approach in comparison to general time domain formulations due to its lower computational costs. In these conditions, the aeroelastic equilibrium equations take the following generic form [24]:

$$\left[\left(\frac{U_\infty}{c}\right)^2 [M]p^2 + \left(\frac{U_\infty}{c}\right)[[C] - [AIC_I(p, M)]]p + [K] - [AIC_R(p, M)] \right]\{\bar{q}\} = 0 \qquad (3)$$

This equation consists in an eigenvalue problem in p and defines the system's stability equation or simply the "flutter equation". Here, $p = k(\gamma + i)$ is the dimensionless complex frequency with $k \equiv \omega c/U_\infty$ being the reduced frequency and $\gamma \equiv Re\{p\}/k$ the damping coefficient of the oscillatory movement. The aerodynamic force is written in terms of the DoFs via the Aerodynamic Influence Coefficient's matrix (AIC): $f_A(t) = [AIC]\{q\}$. In general, this is a complex matrix with $[AIC_R] = Re\{[AIC]\}$ and $[AIC_I] = Im\{[AIC]\}$ that depends on the complex frequency and Mach number. The AIC matrix is computed by the chosen aerodynamic theory after a proper force transfer and DoF conversion from the aerodynamic nodes to the structural ones. This can be accomplished by simple methods such as the Rigid Body Attachment [25] or more sophisticated ones such as the spline mapping methods. The latter method includes the Infinite Beam Spline [25] and the Thin Plate Spline [25] [26], depending on whether the DoFs are being transferred to a structural beam or plate.

The flutter equation (3) can seldom be solved as a standard eigenvalue problem because the aerodynamic force is usually a non-linear function of the complex frequency "p". If the AIC matrix is a simple function of "p", as in the case of quasi-steady aerodynamics [9], the solution can be obtained by finding the roots of the determinant. This is known as the p-method [27] and it is exact from the mathematical point of view. In most cases, however, the aerodynamic model is only available for simple harmonic motion ($\gamma = 0$) which means that the AIC matrix is restricted to values of the reduced frequency "k". Initially, in order to avoid improper formulations, simple harmonic oscillations ($p = ik$) used to be imposed on the structural part and the problem had been reduced to a non-linear eigenvalue problem in the reduced frequency alone. Since this approach does not directly generates damping in the system, an artificial damping "g" was introduced in the system as an external structural damping force. Based on experimental tests, the damping force has been assumed proportional to the amplitude but in phase with the velocity $D \propto g * i\bar{h}e^{i\omega t}$. The solution is obtained in the iterative process of solving

for "g" given "k", for several speeds, until the flutter boundary is reached, i.e., "g" = 0. This procedure is called the k-method and was originated in the 40s, following the Strip Theory. An early description of the method is found on a report by Scanlan & Rosenbaum [28] and a good and recent explanation is given in the book by Hodges & Pierce §5.4.1 [27].

While the k-method is still popular today for its speed, it is known to exhibit an improper coupling among the modes, especially in the vicinities of the flutter boundary. Such behavior is often attributed to the artificial damping introduced in its formulation. In 1971, Hassig [29] was able to show this erroneous behavior by applying the k-method in a simple flutter study of a wing and then by applying the exact p-method for comparison. In the attempt of eliminating the artificial damping and at the same time include more accurate aerodynamics, Hassig conducted a p-method type of analysis with the restriction that the AIC matrix was for harmonic motion. Although mathematically inconsistent, the results obtained were approximately the same as with the p-method which provided great credibility towards the new methodology. The method was called "p-k-method" after the mixture of p and k parameters featuring in the flutter equation. The solution can be found by guessing a reduced frequency "k" and solving iteratively the quadratic eigenvalue problem in "p" until $Im\{p\} = k$. The process is repeated for all the relevant eigenvalues and for several speeds until the flutter boundary is reached $Re\{p\} = 0$. The p-k-method is considered the standard solution methodology for solving the flutter equation formulated in the frequency domain and it is currently used nowadays in CAE software such as MSC NASTRAN® [17] and ZAERO® [25].

2.2 State of the Art

The modern aeroelastic field of research is focused on studying the effects of both structural and aerodynamic nonlinearities on the structure's dynamic response. Structural nonlinearities are present whenever large displacements are allowed which is often the case of high aspect ratio wings. On the other hand, aerodynamic nonlinearities are present outside the scope of small perturbations assumption, such as transonic and hypersonic flight regimes, or in the most general flow regime where vorticity and viscosity are included. Nonlinear aircraft flutter is currently an active topic of research. The computational resources available today allow full nonlinear, time domain aeroelastic theories to be successfully applied for virtually any configuration, instead of the classical and linear frequency domain approaches. As a result, the understanding of flutter grew considerably in the past 20 years. Its concept became less restricted to the mathematical point of view of unstable eigenvalues and more attached to the instability mechanisms of newfound nonlinear phenomena such as the Limit Cycle Oscillations (LCO).

Patil and Hodges [30] modeled the structural nonlinearities in an aeroelastic analysis of a HALE aircraft. They conducted a linear stability analysis about a deformed trim state using nonlinear beam theory for the structure and a linear aerodynamic theory for the external forces. After comparing with the usual linear flutter analysis, it was clear that, when large deformations are present, the aeroelastic modes and frequencies were significantly altered leading to lower flutter speeds. It was shown in a similar study [31] that in terms of steady state calculations, there is negligible difference between the airloads calculated

using the correct non-planar wing geometry as compared to loads assuming an undeformed, planar wing. However, the differences are critical concerning the dynamic behavior of the wing. The aerodynamic induced wing curvature significantly alters the dynamic proprieties of the structure such as the stiffness and mass distribution, leading to a change of the flutter speed by more than 50%.

Xie and Yang [32] further studied HALE aircrafts in a slightly more sophisticated study where the structural model was a 2D flat plate and the aerodynamics were modeled by the DLM. Both linear and nonlinear flutter analysis were conducted. In the pre-flutter static nonlinear analysis, they used the true normal pressure forces (follower forces) on the deformed body instead of the usual normal forces to the undeformed wing plane used in linear analysis. In comparison with the linear analysis, it was shown that the geometrical nonlinearity induced by the large structural deformation leads to the motion coupling of the wing chordwise bending and the torsion, which resulting in different mode frequencies and shapes. As a consequence, the aeroelastic coupling of the flexible modes is altered leading to the decrease of the flutter speed. In this sense, the author justifies the use of nonlinear models for flutter prediction when very flexible structures are concerned.

In the last decade, there is a growing interest in developing aeroelastic analysis in the transonic flight speeds that typically occur around Mach 0.8-1.2. Bendiksen [33] investigated the effects of nonlinearities on a generic swept wing at high altitudes and at transonic Mach numbers. In his analysis, the aerodynamics were modeled by the Euler equations discretized by the Galerkin method and the structure was modeled by the Reissner-Mindlin nonlinear finite element plate theory. Proceeding with a Runge-Kutta time marching scheme, Bendiksen obtained the onset of flutter at Mach 0.84 and subsequent grow of oscillations until Mach 0.95 where they would start to decrease with time. In his study, these oscillations are mentioned as LCO and are considered a type of nonlinear flutter. Since the growing oscillations do not occur below the critical Mach number, the author concludes that the nature of observed unstable LCO must be due to the transonic flight regime.

Some researchers go even beyond the inviscid fluid models and perform full viscous analysis for flutter boundary determination. Gao [34] successfully validated the experimental AGARD 445 wing flutter tests at transonic speeds using a fully coupled, aeroelastic theory in a time marching procedure. The structure was a thin plate discretized by linear finite plate elements, and the fluid was modeled by the RANS equations discretized by several 3D control volumes. Since the structural and aerodynamic meshes were non-point matching, spline techniques were used to interpolate displacement data from one grid to another. The solution procedure required calculating the steady deformed shape at a certain speed and then the unsteady calculations were initiated by introducing a perturbation displacement field based on a certain natural mode. Each time step contained several iterative sub-steps in order to deform the structural mesh according to the aerodynamic forces. Gao neglected the structural damping and resorted to the Newmark algorithm for advancing in time, using time steps as small as 0,0004 seconds. For each Mach, the flutter boundary was found whenever the flutter speed index $V_f = \frac{U_\infty}{C_r \omega_f \sqrt{\mu}}$ provided approximately neutrally stable oscillations, i.e., the onset on instability. In a plot depicting the flutter

speed index versus the Mach number ranging from 0.499 to 1.141, the calculated results were compared with the experimental ones and were in good agreement.

There is currently a trend toward developing high-fidelity methods at a substantially lower computational cost. One approach is to linearize the structural and aerodynamics equations about a steady state, and then to convert the equations to the frequency domain. The flutter boundary is calculated by eigenvalue extraction, similarly to the classical flutter prediction techniques.

Bhatia *et al* [35] determined the flutter speed of a 2D flat plate in transonic speeds, using an eigenvalue approach. The fluid was modeled by the Euler equations in conservative form followed by linearization about a steady state, where small, oscillatory unsteady perturbations of all the unknowns were assumed. A uniform beam was used to model the structure and the equilibrium equations were obtained using the principle of virtual work. The resulting system of equations related the structural and aerodynamic forces in which the latter was written in terms of a generalized force matrix. The Euler equations were also discretized according to energy methods in particular the Streamline-Upwind-Petrov-Galerkin (SUPG) technique. Since the resulting aerodynamic system of equations was related to the structural unknowns by the boundary condition, the two systems could be organized in a coupled fluid-structure system of equations. The coupled linearized system was represented in a state-space form and, through a series of simplifications, it became suitable for the application of the usual linear stability analysis. The author presents a methodology for computing all the necessary matrices, but despite that, it is only a matter of solving a nonlinear eigenvalue problem, and methods such as the k-method or p-k method can be used. The k method was chosen for solving the flutter equation for the case of a simply supported panel. Both dynamic pressure and frequency of the critical mode were plotted for Mach numbers ranging from 0.4 to 2. Since the results have shown good agreement with the available literature it became clear that high-fidelity alternatives to the expensive time domain techniques are possible at a much lower computational cost.

Finally, when addressing computational efficiency in modern flutter calculations, it is important to mention the Reduced Order Methods (ROMs). These represent a variety of existing and emerging methodologies that either simplify the governing equations or use data from expensive CAE simulations in order to construct a reduced, but compact, version of the aeroelastic system. Carlson *et al* [36] have built an aeroelastic ROM using the Proper Orthogonal Decomposition (POD) method to determine the flutter boundary of the AGARD 445.6 wing. The POD method transforms the high dimensional CAE data system into a low dimension system in modal space. The resulting reduced system reflects the important dynamical behavior of the original high-order system. In this case, the CAE data was obtained by eight high-fidelity inviscid CFD simulations, one per combination of dynamic pressure and Mach number, covering the subsonic, transonic and supersonic regions. The ROM was solved using 8 POD modes and the flutter dynamic pressure was obtained and plotted versus the Mach number. The results were validated with the same high quality CFD simulations performed at a larger set of points, and in general, the error was small. The authors conclude about the feasibility of this ROM technique for most flutter calculations but recommend more CAE data in the transonic region where the error was the highest.

Recently, Lai *et al* [37] studied the effects of a trailing edge flap on the flutter boundary using a different ROM method. The method used is a type of System Identification (SI) process that essentially builds the aeroelastic ROM equations by performing several measurements or high fidelity calculations on the wing. The many measurements, called aeroelastic states, are performed at two different flight conditions, namely at the ground and at a reference speed. These consist in time histories of diverse structural and aerodynamic variables such as displacements and fluid velocities. The aeroelastic data was obtained from coupled fluid-structure simulations where the structure was discretized by FEM and the fluid by the Euler equations using the finite volume approach. The main task was to identify separately the structural and aerodynamic systems and then to couple them to form the aeroelastic ROM. While the structural system is easily identified by performing FEM analysis for instance, the aerodynamic one is physically coupled with the structural system and therefore hard to identify. The system identification process used involves subtracting the structural sub-states from the aeroelastic states in order to obtain the pure aerodynamic states. Afterwards, the aerodynamic states are coupled with the structural states and the aeroelastic ROM is defined. The flutter boundary is calculated by determining the eigenvalues of the ROM system. The clean wing results were validated with data from the literature and in general they have shown good agreement. It was found that, in comparison with the clean configuration, the flap deflection angle has a profound impact on flutter stability, especially at transonic speeds, leading to a substantial drop in the flutter speed. The cause was attributed to the combined effects of increased effective angle of attack and flow nonlinearities.

3 MOTIVATION AND PRESENT WORK

The idea behind the present work was to develop and implement a numerical method capable of predicting the flutter speed of a 3D airplane wing. The task of choosing such method was not straight forward and essentially involved five decisions:

1. Object of study
2. Flight regime
3. Theoretical model
4. Methodology
5. Implementation

3.1 PRELIMINARY ASPECTS

Identifying the object of study is the easiest step in the decision process because it is the physical body being studied that is prescribed in the objective of the work – an airplane wing. However, the type and shape of the wing are determining factors towards the choice of the theoretical model. The interactions between fluid and body are highly dependent on the complexity of its geometry. The numerical predictions of these interactions are only as accurate as the validity of the aerodynamic theory used.

The flight regime defines the set of parameters that characterize the flight. Among these are the Mach number and the angle of attack. The flight regime also determines the theoretical model to be chosen. Depending on the Mach number and angle of attack, different aerodynamic phenomena may occur, which require adequate theories in order to be correctly predicted.

The theoretical model encompasses both structural and aerodynamic theories. They are behind every calculation and define the domain of applicability of the current method.

The methodology is the set of procedures in order to obtain the solution – the wing's flutter speed – and it is highly dependent on the theories selected. Along with the theoretical model, the methodology is a core aspect in the decision process and usually determines the numerical method used.

Finally, the implementation aspects are related to the numerical tools used for the realization of the method. Being a computer program, a programming language needs to be selected along with the planning of the internal structure of the code. These aspects are based on the adaptability of the language to the number and type of numerical tasks required by the method and on the code's overall computational efficiency.

3.2 MODEL LIMITATIONS

The wing is modeled as a 3D body, with all the characteristics of a conventional airplane wing like the sweep angle, dihedral and taper. The airfoil, however, is assumed to be very thin with low to moderate camber in order to avoid complex aerodynamic phenomena, such as flow separation, that are difficult to predict. Accordingly, the admissible angle of attack is considered small, typically within $\pm 5°$.

Compressibility effects are also included, but the flight speed is restricted to the subsonic region. The transonic and supersonic regions give rise to shockwaves in the flow field around the wing that may difficult the analysis. This is especially true for the transonic Mach numbers where the shock-body interactions are strong and complex, therefore requiring overly elaborate aerodynamic theories to model them. The theoretical model is adapted to the defined constraints. Subsonic flow over slender bodies has been extensively studied in the past, most of them relying on simplified aerodynamic theories such as the linearized potential aerodynamics. Due to time limitations, it is noted that the main purpose of this dissertation is not to develop a complex state-of-the-art method, but to develop a tool that is capable of predicting the flutter speed of a conventional 3D airplane wing. For this reason, it was decided that the linearized potential aerodynamic theory was an appropriate aerodynamic model for the development of the tool. On the other hand, the wing structure is modeled using a 1D elastic beam-rod, representing the wing's elastic axis. While this simplification greatly facilitates the program development, it narrows the validity of the aeroelastic analysis to higher aspect ratio wings. As seen in the previous section, there are some well-known methodologies for solving the pressure field using linearized potential aerodynamics. The three most recognized ones are the Strip Theory, the DLM and the Panel Methods. The Strip Theory is inherently 2D and does not account for compressibility effects. It is considered too simplistic for the present work and therefore it is discarded from the options. The DLM and Panel Methods are appropriate candidates concerning their moderate complexity and generality of application. Table 1 compares the various lifting surface methods to the conventional panel methods.

Table 1: comparison of the capabilities between lifting surface methods and conventional Panel Methods

	Lifting Surface Methods (DLM and others[1])	Conventional Panel Methods
Tridimensional	Yes	Yes
Unsteady compressible flow	Yes	No
Time-domain	No	Yes
Frequency-domain	Yes	No
Wake discretization	No	Yes
Surface type	Open	Closed
Surface discretization	Oriented	Free

In general, lifting surface methods are more suitable for the problem under consideration. Unlike the panel methods, they allow unsteady compressible calculations while being formulated in the convenient frequency domain. The DLM is well-known and has been used in linear flutter prediction since its development in the late sixties. However, lifting surface methods are more restricted concerning the arbitrariness of the geometries involved and require a particular discretization scheme. On the other hand, panel methods allow free discretization of the several surfaces that represent the true boundaries of the body. Thus, they are more useful when dealing with complex configurations. But the lack of frequency domain approaches for panel methods makes them a less efficient tool for flutter prediction, especially when better alternatives such as the DLM exist.

---

[1] Kernel Function method for instance [14]

Here, instead of choosing the DLM and implementing its methodology from known formulas, an alternative method is sought. The conventional panel methods are mostly based on the work of Hess and Smith [18] and more recently of Katz and Plotkin [19]. These are restricted to low-speed aerodynamics and compressible formulations are only available for steady flows. Within this restricted flight regime, their applicability has been proven several times for their speed and feasibility on predicting pressure fields on single or multiple wing-like components. The success of these conventional panel methods is mainly because the exact formulas for the influence coefficients are known. A prominent contribution towards generalized potential formulations is presented in a NASA report [38] by L. Morino in 1974. Starting with the full nonlinear compressible potential equation, Morino used the Green's function [39] approach to obtain a general time-domain integral solution for the potential, anywhere within the flow region. Being a general formulation, the conventional panel method integral equations can be obtained by assuming incompressible flow. A more interesting equation is obtained if one assumes small-perturbations in conjunction with harmonic oscillation potential. In this case, the integral equation becomes linear and the steady part can be completely decoupled from the unsteady part which allows both problems to be solved independently. Since the latter part is formulated in the convenient frequency-domain, it is appropriate for flutter calculations. The downside of this formulation resides mostly on the lack of exact formulas for evaluating the integrals, thus requiring numerical procedures.

The method has been successfully implemented by NASA in the eighties, being first validated in a technical report by Yates *et al.* [40]. In this report, the flutter boundaries of four cantilever rectangular wings with different thickness ratios were obtained and have shown good results with the available experimental data. In a later report by Cunningham [41], the method was re-applied to an F-5 wing model with and without a tip-mounted missile. In this case, the unsteady lift and moment coefficients were calculated for several Mach numbers and two oscillation frequencies. Despite the absence of flutter calculations, the results agreed quite well with the experiments which increased the method's credibility for more complex and realistic configurations. The advantages of this method and its apparent lack of widespread usage in the aeroelastic industry instigated the idea of implementing a similar method. In this sense, this dissertation have been mainly focused in attempting to implement Morino's frequency-domain panel method to model the flutter response of a 3D wing model. The implementation process closely follows reference [38], however, for improved clarity, additional details have been introduced in this thesis. The panel method has been fully developed and implemented in a personal computer using MATLAB® as programming language. Although alternative, faster languages such as C/C++ could have been used, MATLAB® excels in matrix operations while providing plenty of built-in functions that greatly facilitate the realization of the majority of tasks involved. The structural beam-rod was discretized using the finite element method, using the commercial software ANSYS® for generating the structural matrices. The final aeroelastic system of equations is written in terms of the structural DoFs and contains the mass, stiffness and AIC matrices. The AIC matrix expresses the generalized aerodynamic force and is obtained indirectly from the panel method.

4 THEORETICAL BACKGROUND

In this chapter, for completeness, the theoretical foundations of the developed aeroelastic flutter solver are presented and described in detail. The first part of the text (§4.1) serves as an introductory note where some alternative aerodynamic theories of relevance are briefly described. The second part (§4.2, §4.3) addresses the theoretical and implementation aspects concerning the aerodynamic and structural models incorporated in the program. Finally, in the third part (§4.4), the aeroelastic model is defined and the solution process is explained. This includes the theoretical background and computer implementation of the modified p-k method, which has been fully developed in the current work.

4.1 ALTERNATIVE THEORIES

The current section provides a brief explanation of other aerodynamic theories that have been used for aeroelastic applications, in particular for determining the flutter speed. The first part of this section outlines the classical theories based on frequency domain formulations, such as the Strip Theory and the DLM. A more detailed description is provided for the Strip Theory since it was also implemented in the main work for validation purposes. The second part of this section includes two time-domain formulations, a high-fidelity Fluid Structure Interaction (FSI) method and a conventional unsteady panel method. In addition to the aerodynamic models, compatible structural models are also mentioned in order to clarify the architecture of the resulting aeroelastic model.

4.1.1 Strip Theory

The strip theory [8] [9] is considered the classical aerodynamic theory for solving aeroelastic flutter problems. The wing is modeled by an infinite flat plate submerged in a steady, incompressible potential flow. Each airfoil section is rigid in the chordwise direction allowing only small rigid rotations (angle of attack) about the wing's elastic axis which is free to perform small translations in the vertical direction (heave), as illustrated in Figure 1. The coordinate system is centered at the elastic axis (X_{EA}) and the aerodynamic center is placed at X_{AC}:
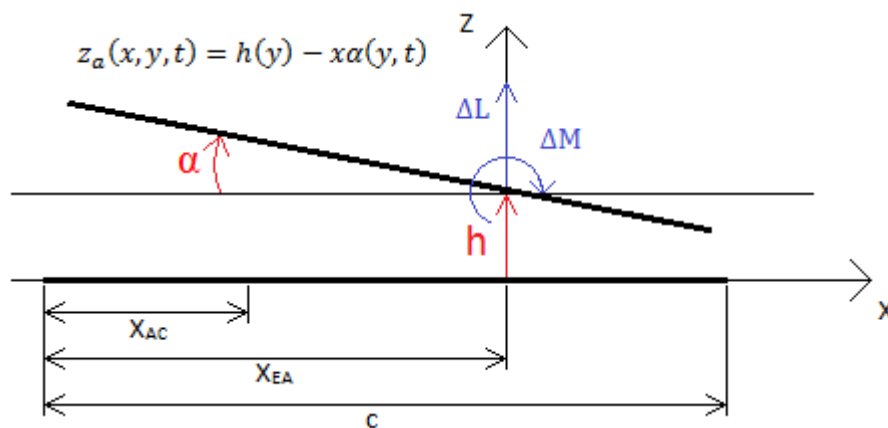
Figure 1: coordinate system for the 2D flat plate airfoil with 2 DoFs

The flow field equation is simply:

$$\nabla^2 \Phi = 0 \tag{4}$$

Where Φ is the velocity potential. With boundary conditions for a lifting airfoil:

$$\left[\frac{\partial \Phi}{\partial z}\right]_{z=\pm 0} = w_a \equiv \frac{\partial z_a}{\partial t} + U_\infty \frac{\partial z_a}{\partial x} \tag{5}$$

The subscript "a" indicates that the quantity is measured on the airfoil that is on the z=0 plane. It is assumed that the derivative is continuous across the airfoil ($z = \pm 0$). The pressure difference is given by:

$$\Delta p = -\rho_\infty \left[\frac{\partial \Delta \phi}{\partial t} + U_\infty \frac{\partial \Delta \phi}{\partial x}\right] \tag{6}$$

$$\Delta \Phi \equiv \Phi_{\text{lower}} - \Phi_{\text{upper}} \tag{7}$$

$$p, \Phi \to 0 \text{ as } z \to \infty \tag{8}$$

The airfoil is modeled by a vortex singularity line $\gamma(x, t)$ that extends to infinity defining the wake beyond the trailing edge. The induced vertical velocity (upwash) is given by the following integral:

$$w_a(x, t) = \left[\frac{\partial \Phi}{\partial z}\right]_{z=0} = \frac{1}{2\pi} \int_{-b}^{\infty} \frac{\gamma(\xi, t)}{x - \xi} d\xi \tag{9}$$

$$\gamma(x, y) \equiv \left[\frac{\partial \Phi}{\partial x}\right]_{\text{upper}} - \left[\frac{\partial \Phi}{\partial x}\right]_{\text{lower}} \tag{10}$$

Introducing the circulation integral:

$$\Gamma(x, t) \equiv \int_{-b}^{x} \gamma(\xi, t) d\xi = \int_{-b}^{x} \left[\frac{\partial \Phi_{\text{upper}}}{\partial \xi} - \frac{\partial \Phi_{\text{lower}}}{\partial \xi}\right] d\xi = -\Delta \Phi(x, t) \tag{11}$$

Thus once γ (and hence Γ) is known, $\Delta p(x, t)$ is readily computed. The full solution procedure is mathematically cumbersome and have not been reproduced here [9]. The methodology involves obtaining the vortex strength γ from equation (9) by inverting the relation between γ and w_a. In the process, a special function (solving kernel) is chosen such that the Kutta condition is satisfied, i.e., $\gamma \neq \infty$ or $\Delta p \neq \infty$ at the trailing edge. In flutter calculations, the most common approach is to convert the equations to the frequency domain by assuming simple harmonic motion. In other words, all variables oscillate in time according to:

$$w_a(x, t) = \bar{w}_a(x) e^{i\omega t}$$
$$\gamma_a(x, t) = \bar{\gamma}_a(x) e^{i\omega t} \tag{12}$$

$$\ldots$$

In the coordinate system shown in Figure 1, the airfoil unsteady lift and moment amplitudes are given by:

$$\Delta \bar{L} = \frac{1}{2} \rho_\infty U_\infty^2 c \left(i \frac{\pi}{2} k \bar{\alpha} + \frac{\pi}{2} k^2 \frac{\bar{h}}{c}\right) + \frac{1}{2} \rho_\infty U_\infty^2 c C\left(\frac{k}{2}\right) \left(2\pi \bar{\alpha} - i2\pi k \frac{\bar{h}}{c} + i2\pi k \bar{\alpha}\right) \tag{13}$$

$$\Delta\overline{M} = \frac{1}{2}\,\rho_\infty U_\infty^2 c^2 \left(-i\frac{\pi}{8}k\overline{\alpha} + \frac{\pi}{64}k^2\overline{\alpha}\right) + \frac{1}{2}\,\rho_\infty U_\infty^2 c^2 C\left(\frac{k}{2}\right)\left(\frac{\pi}{2}\overline{\alpha} - i\frac{\pi}{2}k\frac{\overline{h}}{c} + i\frac{\pi}{8}k\overline{\alpha}\right) \tag{14}$$

- The lift and moment have units of force per unit span and moment per unit span respectively
- ρ_∞, U_∞ are the far field air density and flight speed
- c is the airfoil section chord
- i represents the imaginary unit
- $\overline{h}, \overline{\alpha}$ are the heave and pitch (angle of attack) unsteady amplitudes respectively
- k is the non-dimensional vibration frequency called "reduced frequency" given by $k \equiv \frac{\omega c}{U_\infty}$
- For the moment calculation, the lift was considered at the aerodynamic center at ¼ chord

Finally, the function $C\left(\frac{k}{2}\right)$ is the complex, transcendental Theodorsen's function which is given by:

$$C\left(\frac{k}{2}\right) \equiv \left[\frac{H_1^{(2)}}{H_1^{(2)} + iH_0^{(2)}}\right]_{\frac{k}{2}} \tag{15}$$

Where $H_0^{(2)}$ and $H_1^{(2)}$ are standard Henkel functions that can be readily computed using MATLAB or other math software. In the lift and moment equations above, the terms containing $C\left(\frac{k}{2}\right)$ carry the circulatory effects and the remaining terms the inertial ones. This function models the aerodynamic lag caused by the unsteady vortex singularity distribution that constitutes the wake. Since it is a complex quantity with magnitude less than unity, the overall effect is to decrease the amplitude of the lift and moment and also change its phase with $\overline{h}$ and $\overline{\alpha}$. Setting $C\left(\frac{k}{2}\right) = 1$ and discarding the inertial terms, the lift and moment formulas become the often called "quasi-steady aerodynamics" forces. This concludes the aerodynamic modelling of the strip theory.

It is important to notice that this theory is two dimensional therefore tridimensional effects such as wing tip vortices are not taken into account. Although it can be applied to full 3D wings, in the Strip Theory, each "wing strip" generates its own pressure field as if the wing itself is infinite in the spanwise direction.

Structural Model

A simple and compatible structural model is to treat the elastic axis as a one dimensional beam-rod, a structural element that supports bending and torsion. The equilibrium equations can be obtained applying Lagrange's equation to the aeroelastic system:

$$\frac{d}{dt}\left(\frac{\partial(T-V)}{\partial\dot{q}_i}\right) - \frac{\partial(T-V)}{\partial q_i} = Q_i \tag{16}$$

Where

$$T = \frac{1}{2}\int_0^L m\dot{z}_a^2\,dy = \frac{1}{2}\int_0^L \lambda\dot{h}^2\,dy - \int_0^L S_\alpha\,\dot{h}\dot{\alpha}\,dy + \int_0^L I_\alpha\dot{\alpha}^2\,dy \tag{17}$$

$$V = \frac{1}{2}\int_0^L EI_{xx}\left(\frac{\partial^2 h}{\partial y^2}\right)^2 dy + \frac{1}{2}\int_0^L GJ\left(\frac{\partial\alpha}{\partial y}\right)^2 dy \tag{18}$$

$$Q_h \equiv \frac{\delta W_{NC}}{\delta q^h} = L \quad Q_\alpha \equiv \frac{\delta W_{NC}}{\delta q^\alpha} = M \tag{19}$$

- q_i are the generalized coordinates, either h or α
- m is the wing mass per unit area
- λ is the wing mass per unit span
- S_α is the inertial coupling given by $\int_0^c mx\,dx$
- I_α is the cross section moment of inertia given by $\int_0^c mx^2\,dx$
- EI_{xx} is the spanwise bending rigidity
- GJ is the torsional rigidity
- L is the wing semi-span
- Q_h and Q_α are the generalized forces corresponding to the total lift and pitching moment respectively. Their explicit formula can be obtained from the non-conservative work formula W_{NC} (31) and depends on the actual method of solution

The elastic energies (18) refer to the classical Euler-Bernoulli beam theory for bending and St. Venant uniform torsion theory for torsion. Equation (16) can be solved by several methods, depending on the complexity of the structure and the theories used to write the energies and generalized forces. Such methodologies include the Galerkin method, the Rayleigh-Ritz method and the FEM. For instance, in the Rayleigh-Ritz method, the solution is approximated by a linear combination of shape functions and the generalized coordinates. For the current problem, the solution h and α would take the form:

$$h(y,t) = \sum_{r=1}^{N_h} \varphi_r^h(y) q_r^h(t) \tag{20}$$

$$\alpha(y,t) = \sum_{m=1}^{N_\alpha} \varphi_m^\alpha(y) q_m^\alpha(t) \tag{21}$$

φ_r^h and φ_m^α are the shape functions for h and α respectively, and should satisfy the geometrical boundary conditions. Generally they are dimensionless polynomials or trigonometric functions in which some geometrical parameter is involved in the expression. The quantities $q_r^h(t)$ and $q_m^\alpha(t)$ are the dimensional $N_h + N_\alpha$ new generalized coordinates of the problem. Introducing these expressions in the energy formulas (17) and (18) one obtains:

$$T = \frac{1}{2}\sum_r^{N_h}\sum_s^{N_h} M_{rs}^{hh}\dot{q}_r^h\dot{q}_s^h + \sum_r^{N_h}\sum_m^{N_\alpha} M_{rm}^{h\alpha}\dot{q}_r^h\dot{q}_m^\alpha + \frac{1}{2}\sum_m^{N_\alpha}\sum_n^{N_\alpha} M_{mn}^{\alpha\alpha}\dot{q}_m^\alpha\dot{q}_n^\alpha \tag{22}$$

$$V = \frac{1}{2}\sum_r^{N_h}\sum_s^{N_h} K_{rs}^{hh}q_r^hq_s^h + \frac{1}{2}\sum_m^{N_\alpha}\sum_n^{N_\alpha} K_{mn}^{\alpha\alpha}q_m^\alpha q_n^\alpha \tag{23}$$

Definitions:

$$M_{rs}^{hh} \equiv \int_0^L \lambda \, \varphi_r^h(y) \varphi_s^h(y) dy \quad M_{rm}^{h\alpha} \equiv - \int_0^L S_\alpha \, \varphi_r^h(y) \varphi_m^\alpha(y) dy \tag{24}$$

$$M_{mn}^{\alpha\alpha} \equiv \int_0^L I_\alpha \, \varphi_m^\alpha(y) \varphi_n^\alpha(y) dy \tag{25}$$

$$K_{rs}^{hh} \equiv \int_0^L EI_{xx} \, \varphi_r^h(y) \varphi_s^h(y) dy \quad K_{mn}^{\alpha\alpha} \equiv \int_0^L GJ \, \varphi_m^\alpha(y) \varphi_n^\alpha(y) dy \tag{26}$$

M and K are the mass and stiffness matrices of the wing, respectively. The Lagrange equation can now be re-written $N_h + N_\alpha$ times, in terms of the $N_h + N_\alpha$ generalized coordinates q_i defining a closed system of equations:

$$\sum_{j=1}^{N_h+N_\alpha} M_{ij} \ddot{q}_j + K_{ij} q_j = Q_i(q_j) \quad i = 1, \dots N_h + N_\alpha \tag{27}$$

Defining the complex frequency s and its dimensionless form p:

$$s \equiv \delta + i\omega, \qquad p \equiv k(\gamma + i) \equiv \left(\frac{c}{U_\infty}\right) s \tag{28}$$

And allowing damped oscillations in time:

$$q_j(t) = \bar{q}_j e^{st} \tag{29}$$

The Lagrange equations can now be written in the convenient frequency domain:

$$\left(\frac{U_\infty}{c}\right)^2 \sum_{j=1}^{N_h+N_\alpha} p^2 \bar{M}_{ij} \, \bar{q}_j + \bar{K}_{ij} \bar{q}_j = \bar{Q}_i(\bar{q}_j) \tag{30}$$

The explicit formula for the generalized force $\bar{Q}_i(\bar{q}_j)$ can be obtained by first calculating the non-conservative work performed by the pressure forces on the wing:

$$\delta W_{NC} = \int_0^L \int \Delta p \delta z_a dx dy = \int_0^L \int p dx \delta h dy - \int_0^L \int p x dx \delta \alpha dy =$$
$$= \int_0^L \overline{\Delta L}(\bar{h}, \bar{\alpha}) \sum_r^{N_h} \varphi_r^h(y) dy \delta q_r^h e^{i\omega t} + \int_0^L \overline{\Delta M}(\bar{h}, \bar{\alpha}) \sum_m^{N_\alpha} \varphi_m^\alpha(y) dy \delta q_m^\alpha e^{i\omega t} \tag{31}$$

And then using the definitions in (19):

$$Q_h = \bar{Q}_h e^{st} = \frac{\delta W_{NC}}{\delta q^h} = \left[\int_0^L \overline{\Delta L}(\bar{h}, \bar{\alpha}) \varphi_r^h(y) dy \right] e^{st} \tag{32}$$

$$Q_\alpha = \bar{Q}_\alpha e^{st} = \frac{\delta W_{NC}}{\delta q^\alpha} = \left[\int_0^L \overline{\Delta M}(\bar{h}, \bar{\alpha}) \varphi_m^\alpha(y) dy \right] e^{st} \tag{33}$$

The last step is to expand $\bar{h}$ and $\bar{\alpha}$ in the sectional lift and moment formulas defined in equations (13) and (14) using the shape functions (20) and (21). In order to avoid complex quantities in the final system

of equations, the complex unit is absorbed into the complex frequency "s" and then converted to its dimensionless form "p":

$$i\omega \underset{\gamma \cong 0}{=} s = \left(\frac{U_\infty}{c}\right)p \tag{34}$$

This is only exact for $\gamma = 0$ (flutter boundary) being an approximation elsewhere. In general, for linear flutter problems, the modes are lightly damped therefore such inconsistence should be of minor concern. The resulting generalized forces are the following:

$$\bar{Q}_{ij} = \begin{bmatrix} \bar{Q}_{hh} & \bar{Q}_{h\alpha} \\ \bar{Q}_{\alpha h} & \bar{Q}_{\alpha\alpha} \end{bmatrix} \tag{35}$$

$$\bar{Q}_{hh} = \frac{1}{2}\,\rho_\infty U_\infty^2 c * \frac{2\pi}{c}\left[\left(G\left(\frac{k}{2}\right) + \frac{k^2}{4}\right) - F\left(\frac{k}{2}\right)p\right]\sum_{s=1}^{N_h}\int_0^L \varphi_r^h(y)\varphi_s^h(y)dy\bar{q}_s^h \tag{36}$$

$$\bar{Q}_{h\alpha} = \frac{1}{2}\,\rho_\infty U_\infty^2 c * 2\pi\left[F\left(\frac{k}{2}\right) - \frac{k}{4}G\left(\frac{k}{2}\right) - \left(\frac{1}{k}G\left(\frac{k}{2}\right) - \frac{1}{4} + \frac{1}{4}F\left(\frac{k}{2}\right)\right)p\right]\sum_{n=1}^{N_\alpha}\int_0^L \varphi_m^h(y)\varphi_n^h(y)dy\bar{q}_n^\alpha \tag{37}$$

$$\bar{Q}_{\alpha h} = \frac{1}{2}\,\rho_\infty U_\infty^2 c^2 * \frac{\pi}{2c}\left[kG\left(\frac{k}{2}\right) - F\left(\frac{k}{2}\right)p\right]\sum_{s=1}^{N_h}\int_0^L \varphi_m^\alpha(y)\varphi_s^h(y)dy\bar{q}_s^h \tag{38}$$

$$\bar{Q}_{\alpha\alpha} = \frac{1}{2}\,\rho_\infty U_\infty^2 c^2 * \frac{\pi}{2}\left[F\left(\frac{k}{2}\right) - \frac{k}{4}G\left(\frac{k}{2}\right) + \frac{k^2}{32} + \left(\frac{1}{k}G\left(\frac{k}{2}\right) - \frac{1}{4} + \frac{1}{4}F\left(\frac{k}{2}\right)\right)p\right]\sum_{n=1}^{N_\alpha}\int_0^L \varphi_m^\alpha(y)\varphi_n^\alpha(y)dy\bar{q}_n^\alpha \tag{39}$$

$$C\left(\frac{k}{2}\right) \equiv F\left(\frac{k}{2}\right) + iG\left(\frac{k}{2}\right) \tag{40}$$

Finally, expanding $\bar{Q}_{ij}$ in the equilibrium equations (30) and rearranging the terms, the aeroelastic system equations in the frequency domain is fully defined:

$$\left[\sum_{j=1}^{N_h+N_\alpha}\left(\frac{U_\infty}{c}\right)^2\bar{M}_{ij}\,p^2 + \bar{C}_{ij}^A(k)p + [\bar{K}_{ij}^S - \bar{K}_{ij}^A(k)]\right]\bar{q}_j = 0 \tag{41}$$

The matrix $\bar{C}_{ij}^A$ is equivalent to an aerodynamic damping and can be obtained by grouping all terms proportional to "p" in the generalized force expressions. The remaining zero order terms can be interpreted as an aerodynamic stiffness and are grouped in matrix $\bar{K}_{ij}^A$. This equation defines a generalized nonlinear eigenvalue problem in "k" and must be solved iteratively. In order to extract the eigenvalues (and eigenvectors), several methods can be used. Amongst the most popular are the k method [27] and the p-k method [29], the latter to be presented in detail in the final section of this chapter. Flutter occurs if the solution $q_j(t) = \bar{q}_j e^{st}$ becomes unstable, i.e., if $|q_j(t)|$ grows indefinitely with time. Since $s = \omega(\gamma + i)$, the sign of real part of each eigenvalue determines such behavior:

- $\gamma < 0$: a particular mode is stable, and a perturbation in the system will be attenuated after a while

- $\gamma \geq 0$: a particular mode is unstable or on the onset of instability (flutter boundary). Any perturbation in the system can be amplified with time, potentially leading to the failure of structural components or aircraft stall

Even though there are at least as many eigenvalues as generalized coordinates, usually only the lowest magnitude eigenvalues are of interest. The remainder high frequency modes are less likely to occur in practice and may be often ignored. The flutter speed is defined as the lowest flight speed at which appears an instable eigenvalue $\mathrm{Re}(p) > 0$.

4.1.2 The Doublet Lattice Method

The DLM is an unsteady tridimensional lifting surface theory, initially presented by Albano and Rodden [15] and further developed by several authors in the following years. The theoretical basis of the DLM is the linearized compressible aerodynamic potential theory for subsonic flow. The undisturbed flow is uniform and is either steady or varying (gusting) harmonically. All lifting surfaces are assumed flat and lie parallel to the incoming flow. Each surface is divided into small trapezoidal lifting elements (called boxes) such that the boxes are arranged in strips whose sides are aligned with the undisturbed flow:
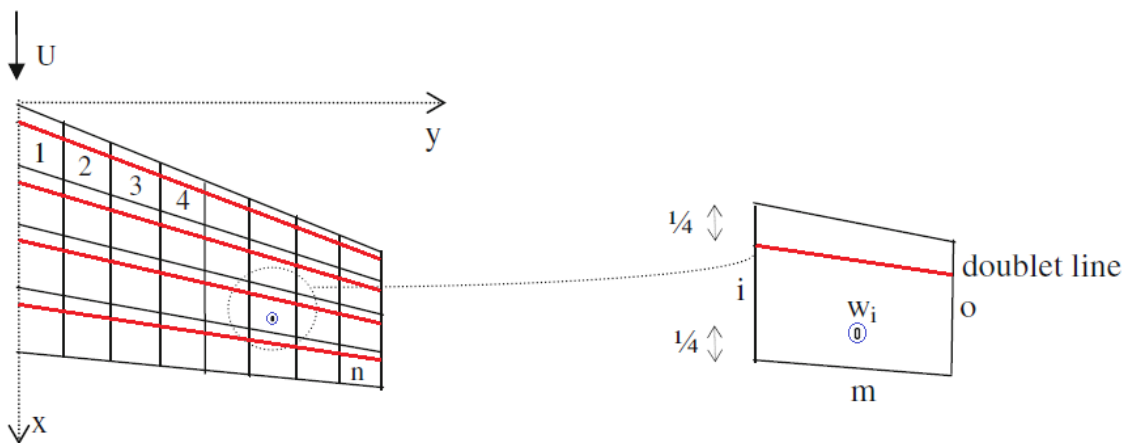
Figure 2: doublet lattice grid example (adapted from [42], page 142)

The aerodynamics is solved by collocation, in which an unknown constant strength doublet singularity line (red line) is placed at ¼ chord of each box and a control point, where the pressure and boundary condition are evaluated, is placed at the ¾ chord (blue dot). Although there is no mathematical proof, from numerical experimentation with this collocation scheme, it has become apparent that the Kutta condition at the wing's trailing edge will be satisfied approximately [15]. The downwash w_i induced on the control point of the ith box by the doublet lines of the boxes j = 1,2,…,n shown in Figure 2, can be expressed as follows:

$$\overline{w}_i = \sum_{j=1}^{n} D_{ij} \overline{\Delta p_j} \tag{42}$$

The matrix D_{ij} contains the pressure influence coefficients of each box j on the downwash at the control point i. This matrix condenses the aerodynamics and is generally written as the following integral:

$$D_{ij} = \frac{1}{4\pi\rho_\infty U_\infty} \, x_j \cos\lambda_j \int K\big(x_i, s_i, x_j(\mu), s_j(\mu), k\big) d\mu_j \tag{43}$$

Here, (x_i, s_i) refer to the orthogonal surface coordinates of the influenced point (receiver) such that the undisturbed stream is directed parallel to the x axis and $\big((x_j(\mu), s_j(\mu)\big)$ to the surface coordinates of the influencing doublet line parameterized by μ. The parameter λ_j stands for the doublet line sweep angle. The function K is the "Kernel function" whose complicated analytical expression will not be reproduced here. Once the matrix D_{ij} is calculated (equation (42)), it can be inverted in order to obtain the pressure in terms of the downwash:

$$\overline{\Delta p}_i = \sum_{j=1}^{n} A_{ij}\overline{w}_j, \qquad A_{ij} \equiv D_{ij}^{-1} \tag{44}$$

The last step in the DLM is to impose the boundary condition at the surface of the wing:

$$\overline{w}(x,y) = \left(i\omega + U_\infty \frac{\partial}{\partial x}\right) \overline{z}_a(x,y) \tag{45}$$

Here, $\overline{z}_a$ is the function defining the surface of the wing. In accordance with the DLM, this surface should be a single, zero thickness surface with some curvature allowed. However, for flutter calculations, this surface should be written in terms of generalized coordinates in order to proceed to the stability analysis. Such procedure depends on the structural theory chosen to model the wing. As in the strip theory, a common model is the one dimensional beam-rod. For instance, consider a flat, swept wing and the coordinate system shown in Figure 3:
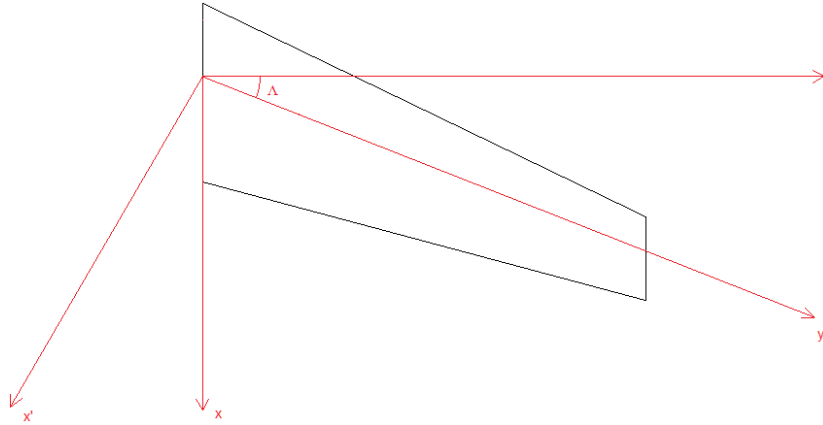
Figure 3: aerodynamic and structural coordinate systems for flat wing with sweep angle Λ

The elastic axis defines the beam-rod and is allowed to bend in the Z direction and rotate about the y' axis. In the elastic coordinate system, the deflection at any point on the wing is given by:

$$\overline{z}_a(x', y') = \overline{h}(y') - x'\overline{\alpha}(y') \tag{46}$$

Using the coordinate system depicted in Figure 3, the elastic coordinates are related to the aerodynamic ones by the following formulas:

$$x' = x \cos \Lambda - y \sin \Lambda \tag{47}$$

$$y' = x \sin \Lambda + y \cos \Lambda \tag{48}$$

Rewriting z_a:

$$\bar{z}_a(x, y) = \bar{h}(y'(x, y)) - (x \cos \Lambda - y \sin \Lambda)\bar{\alpha}(y'(x, y)) \tag{49}$$

Now it is possible to relate the downwash $\bar{w}$ with the beam's deflection $\bar{h}$ and rotation angle $\bar{\alpha}$ by applying the boundary condition:

$$\bar{w}(x, y) = \left(i\omega + U_\infty (\sin \Lambda + \cos \Lambda) \frac{\partial}{\partial y'} \right) \bar{h}$$
$$+ \left(i\omega \left[y \sin \Lambda - \cos \Lambda \left(x + \frac{U_\infty}{i\omega} \right) \right] + U_\infty [(x + y) \sin^2 \Lambda + (y - x) \sin \Lambda \cos \Lambda - x] \frac{\partial}{\partial y'} \right) \bar{\alpha} \tag{50}$$

In order to transform equation (50) to its vector form, it is necessary to transfer the aerodynamic nodes and forces into the structural ones. The most simple way is to assume that each box strip (along X direction) is uniquely connected to a single structural node located at the elastic axis on the same wing strip. Thus, the downwashes $\bar{w}_j$ from equation (44) are obtained by applying equation (50) for each aerodynamic node located in (x,y) with the unknowns $\bar{h}$ and $\bar{\alpha}$ constant for each wing strip. Consider the wing strip depicted in Figure 4 for instance. If the wing strip contains boxes j, j+1 and j+2 and the respective structural node is "m", then the downwashes $\bar{w}_j$, $\bar{w}_{j+1}$ and $\bar{w}_{j+2}$ are written in terms of the same structural DoFs $\bar{h}_m$ and $\bar{\alpha}_m$ using equation (50). Numerically, since $\bar{h}_m$ and $\bar{\alpha}_m$ are constant for all the boxes in a strip, this is equivalent to summing up the downwashes along the same strip.
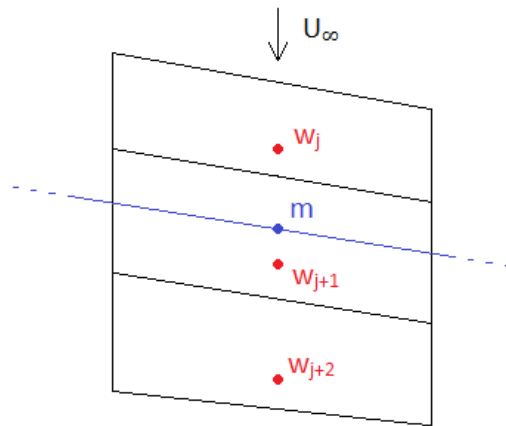
Figure 4: wing strip containing 3 DLM boxes with control points j, j+1 and j+2

The aerodynamic forces and torsional moments can be calculated at "m" by integrating the pressure Δp_j along the strip:

$$\bar{L}_m = \sum_{j \in Strip}^{N_j} \Delta \bar{p}_j \Delta S_j \tag{51}$$

23

$$\bar{M}_m = \sum_{j \,\in\, Strip}^{N_j} \Delta\bar{p}_j \Delta S_j \left(x_j - x_j^m\right) \cos\Lambda \tag{52}$$

- ΔS_j is the area of each aerodynamic box
- x_j^m is the position of the elastic axis (structural node "m") on each strip

Upon performing these two steps, the lift and torsional moment are written in terms of the heave $\bar{h}$ and pitch angle $\bar{\alpha}$ at each structural node. Finally, these quantities can be conveniently organized into a matrix and, in conjunction with the structure's stiffness and mass matrices, the aeroelastic problem can be solved. This procedure is essentially the planar version of the Rigid Body Attachment method described in chapter 6.4 of reference [25].

It is important to notice that in order to use this method, the derivatives $\frac{\partial h}{\partial y'}$ and $\frac{\partial \alpha}{\partial y'}$ must be evaluated numerically using for instance finite difference schemes, which constitute a source of error in the solution. Another way of solving the problem is to resort to the Rayleigh-Ritz method, introduced in the previous section (4.1.1). In the Rayleigh-Ritz method, instead of summing the downwashes of each strip, all the downwashes of all aerodynamic control points are summed and the result is a function of $h(y'), \alpha(y'), \frac{\partial h(y')}{\partial y'}$ and $\frac{\partial \alpha(y')}{\partial y'}$. The lift and pitching moment are calculated in the same way, except that the chordwise length of each box Δx_j is used instead of its area ΔS_j. Finally, the deflection and pitch angle are approximated by shape functions using equations (20) and (21), and the lift and moment generalized forces are obtained by integrating $\bar{L}$ and $\bar{M}$ over the length of the span. Since the sectional lift and moment are now continuous functions of the elastic axis coordinate y', $\frac{\partial h}{\partial y'}$ and $\frac{\partial \alpha}{\partial y'}$ can be evaluated exactly. The process of determining the mass and stiffness matrices and the methodology of obtaining the final solution from the resulting stability equation is described in section 4.1.1.

The DLM is still widely used today by the CFD/CSD industry, such as MSC.NASTRAN® and ZAERO® for its low computational cost and relatively high accuracy on wing-like components. The coupling between the aerodynamic boxes and structural nodes described above are rather simplistic and reflect the academic purpose of this thesis. More sophisticated methods used in industry include the so-called spline methods, which resort to the general analytical solutions of uniform plates and beams. Detailed information about these methods can be found in [26] and chapter 6 of [25].

4.1.3   Time-Domain Formulations

All the methods presented so far for wing flutter prediction were formulated in the frequency domain. These methods were based on the assumption of small amplitude, unsteady oscillatory behavior, about a static, equilibrium configuration. In addition, both structural and aerodynamic theories were linear, in conformity with the hypothesis of small structural displacements and small aerodynamic perturbations. Mathematically, this leads to a decoupling between the steady and unsteady terms in the final aeroelastic equation which allows the unsteady problem to be solved independently from the steady one. The flutter boundary was estimated by solving the unsteady part of the system of equations that

was essentially an eigenvalue problem (equation (3)). If any kind of non-linearity is to be included in the model, the aeroelastic problem becomes fully coupled, and the usual frequency domain approach cannot be implemented. In such cases, the flutter boundary can only theoretically be obtained via the more general time domain formulation:

$$[M]\{\ddot{w}\} + [C]\{\dot{w}\} + [K]\{w\} = \{F(t)\} \tag{53}$$

Until the development of modern computers, time formulations for aeroelastic applications were avoided because of its unconditional high CPU cost and its cheap and sufficiently accurate frequency domain alternatives. The main reasons for this high computational cost resides in the definition of proper initial conditions and the unknown duration and number of time steps required. Also, since time formulations are mostly used on non-linear problems, the several iterative procedures involved at each time step make this this approach very expensive, even in today's standards of available computational resources.

4.1.3.1 FSI Methodologies

One example of a non-linear aerodynamic problem is attempting to solve the pressure field resorting to the full Navier-Stokes equations or even the inviscid Euler equations. When such non-linear models are applied to aeroelastic problems, the respective aeroelastic analysis is commonly addressed in the scientific community as an FSI problem. A typical FSI analysis usually involves the following steps:

1. **Set the initial conditions**: wing orientation, speed, acceleration, free-stream flow speed and direction, structural and aerodynamic mesh, etc.;
2. **Determine aerodynamic forces**: according to the specified initial conditions, the non-linear aerodynamic equations are solved iteratively and the aerodynamic force at each aerodynamic node is obtained. Several methods can be used in solving the aerodynamics. For instance, the Navier-Stokes equations are often solved using the RANS approach along with turbulence models;
3. **Grid transfer**: in general, the aerodynamic grid nodes position differs from the structural ones. The forces and grid displacements can be transferred between grids via transformation matrices. Such matrices can be derived from grid coupling theories such as the 3D Infinite Plate Spline [25]
4. **Determine structural displacements**: once the aerodynamic force at each structural node is known, the displacements at the new time step can be obtained by solving equation (53). Generally, this step includes normalizing the stiffness and mass matrices with the modal matrix (equations (54) and (55)) and then using a time-marching scheme such as the Newmark algorithm [23]
5. **Track results**: the continuous generation of a plot describing the displacement or other relevant quantity over time is essential for it can provide immediate information about convergence and the overall behavior of the solution
6. **Deform mesh**: both aerodynamic and structural grids are deformed according to the calculated structural displacements. The aerodynamic grid is generated from the new structural mesh using similar spline matrices mentioned in step 3

7. **Repeat steps 2-6**: the process of constantly changing the mesh and calculating the aerodynamic forces and structural displacements is repeated for several time steps until the desired aeroelastic phenomena (flutter for instance) is observed

The following diagram depicts the several steps taken in a typical FSI problem:
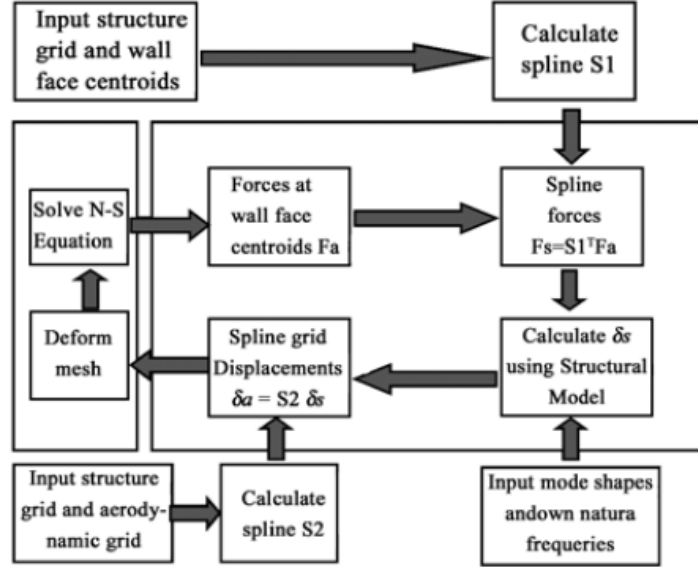
Figure 5: FSI diagram with usual computational steps taken [34]

Modal normalization (step 4 above):

$$\{q\} = [\Phi]\{w\} \tag{54}$$

$$[I] = [\Phi]^T[M][\Phi], \quad [\omega^2] = [\Phi]^T[K][\Phi], \quad [\bar{C}] \equiv [\Phi]\{w\}, \quad \{Q\} \equiv [\Phi]\{F\} \tag{55}$$

$$\{\ddot{q}\} + [\omega^2]\{q\} = \{Q\} \tag{56}$$

Time-marching scheme (Newmark algorithm):

$$\dot{q}_{n+1} = \dot{q}_n + (1-\gamma)\Delta t\ddot{q}_n + \gamma\Delta t\ddot{q}_{n+1} \tag{57}$$

$$q_{n+1} = q_n + \Delta t\dot{q}_n + \Delta t^2\left(\frac{1}{2}-\beta\right)\ddot{q}_n + \Delta t^2\beta\ddot{q}_{n+1} \tag{58}$$

$$\gamma \geq \frac{1}{2} \wedge \beta \geq \frac{1}{4}\left(\gamma+\frac{1}{2}\right)^2 \tag{59}$$

The solution is obtained in three steps:

1. Using equations (57) and (58), the aeroelastic equations are written at time step (n+1)

$$[[I] + \Delta t \gamma [\overline{C}]]\{\ddot{q}_{n+1}\} =$$

$$= \{Q_{n+1}\} - [\omega^2]\{q_n\} - [\Delta t \omega^2 + [\overline{C}]]\{\dot{q}_n\} - \left[\Delta t^2 \left(\frac{1}{2} - \beta\right)[\omega^2] + \Delta t(1 - \gamma)[\overline{C}]\right]\{\ddot{q}_n\}$$

(60)

2. Equations (60) are solved for the acceleration $\ddot{q}_{n+1}$
3. Using equations (57) and (58), the velocities $\dot{q}_{n+1}$ and displacements q_{n+1} can be obtained for the time step (n+1)

4.1.3.2 Unsteady Panel Methods

For low subsonic speeds, accurate and relatively fast time-domain aeroelastic solutions can be obtained using incompressible, unsteady panel methods. Similarly to the DLM, panel methods are collocation methods based on linearized potential theory but, unlike the DLM, they are not restricted to a single lifting surface. These methods allow the free discretization (paneling) of tridimensional geometries which makes them more versatile when comparing to lifting surface methods. However, the wake modeling is mandatory in order to satisfy the Kutta condition and to preserve the total circulation at each time step (Helmholtz theorem). The unsteady panel method given by Katz & Plotkin [19] has been used extensively in the literature for its fast, accurate and general applicability within the domain of flow around slender bodies. The pressure field at each time step is computed by introducing constant source σ_j and doublet μ_j singularities distributions at each panel and then satisfying the boundary condition of zero normal fluid flux at every control point of the body:

$$\frac{\partial \Phi}{\partial n} - (\mathbf{V_0} + \mathbf{v_{rel}} + \boldsymbol{\Omega} \times \mathbf{r}) \cdot \mathbf{n} = 0$$

$$\Leftrightarrow \sigma = -\mathbf{n} \cdot (\mathbf{V_0} + \mathbf{v_{rel}} + \boldsymbol{\Omega} \times \mathbf{r})$$

(61)

- All quantities (velocities) are measured in the body frame of reference
- Φ is the velocity potential and $\frac{\partial \Phi}{\partial n}$ is the fluid normal velocity
- $\mathbf{V_0}$ is the translational kinetic body velocity
- $\boldsymbol{\Omega} \times \mathbf{r}$ is the rotational kinetic body velocity
- $\mathbf{v_{rel}}$ is the relative body velocity (deformation rate)
- $\mathbf{n}$ is the normal surface unit vector

Additionally, the Kutta condition is a physical condition that must be numerically imposed at the trailing edge panels:

$$\gamma_{TE} \equiv -\frac{\partial \mu_{TE}}{\partial x} = 0 \Leftrightarrow (\mu_u - \mu_l)_{TE} = \mu_{W_{TE}}$$

$$u_x \equiv \frac{\partial \mu}{\partial x}$$

(62)

- γ_{TE} is the trailing edge vorticity
- μ_u and μ_l are the doublet strengths of the upper and lower trailing edge panels respectively
- $\mu_{W_{TE}}$ is the doublet strength of the 1st wake panel

- u_x is the X component of the induced perturbation flow velocity

The Kutta condition expressed above basically forces the trailing edge to be a flow stagnation point and is valid for 2D flows. In 3D unsteady flows, the validity of this assumption depends on the component of the kinematic velocity, normal to the trailing edge $U_{TE}^n(t)$, which must be much smaller than the characteristic velocity U_∞.

The wake is divided in several panels with different orientations and lengths that are determined during the time dependent wake roll-up process. The procedure for modelling the unsteady wake can be described according to the following generic steps:

1. At the first time step $t = \Delta t$, the first row of wake panels are added to the panels of the trailing edge. These panels are usually aligned with the bisector trailing edge plane and their lengths is given by $\Delta l_{wake} = U_{TE}(t)\Delta t$. They carry a doublet singularity whose strength is related to the trailing edge panels through the Kutta condition (equation (62))

2. Once all the singularities strengths are calculated, the velocity field can be obtained everywhere in the field, including in the wake region. Since the wake cannot sustain pressure forces, it is assumed that the wake panels are convected with the downstream flow. To achieve the wake rollup, the induced velocity $(u, v, w)_l$ at each wake panel corner point l is calculated and then the wake panels are moved by (see Figure 6):

$$(\Delta x, \Delta y, \Delta z)_l = (u, v, w)_l \Delta t \tag{63}$$

3. At the next time step, a new row of wake panels are inserted behind the trailing edge and step 2 is repeated for the two rows of wake panels. The doublet strength of the "old" row of wake panels is the same, in accordance with Helmholtz' theorem [19] §2.9
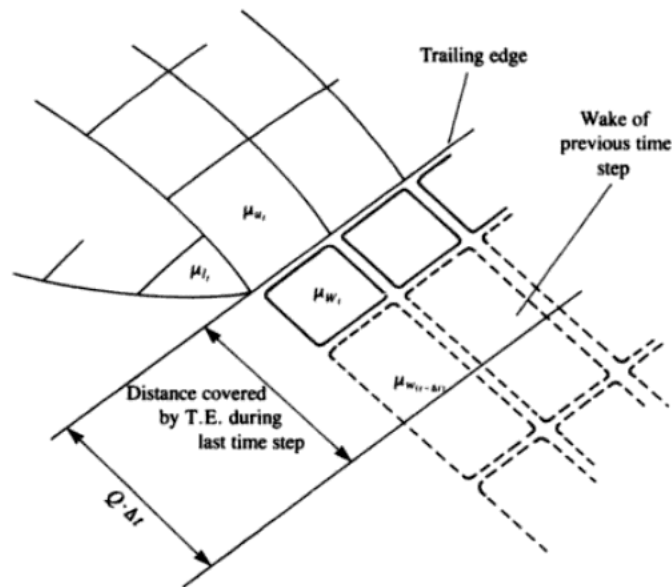
Figure 6: schematic description of a wing's trailing edge and the latest wake row of the unsteady wake (Katz & Plotkin §13.13 page 435 [19])

This aerodynamic model can be incorporated with any of the structural models described so far. In comparison with the DLM, this formulation benefits from the more elaborate wake modelling and the capability of including thickness effects. However, there is an increased computational cost, the additional requirement of proper initial conditions and it is restricted to low subsonic speed.

4.2 Aerodynamic Model (Panel Method)

The objective of this section is to present the theoretical foundations that support the aerodynamic model of the final wing flutter program, which is fundamentally an unsteady panel method in the frequency-domain. In addition, all the necessary technical details for the computer implementation of the panel method are carefully exposed. The theoretical aspects reproduced here follow the work by L. Morino [38] introduced in section 3.2.

4.2.1 Theoretical Aspects

In this sub-section, a theoretical overview of the potential flow case is presented, starting with the general potential flow field equation. Next, the panel method integral equation is formulated.

Physical preliminaries of a potential flow

- Inviscid fluid (zero viscosity)
- Curl-free velocity field (fluid particles cannot rotate $\nabla \times \mathbf{V} = 0$)

Field equation

$$a^2 \nabla^2 \Phi = \frac{D_c^2 \Phi}{Dt^2} \tag{64}$$

With

$$\frac{D_c}{Dt} \equiv \frac{\partial}{\partial t} + \nabla \Phi \cdot \nabla \tag{65}$$

Equation (64) models a compressible tridimensional unsteady potential flow field in terms of the local sound speed "a" and the total velocity potential Φ defined by:

$$\mathbf{V} = \nabla \Phi \tag{66}$$

The non-linear nature of the field equation (64), also called the full compressible potential flow equation, makes it very difficult to solve directly. A common simplification used extensively in potential aerodynamics is to write the total potential as the sum of the far-field constant potential and a small deviation (perturbation potential φ), then neglecting all the non-linear terms:

$$\Phi = U_\infty(x + \varphi) \tag{67}$$

$$\nabla^2 \varphi - \frac{1}{a_\infty^2} \frac{d^2 \varphi}{dt^2} = F(\varphi_x, \varphi_y, \varphi_z, \varphi_{xx}, \varphi_{yy}, \varphi_{zz}, \varphi_{tt}, \varphi_{xy}, \varphi_{yz}, \varphi_{xz}, \varphi_{xt}, \varphi_{yt}, \varphi_{zt}) \tag{68}$$

$$\frac{d}{dt} \equiv \frac{\partial}{\partial t} + U_\infty \frac{\partial}{\partial x} \tag{69}$$

- U_∞ represents the far-field constant velocity field which is assumed in the Ox direction
- a_∞ represents the far-field speed of sound and it is assumed constant everywhere
- F is a functional containing all the non-linear terms in φ

Considering small perturbations, $\varphi \ll \Phi$, all the non-linear terms are of second order or higher and therefore will be neglected. Setting $F = 0$ in equation (68) and expanding all the terms, the final linear equation for the compressible unsteady 3-D potential aerodynamics is the following:

$$(1 - M_\infty^2)\frac{\partial^2 \varphi}{\partial x^2} + \frac{\partial^2 \varphi}{\partial y^2} + \frac{\partial^2 \varphi}{\partial z^2} - \frac{1}{a_\infty^2}\left(\frac{\partial^2 \varphi}{\partial x^2} + 2U_\infty^2 \frac{\partial^2 \varphi}{\partial x\, \partial t}\right) = 0 \tag{70}$$

Pressure field formula

The pressure at each point can be obtained from the potential field according to Bernoulli's theorem [38] [42]:

$$p = p_\infty\left[1 - \frac{\gamma - 1}{a_\infty^2}\left(\frac{\partial \Phi}{\partial t} + \frac{1}{2}\nabla\Phi \cdot \nabla\Phi - \frac{1}{2}U_\infty^2\right)\right]^{\frac{\gamma}{\gamma - 1}} \tag{71}$$

Here, γ is the ratio of specific heats and p_∞ is the pressure of the far-field. For practical reasons and for consistency with the previous simplifications, this formula can be linearized to the following useful expression:

$$p - p_\infty = -\rho_\infty U_\infty\left(\frac{\partial \varphi}{\partial t} + U_\infty \frac{\partial \varphi}{\partial x}\right) \tag{72}$$

The symbol ρ_∞ represents the density of any point in the far-field.

Method of solution

The solution of equation (70) can be obtained by using appropriate finite difference schemes and the usual boundary and initial conditions for inviscid fluids. However, this would require the discretization of the entire flow field and therefore it is not feasible computationally. The panel method is a Boundary Element Method (BEM) that is suitable for linear equations and requires only the discretization of the boundaries (surfaces). The solution procedure is based on the Green's function, which in this case, is the solution of the following equation:

$$\nabla^2 G - \frac{1}{a_\infty^2}\frac{d^2 G}{dt^2} = \delta(x - x_1, y - y_1, z - z_1, t - t_1) \tag{73}$$

$$G = 0, (x, y, z, t) \to \infty \tag{74}$$

The delta function δ is 4-dimensional Dirac function. For the subsonic case (M<1), the Green's function is given by [42]:

$$G(x, y, z, t) = -\frac{1}{4\pi r_\beta} \delta(t_1 - t + T) \tag{75}$$

$$r_\beta \equiv \sqrt{(x - x_1)^2 + \beta^2[(y - y_1)^2 + (z - z_1)^2]} \tag{76}$$

$$T \equiv \frac{1}{a_\infty \beta^2} \left[r_\beta - M_\infty(x - x_1)\right] \tag{77}$$

$$\beta^2 \equiv 1 - M_\infty^2 \tag{78}$$

The next steps involve mixing equations (70) and (75) in the Green's Theorem and solve for the potential φ at any point in space by means of an integral equation along the surfaces. The full mathematical procedure is extensive and is available in reference [38]. The final integral equation is the following:

$$4\pi E\varphi(x, y, z, t) = -\iint \left[\frac{\partial\varphi}{\partial n_1}\frac{1}{r_\beta}\right]^T \frac{|\nabla_1 S|^T}{|\nabla_1 S^T|} dS^T + \iint \left[\frac{\partial}{\partial n_1}\left(\frac{1}{r_\beta}\right)\varphi\right]^T \frac{|\nabla_1 S|^T}{|\nabla_1 S^T|} dS^T - \frac{\partial}{\partial t}\iint \left[\frac{\partial T}{\partial n_1}\frac{\varphi}{r_\beta}\right]^T \frac{|\nabla_1 S|^T}{|\nabla_1 S^T|} dS^T \tag{79}$$

The superscript T indicates evaluation at time $t_1 = t - T$ and E is defined as follows:

$$E = \begin{cases} 0 & \text{point inside the body} \\ 1 & \text{point outside the body} \\ \dfrac{1}{2} & \text{point on the surface} \end{cases} \tag{80}$$

Equation (79) is the starting point for any subsonic panel method, either steady or unsteady, time or frequency-domain.

Aerodynamic Modeling of Flutter Instability

In this section, equation (79) is simplified and reformulated in the frequency-domain in a form that is suitable for flutter calculations.

Panel method integral equation in the frequency domain

In the flutter analysis the main concern is the onset of the instability and not the exact time-dependent deformed shape of the body. It is assumed that the surface is free to oscillate around a steady state configuration and that the amplitudes are small. This allows evaluating the integrals on the steady configuration. With these assumptions the following simplifications take place:

$$|\nabla S|^T = |\nabla S^T| = |\nabla S| \tag{81}$$

$$\frac{\partial S}{\partial t} \neq 0 \tag{82}$$

$$S^T \equiv S(x, y, z, t) = S_S(x, y, z) + \varepsilon S_U(x, y, z)e^{st} \tag{83}$$

The parameter ε represents an amplitude that should be small and "s" is a complex number representing both harmonic (imaginary part) and exponential grow or decay (real part) of the amplitudes.

The next step is to re-write the normal perturbation velocity $\frac{\partial\varphi}{\partial n}$ in terms of the boundary condition (84) and equation (83). Impermeability requires that:

$$\frac{\partial \varphi}{\partial n} = -\frac{1}{U_\infty} \frac{1}{|\nabla S_S|} \frac{dS}{dt} \tag{84}$$

Since:

$$\frac{dS}{dt} = \frac{\partial S}{\partial t} + U_\infty \frac{\partial S}{\partial x} \tag{85}$$

Using equation (83), equation (84) can be re-written in the following way:

$$\frac{\partial \varphi}{\partial n} = -\frac{1}{U_\infty} \frac{1}{|\nabla S_S|} \left[\frac{\partial S_S}{\partial x} + \varepsilon \left(\frac{s}{U_\infty} S_U + \frac{\partial S_U}{\partial x}\right) e^{st}\right] = Q_{n,S} + Q_{n,U} \tag{86}$$

$$Q_{n,S} = -\frac{1}{|\nabla S_S|} \frac{\partial S_S}{\partial x} \tag{87}$$

$$Q_{n,U} = -\frac{\varepsilon}{|\nabla S_S|} \left(\frac{s}{U_\infty} S_U + \frac{\partial S_U}{\partial x}\right) e^{st} = \widetilde{Q}_n e^{st} \tag{88}$$

The potential φ can also be split in two contributions:

$$\varphi = \varphi_S + \varepsilon \widetilde{\varphi} e^{st} \tag{89}$$

Finally, equation (79) can be re-written using (83), (86) and (89). Noting that the resulting equation is linear in both φ_S and $\varepsilon\widetilde{\varphi}$, the steady and unsteady contributions can be treated independently, therefore defining two separate equations. For flutter calculations, only the unsteady equation needs to be solved because it is the only source of unsteady fluctuations in the potential. The unsteady integral equation in the frequency domain suitable for a panel method is the following:

$$2\pi\widetilde{\varphi}(x, y, z) = -\oiint \widetilde{Q}_n \frac{e^{-sT}}{r_\beta} dS_S + \oiint \widetilde{\varphi} \frac{\partial}{\partial n_1}\left(\frac{e^{-sT}}{r_\beta}\right) dS_S \tag{90}$$

The integrands $\frac{e^{-sT}}{r_\beta}$ and $\frac{\partial}{\partial n_1}\left(\frac{e^{-sT}}{r_\beta}\right)$ are called the unsteady subsonic <u>source</u> and <u>doublet</u> singularities respectively. Since the calculations are performed on the surface, the parameter E was set to ½. Computationally, it's convenient to perform the so-called Generalized Prandtl-Glauert transformation the previous equation:

$$x = \beta x_0, \qquad y = y_0, \qquad z = z_0, \qquad t = \frac{t_0}{\beta a_\infty}, \qquad s = \beta a_\infty s_0 \tag{91}$$

Resulting in the following final panel method equation:

$$2\pi\widehat{\varphi}(x_0, y_0, z_0) = -\oiint \widehat{Q}_n \frac{e^{-s_0 r_0}}{r_0} dS_{S0} + \oiint \widehat{\varphi} \frac{\partial}{\partial n_{01}}\left(\frac{e^{-s_0 r_0}}{r_0}\right) dS_{S0} \tag{92}$$

$$\widehat{\varphi} = \widetilde{\varphi} e^{-s_0 M x_0}, \quad \widehat{Q}_n = \widetilde{Q}_n e^{-s_0 M x_0} \tag{93}$$

$$r_0 = \sqrt{(x_0 - x_{01})^2 + (y_0 - y_{01})^2 + (z_0 - z_{01})^2} \tag{94}$$

In equation (92), the integral relation between the modified potential $\widehat{\varphi}$ and $\widehat{Q}_n$ is completely independent of the Mach number. In addition, the integrands became greatly simplified. All the

integrations are evaluated in the transformed surface $S_0(x_0, y_0, z_0)$, which is equivalent to the original surface S stretched in the x direction by a factor of $1/\beta$.

Definition of the Generalized Displacements

In the frequency domain, there is a need to write the surface function S in terms of several harmonics which are basically the translational DoFs in the (x, y, z) directions. In order to do so, the surface equation S is written in the following alternative way:

$$S = S_S + \Delta S \tag{95}$$

The term ΔS is an unsteady deviation from the equilibrium position S_S. Expanding S in Taylor series around S_S, we get:

$$S = S_S\left(x_S + \varepsilon d_x e^{st}, y_S + \varepsilon d_y e^{st}, z_S + \varepsilon d_z e^{st}\right) = S_S + \varepsilon \mathbf{d} \cdot \nabla S_S e^{st} + O(\varepsilon^2) \tag{96}$$

The vector $\mathbf{d}$ represents the above mentioned translational DoFs at each point of the surface. Comparing equations (96) and (83), one can infer the following expression for the unsteady surface S_U:

$$S_U(x, y, z) = \mathbf{d} \cdot \nabla S_S \tag{97}$$

Finally, the DoFs are introduced in the integral equation (92) through the modified normal perturbation speed $\widehat{Q}_n$, which depends explicitly on S_U:

$$\widehat{Q}_n = -\frac{\varepsilon}{|\nabla S_S|}\left(\frac{s}{U_\infty} S_U + \frac{\partial S_U}{\partial x}\right) e^{-s_0 M x_0} = -\frac{\beta}{M_\infty} s_0 \mathbf{n} \cdot \hat{\mathbf{d}} - \mathbf{n} \cdot \hat{\mathbf{d}}' \tag{98}$$

$$\hat{\mathbf{d}} = e^{-s_0 M_\infty x_0} \begin{Bmatrix} d_x \\ d_y \\ d_z \end{Bmatrix}, \quad \hat{\mathbf{d}}' = e^{-s_0 M_\infty x_0} \begin{Bmatrix} \dfrac{\partial d_x}{\partial x} \\ \dfrac{\partial d_y}{\partial x} \\ \dfrac{\partial d_z}{\partial x} \end{Bmatrix} \tag{99}$$

The derivatives in x direction $\hat{\mathbf{d}}'$ represent three rotational DoFs, which in conjunction with the translational ones define a set of 6 DoFs per point. The integral equation (92) becomes:

$$2\pi\widehat{\varphi}(x_0, y_0, z_0) = \oiint \left(\frac{\beta}{M} s_0 \mathbf{n} \cdot \hat{\mathbf{d}} + \mathbf{n} \cdot \hat{\mathbf{d}}'\right) \frac{e^{-s_0 r_0}}{r_0} dS_{S0} + \oiint \widehat{\varphi} \frac{\partial}{\partial n_{01}}\left(\frac{e^{-s_0 r_0}}{r_0}\right) dS_{S0} \tag{100}$$

This equation is the starting point for the computational implementation of the frequency-domain panel method.

Wake Modeling

The surface S_0 is the sum of two closed surfaces, the body and the wake:

$$S_0 = S_{B0} + S_{W0} \tag{101}$$

The wake is defined as a flat surface starting from the trailing edge of the wing and aligned with the free stream velocity $\mathbf{V}_\infty$. The wake is considered a free surface therefore it cannot sustain pressure forces. In other words:

$$\Delta p_{wake} = 0 \tag{102}$$

Expressing the pressure as the sum of a steady and unsteady contribution:

$$p(x, y, z, t) = p_S(x, y, z) + \varepsilon \tilde{p}(x, y, z) e^{st} \tag{103}$$

And recovering the linearized pressure equation (72), the pressure difference can be written in the frequency-domain:

$$\Delta \tilde{p}_{wake} = -\rho_\infty U_\infty \left(s \Delta \tilde{\varphi}_{wake} + U_\infty \frac{\partial \Delta \tilde{\varphi}_{wake}}{\partial x} \right) \tag{104}$$

Using the Prandtl-Glauert transformation and introducing (102), the following final relation is obtained:

$$e^{\frac{s_0 x_{0_{wake}}}{M_\infty}} \Delta \hat{\varphi}_{wake} = e^{\frac{s_0 x_{0_{TE}}}{M_\infty}} \Delta \hat{\varphi}_{TE} \tag{105}$$

The subscript "TE" refers to the trailing edge. This equation must be satisfied at every point of the wake.

4.2.2 Computational Implementation

In order to find the modified potential distribution $\hat{\varphi}$, and later the unsteady pressure $\tilde{p}$, equation (100) must be satisfied in the entire surface (physical) domain. Although the formulation until now is written in terms of the complex frequency "s", the remaining mathematical developments will be restricted to the simple harmonic motion $s = i\omega$. In addition, the frequency "ω" will be converted to its non-dimensional form "k", also known as the *reduced frequency*:

$$k = \frac{\omega c}{V_\infty} \tag{106}$$

The methodology is the following:

1. **Surface modeling**: both physical surfaces and wake are divided in several flat panels (quadrilaterals and/or triangles) and stored in arrays according to a proper numbering scheme
2. **Collocation**: for each panel, the coordinates of its centroid are stored in arrays. These define the collocation points where the unknown potential, aerodynamic DoFs and pressure will be calculated. Since they are assumed constant for each panel, these quantities can be taken out of the integrals
3. **Influence coefficients**: all integrals are now calculated for each panel individually and the integral equation (20) is transformed into a sum of integrals (107). Each integral can be interpreted as an influence coefficient of each panel singularity distribution in the potential at a certain control point
4. **Linear system of equations**: writing the integral equation for each collocation point on the body surface we obtain a linear system of equations with unknowns $\hat{\varphi}_i$ and $\hat{q}_k$ (113)

5. **Pressure scheme**: the pressure distribution can be obtained from the potential using the linearized pressure equation (72). By choosing an adequate finite difference scheme, a relation between the unsteady pressure $\tilde{p}_i$ and the modified aerodynamic DoFs $\hat{q}_k$ can be found (118)

6. **Coordinate transformation**: the modified aerodynamic DoFs $\hat{q}_k$ are converted to the physical ones $\tilde{q}_k$ using equation (99), resulting in equation (120) for the unsteady pressure

7. **Aerodynamic force array**: finally, the normal force array $\{\tilde{F}_n\}$ can be obtained by multiplying the vector $\tilde{p}_i$ by each panel area (121) and through a rotation matrix, a new vector $\{\tilde{F}\}$ is created containing the Cartesian components the pressure force for each panel (122)

4.2.2.1 Discretized Integral Equations

Computational form of the integral equation (100):

$$2\pi\hat{\varphi}_i = \sum_{j=1}^{N_B} \iint \frac{e^{-i\omega_0(M,k)r_0^{ij}}}{r_0^{ij}} dS_{S0}^j \left(i\frac{k}{c}\mathbf{n}\cdot\hat{\mathbf{d}} + \mathbf{n}\cdot\hat{\mathbf{d}}'\right)_j + \sum_{j=1}^{N_B+N_W} \iint \frac{\partial}{\partial n_{01}^j}\left(\frac{e^{-i\omega_0(M,k)r_0^{ij}}}{r_0^{ij}}\right) dS_{S0}^j \, \hat{\varphi}_j \tag{107}$$

Definitions:

$$B_{ij} \equiv \iint \frac{e^{-i\omega_0(M,k)r_0^{ij}}}{r_0^{ij}} dS_{S0}^j \quad C_{ij} \equiv \iint \frac{\partial}{\partial n_{01}^j}\left(\frac{e^{-i\omega_0(M,k)r_0^{ij}}}{r_0^{ij}}\right) dS_{S0}^j \tag{108}$$

$$\hat{Q}_n^j = -\left(i\frac{k}{c}\mathbf{n}\cdot\hat{\mathbf{d}} + \mathbf{n}\cdot\hat{\mathbf{d}}'\right)_j \equiv -D_{jk}\hat{q}_k \tag{109}$$

$$\omega_0(M,k) \equiv \frac{Mk}{c\beta} \tag{110}$$

$$D_{jk}\hat{q}_k \equiv \begin{bmatrix} [n]_1 & 0 & \dots & 0 \\ 0 & [n]_2 & \dots & 0 \\ \vdots & \vdots & \ddots & \vdots \\ 0 & 0 & 0 & [n]_{N_B} \end{bmatrix} \begin{Bmatrix} \{\hat{d}\}_1 \\ \{\hat{d}\}_2 \\ \vdots \\ \{\hat{d}\}_{N_B} \end{Bmatrix} \tag{111}$$

$$[n]_1 \equiv \begin{bmatrix} i\frac{k}{c}n_x & i\frac{k}{c}n_y & i\frac{k}{c}n_z & n_x & n_y & n_z \end{bmatrix}_1, \quad \{\hat{d}\}_1 = \begin{Bmatrix} \hat{d}_x \\ \hat{d}_y \\ \hat{d}_z \\ \hat{d}_x' \\ \hat{d}_y' \\ \hat{d}_z' \end{Bmatrix}_1 = \begin{Bmatrix} \hat{q}_1 \\ \hat{q}_2 \\ \hat{q}_3 \\ \hat{q}_4 \\ \hat{q}_5 \\ \hat{q}_6 \end{Bmatrix} \tag{112}$$

N_B, N_W are the total number of panels in the body and the wake respectively. Re-writing eq. (107):

$$2\pi\hat{\varphi}_i = \sum_{j=1}^{N_B} B_{ij}D_{ik}\hat{q}_k + \sum_{j=1}^{N_B+N_W} C_{ij}\hat{\varphi}_j \tag{113}$$

Solving for the modified potential and writing in vector form we have:

$$\left[4\pi[I] - [C]\right]\{\hat{\varphi}\} = [B][D]\{\hat{q}_A\} \tag{114}$$

- [I] is the identity matrix NB X NB

- [C] is the doublet matrix NB X (NB + NW)
- [B] is the source matrix NB X NB
- [D] is the DoF matrix NB X 6NB[2]
- $\{\widehat{\varphi}\}$ is the vector of the modified potential (NB + NW) X 1
- $\{\hat{q}_A\}$ is the vector of the aerodynamic DoFs 6NB X 1

Note: this equation is written before the wake treatment. The wake points (NW) do not bear additional unknowns as they are related to the trailing edge through equation (105). Afterwards the doublet's matrix C becomes square (NB x NB) and the potential is calculated on the wing surface only (NB points).

4.2.2.2 Aerodynamic Force Vector

The aerodynamic force vector contains the components of the pressure force on each control point and is written in terms of the aerodynamic DoFs by a coefficient's matrix. This is the final step concerning the implementation of the aerodynamic model.

Re-writing the pressure equation (72) in the frequency domain and performing the Prandtl-Glauert transformation (91), the unsteady pressure becomes:

$$\tilde{p} = -\rho_\infty U_\infty^2 \left(i\frac{k}{c}\left(\widehat{\varphi}e^{i\omega_0(M_\infty,k)M_\infty x_0}\right) + \frac{1}{\beta}\frac{\partial\left(\widehat{\varphi}e^{i\omega_0(M_\infty,k)M_\infty x_0}\right)}{\partial x_0} \right) \tag{115}$$

$$\Leftrightarrow \tilde{p} = -\frac{1}{2}\rho_\infty U_\infty^2 * \left(\frac{2ik}{c}\left(1 + \left(\frac{M_\infty}{\beta}\right)^2\right)\widehat{\varphi}e^{i\omega_0(M_\infty,k)M_\infty x_0} + \frac{2}{\beta}\frac{\partial\widehat{\varphi}}{\partial x_0}e^{i\omega_0(M_\infty,k)M_\infty x_0}\right) \tag{116}$$

The x_0 derivative can be approximated by a finite difference rule. For subsonic flow, an adequate formula is a central difference:

$$\frac{\partial\widehat{\varphi}}{\partial x_0} = \frac{\widehat{\varphi}_{i+1} - \widehat{\varphi}_{i-1}}{x_{0_{i+1}} - x_{0_{i-1}}} + O(\varepsilon^2) \tag{117}$$

This formula is second order accurate on a uniform mesh and has been implemented on every control point of the wing. An exception occurs at the leading and trailing edge control points where forward and backwards first order differences have been implemented, respectively. Independently of the rule used, it is always possible to write a relation between the pressure and the potential by means of a coefficient matrix:

$$\{\tilde{p}\} = -\frac{1}{2}\rho_\infty U_\infty^2 * [P]\{\widehat{\varphi}\} \tag{118}$$

Inserting equation (114) into (118) the following numeric expression is obtained:

$$\{\tilde{p}\} = -\frac{1}{2}\rho_\infty U_\infty^2 * [P]\{\widehat{\varphi}\} = -\frac{1}{2}\rho_\infty U_\infty^2 * [P][2\pi[I] - [C]]^{-1}[B][D]\{\hat{q}_A\} \tag{119}$$

---

[2] Matrix [D] is called [D_aux] in the code

The modified aerodynamic DoFs $\{\hat{q}_A\}$ can be transformed into the physical ones $\{\tilde{q}_A\}$ according to equation (99). The resulting coefficient matrix is called $[A]$ and expresses final relation between the unsteady pressure at each panel and the several aerodynamic DoFs:

$$\{\tilde{p}\} = -\frac{1}{2}\rho_\infty U_\infty^2 * [A]\{\tilde{q}_A\} \tag{120}$$

The unsteady normal force is directly obtained by multiplying the unsteady pressure by each panel surface area:

$$\{\tilde{F}_n\} = [S]\{\tilde{p}\} = -\frac{1}{2}\rho_\infty U_\infty^2 * [S][A]\{\tilde{q}_A\}$$
$$[S] \equiv \begin{bmatrix} A_1 & 0 & ... & 0 \\ 0 & A_2 & ... & 0 \\ \vdots & \vdots & \ddots & \vdots \\ 0 & 0 & 0 & A_{N_B} \end{bmatrix} \tag{121}$$

The normal force is then projected in the (x,y,z) directions by means of a rotation matrix $[R]$:

$$\{\tilde{F}\} = -\frac{1}{2}\rho_\infty U_\infty^2 * (-1) * [R]\{\tilde{F}_n\} = \frac{1}{2}\rho_\infty U_\infty^2 * [R][S][A]\{\tilde{q}_A\} \tag{122}$$

The extra -1 factor establishes the pressure force convention of being positive when pointing into the body, in the direction opposite to the exterior surface normal. The matrix [R] is 3NB X 6NB, [A] is NB X 6NB (after the wake treatment) and $\{\tilde{F}\}$ is 3NB X 1. This concludes the definition of the aerodynamic force and the aerodynamic modeling phase.

4.3 STRUCTURAL MODEL

The structural model used in this work consists in a single one dimensional straight beam that coincides with the wing elastic axis (Figure 7 – red line). It is assumed that the whole rigidity of the wing is concentrated along this beam and that the structural nodes are exactly at the midpoints of the spanwise panels (Figure 7 – red squares). The structure is modeled using the finite element software ANSYS® and both stiffness and mass matrices are extracted and stored in a file.
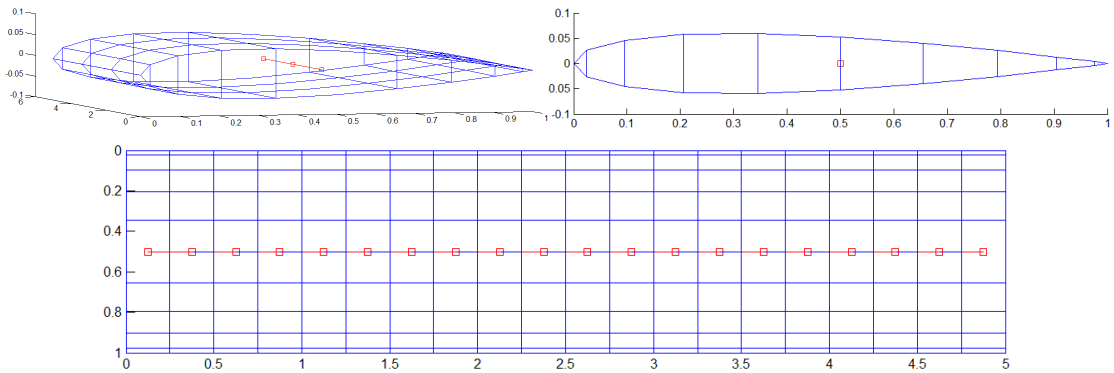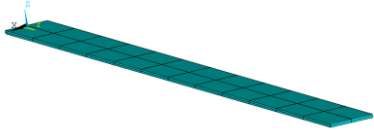
*Figure 7: illustration of both aerodynamic and structural meshes. Top **left** – perspective view with 3 structural nodes; Top **right** – side view; **Bottom** – top view with 20 structural nodes. The structural nodes (red squares) are always located at the center of each panel along the spanwise direction and on the mean surface (camber)*

4.3.1   Computational Setup in ANSYS

*Table 2: geometrical and structural proprieties of the structural model using ANSYS®. The words written in **bold** refer to variables used in the ANSYS® input file "structural_analysis_wing.txt"*

Geometry		Length	**span**
		Sweep Angle	**beta**
		Cross Section	"sectype,1,beam,rect,,0" "secdata,b,h"
		Section Inertias	$I_{xx} = \dfrac{1}{12} bh^3$
			$I_{zz} = \dfrac{1}{12} b^3 h$
		Torsion Constant	$J \approx bh^3 \left(\dfrac{1}{3} - 0.21 \dfrac{h}{b} \left(1 - \dfrac{1}{12} \left(\dfrac{h}{b} \right)^4 \right) \right)$
		Nº of active nodes	**NDIV**
		Number of nodes	**NDIV** + 1
Element Type	BEAM 188 "ET,1,beam188"	Theory	1st order shear theory
		Shape functions	Linear (default)
		Boundary Conditions	All DoFs zero at y=0 "d,1,all,0"
Material Proprieties (linear isotropic)	Density	**rho**	"MP,dens,1,**rho**"
	Young's Modulus	**E**	"MP,EX,1,**E**"
	Shear Modulus	**G**	"MP,GXY,1,**G**"
	Poisson's Ratio	**poisson**	"MP,PRXY,1,**poisson**"
	Flapwise Rigidity	**EIx**	$E * I_{xx}$
	Lagwise Rigidity	**EIz**	$E * I_{zz}$
	Torsional Rigidity	**GJ**	$G * J$
Analysis Type [43]	Substructuring/CMS "antype,substr"	Structural matrices	Stiffness [K], Mass [M] "seopt,file,3,1,0,0"
		Master DoFs	All DoFs "m,all,all"
	Modal "antype,modal"	Nº of modes	20
		Method	Block Lanczos "modopt,lanb,20,0,0,,off"

The BEAM188 is a one-dimensional beam element formulated with a first order shear deformation theory (Timoshenko – FSDT) with 6 DoFs per node [44]. This consists in a simplification of the real wing and some 3D effects such as chordwise deflections cannot be predicted. One dimensional beam theories are suitable for bodies whose natural frequencies are close to those of beams with equivalent bending rigidity. Examples of these bodies include high aspect ratio wings with uniform material proprieties.
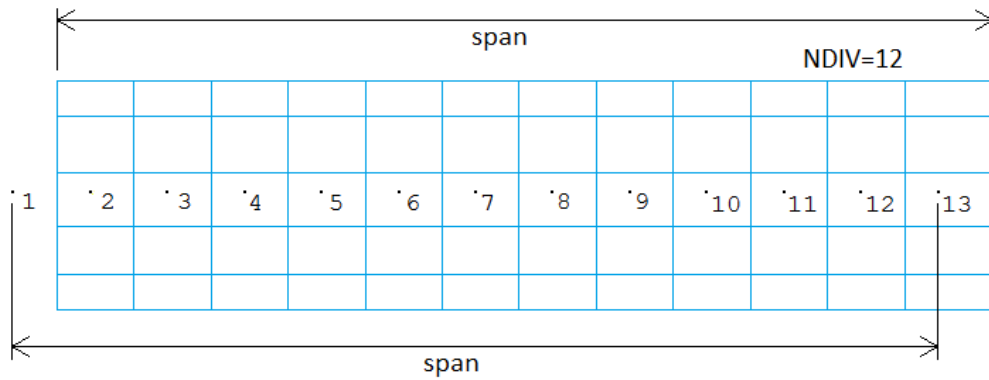
Figure 8: numbering scheme of the structural mesh used in ANSYS and its relative position to the aerodynamic mesh (blue)

There is an additional node, not present in the aerodynamic model. This extra node defines the zero displacement + rotation boundary condition and physically represents the intersection of the wing with the fuselage (see Figure 8). It is assumed that the wing is perfectly clamped in the fuselage.

The goal of the structural analysis is to extract information about the first natural modes and the structural stiffness and mass matrices, K and M respectively. The extracted data is then written on a text file to be read by the MATLAB® script. For this, ANSYS® must run read an *.txt file called "structural_analysis_wing.txt" containing the detailed information for each specific analysis. The structural analysis can be organized in the following steps:

1. ANSYS® reads input *.inp file containing the structural analysis
   1.1. Create (nseg_Y+1) BEAM188 nodes evenly spaced along the specified wing span length
   1.2. Define the material proprieties: Young's modulus, density, Poisson coefficient
   1.3. Define the geometrical proprieties: cross-section dimensions and area inertias
   1.4. Apply zero displacements and rotations boundary condition at the first node
   1.5. Run the modal analysis
   1.6. Extract the stiffness and mass matrices (substructuring analysis option)
   1.7. Write the structural matrices into a *.txt file
2. MATLAB® reads the *.txt files and stores the structural matrices into variables

It is recommended to read the program's manual[3] before attempting to run the structural or aerodynamic analysis. It contains a detailed description of the code in both ANSYS® and MATLAB® files.

4.4 AEROELASTIC ANALYSIS

The aeroelastic analysis couples both aerodynamic and structural analysis. In this work, the ultimate goal of the aeroelastic calculations is the determination of the wing's flutter speed. For this, the aeroelastic stability equation (3) needs to be obtained and solved for several free stream velocities. Since this equation is formulated in the structural mesh involving the structural DoFs, the aerodynamic loads and DoFs must be transferred to the structural nodes. The stability equation corresponds to a

---

[3] Document available on request: eduardo.pizarro@tecnico.ulisboa.pt

non-linear eigenvalue problem and is solved iteratively according to a frequency matching method based on the p-k method.

4.4.1 Equivalent Force System

The aerodynamic pressure forces are transferred into the structural nodes and its respective moments are calculated to constitute the equivalent force system as D'Alembert's principle requires (see Figure 9).
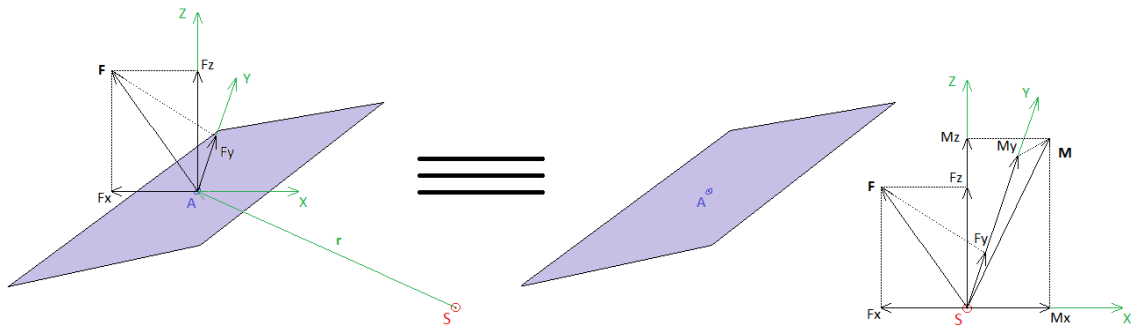
Figure 9: schematics of the pressure force acting on a panel and its equivalent force system on the nearby structural node

In the force transfer procedure, only the forces acting on the ring of panels surrounding the structural node are transferred. An exception occurs at the last structural node where there is an additional contribution of the tip panels. Likewise, the 3 orthogonal unsteady moments generated by the pressure forces on each panel are calculated and stored at each structural node.

4.4.2 Rigid DoFs Transformation

The aerodynamic DoFs are converted into the structural ones using a suitable coordinate transformation. Since the beam is the only true deformable body, the aerodynamic nodes on the wing are only allowed to follow the structural ones in a rigid manner. Therefore it is assumed that every control point on the wing surface is rigidly connected to the structural nodes by an infinite stiff invisible beam. These virtual beams are depicted as green lines in Figure 10. Similar to the force transfer system, each ring of panels transforms its aerodynamic DoFs into the structural DoFs of the nearest structural node only.
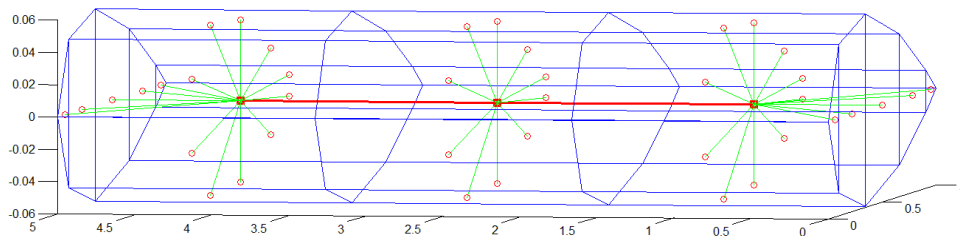
Figure 10: Rigid connections (green lines) between each structural node (red squares) and the aerodynamic ones (red circles).

The aerodynamic DoFs are related to the structural DoFs by the following matrix that represents a rigid rotation considering small amplitudes:

$$
\left\{ \begin{matrix} u \\ v \\ w \end{matrix} \right\}_A = \begin{bmatrix} 1 & 0 & 0 & 0 & z_S & -y_S \\ 0 & 1 & 0 & -z_S & 0 & x_S \\ 0 & 0 & 1 & y_S & -x_S & 0 \end{bmatrix} \left\{ \begin{matrix} u \\ v \\ w \\ \phi_x \\ \phi_y \\ \phi_z \end{matrix} \right\}_S
\tag{123}
$$

- The subscript "A" refers to the aerodynamic DoFs and "S" to the structural ones
- z_S refers to the "z" coordinate of an aerodynamic control point measured in a frame originating in a certain structural node. This local coordinate system is the same for all panels of the same ring of panels
- Only half of the matrix is shown here. The other 3 aerodynamic DoFs (u'_A, v'_A, w'_A) are related to the structural DoFs by finite differences formulas involving (u_A, v_A, w_A) of different panels
- Each panel requires a 6x6 matrix for DoFs compatibility and the full compatibility matrix has dimensions equal to the total number of aerodynamic DoFs times the total number of structural DoFs

4.4.3 The Aerodynamic Influence Coefficient's matrix (AIC)

In this section, the computational procedure that leads to the definition of the AIC matrix is briefly explained. At the end of the aerodynamic calculations (4.2.2.2), the vector containing the unsteady forces in the 3 orthogonal directions at each panel is obtained. These forces are expressed in terms of the aerodynamic DoFs via the product of the rotation matrix [R], the area matrix [S] and the unsteady pressure matrix [A]. Since the aeroelastic calculations are performed in the structural nodes, both aerodynamic DoFs and forces must be transported to these nodes. The DoFs transformation can be achieved by multiplying the rotation matrix [T] introduced in section 4.4.2:

$$
\{\tilde{q}_A\} = [T]\{\tilde{q}_S\}
\tag{124}
$$

$$
\{\tilde{F}_A\} = [R][S][A]\{\tilde{q}_A\} = [R][S][A][T]\{\tilde{q}_S\}
\tag{125}
$$

Note that these forces are still on the aerodynamic mesh (panels' centers). The next step is to transfer the forces from the panels to the structural nodes. Doing so requires calculating the resultant force and moment in each structural node according to D'Alembert's Principle (see section 4.4.1). Once the forces and moments are calculated in the structural nodes and are expressed in terms of the structural DoFs, the AIC matrix is completely defined:

$$
\{\tilde{F}\} = [AIC]\{\tilde{q}\}
\tag{126}
$$

This is the matrix that figures in the aeroelastic stability equation (3). Each row of this matrix measures a component of the unsteady aerodynamic force or moment on a structural node, and each column the influence of a particular structural DoF on the forces and moments. The AIC matrix is a complex matrix with size (6x"nseg_Y" x 6x"nseg_Y").

4.4.4   Modified p-k Method

The p-k method is an iterative process for solving the non-linear eigenvalue problem that arises from aeroelastic flutter problems. In its simplest form, the flutter equation is the following [29]:

$$\left[\left(\frac{U_\infty}{c^2}\right)[M]p^2 + [K] + \frac{1}{2}\rho_\infty U_\infty^2[AIC(ik, M_\infty)]\right]\{\tilde{q}\} = 0 \tag{127}$$

$$p = k(\gamma + i) \tag{128}$$

$$s = \omega(\gamma + i) = \frac{U_\infty}{c}p \tag{129}$$

- [M] and [K] are the wing's mass and stiffness matrix respectively
- [AIC] is the complex aerodynamic influence coefficients' matrix
- "p" is the non-dimensional complex eigenvalue and also the solution of the equation
- "s" is the dimensional complex eigenvalue solution of the equation (rad/s)
- "ω" is the circular frequency (rad/s)
- "k" is the reduced frequency and the imaginary part of "p"
- "γ" represents the damping of the system and is often referred as the rate of decay

The procedure involves reducing to a standard quadratic eigenvalue problem in "p" by injecting a frequency "k" in the pure non-linear part of the equation (aerodynamics), and solving iteratively until the imaginary part of "p" matches "k". This is referred as the so-called frequency matching process [27].

A more practical way of solving the flutter equation is to write it in the form of a structural damped modal equation by the inclusion of an aerodynamic damping matrix [24] (page 396). Such can be achieved by first isolating the term containing the imaginary part of matrix [AIC]:

$$\frac{1}{2}\rho_\infty V_\infty * U_\infty i[AIC_I] = \frac{1}{2}\rho_\infty U_\infty * \frac{c\omega}{k}i[AIC_I] \overset{s=i\omega}{=} \frac{1}{2}\rho_\infty U_\infty * \frac{cs}{k}[AIC_I] = \frac{1}{2}\rho_\infty U_\infty^2 * \frac{p}{k}[AIC_I] \tag{130}$$

The "p" eigenvalue was originated from the aerodynamics by assuming a non-damped (simple harmonic) solution. Introducing this term in the flutter equation yields:

$$\left[\left(\frac{U_\infty^2}{c^2}\right)[M]p^2 + \frac{1}{2}\rho_\infty U_\infty^2 \frac{1}{k}[AIC_I(ik)]p + [K] + \frac{1}{2}\rho_\infty U_\infty^2[AIC_R(ik)]\right]\{\tilde{q}\} = 0 \tag{131}$$

Since the aerodynamic matrix [AIC] is calculated assuming $p = ik$ while the solution "p" is allowed to be damped, this flutter equation is only exactly satisfied when $\text{Re}\{p\} = 0$. For all other cases this method is mathematically inconsistent. However, according to most researchers in the field, it provides a good estimate of the behavior of the damping around the flutter boundary $\text{Re}\{p\} = 0$ and it is considered superior and more cost-efficient in relation to other methods.

For a given flight condition (U_∞, ρ_∞), and for a given reduced frequency k^j, the quadratic eigenvalue problem in p^{j+1} is solved. Usually, the first guess for k^j corresponds to one of the system's natural frequencies. The solution is always in the form of conjugate complex pairs of eigenvalues and eigenvectors:

$$p^{j+1} = k^{j+1}(\gamma^{j+1} \pm i)$$
$$\{\overline{V}\} = \{V, V^*\} \tag{132}$$

In the standard p-k method, the process converges when k^{j+1} matches k^j with less than a small error. Then the real part of "p" is stored and another iterative process starts for a different reduced frequency. When all frequencies of interest are converged, the flight condition is altered and the full process is repeated until the flutter boundary is reached.

The actual method used in this work is slightly different from the traditional p-k method concerning the frequency matching procedure. The "Modified p-k Method" does not rely exclusively on the relative error between the new and the previous reduced frequencies for eigenvalue convergence. Instead, the amplitudes of the several eigenvectors are inspected and only those whose shape and DoFs match those of the guessed frequency are eligible for comparison. This avoids tracking the wrong mode in consecutive iterations or between two different flight speeds, especially when two or more of the wing natural frequencies are closely spaced.

The measurement of the modes' amplitudes is explained next. Each non-trivial solution of the flutter equation is a linear combination of pair of conjugate eigenvectors (V, V^*) and eigenvalues (p, p^*):

$$\{q\} = \{V\}e^{pt} + \{V^*\}e^{p^*t} = \{A + Bi\}e^{at}e^{ibt} + \{A - Bi\}e^{at}e^{-ibt} = 2e^{at} * (\{A\}\cos bt - \{B\}\sin bt) \tag{133}$$

For a given frequency and for all time, the solution is a combination of a sine and a cosine affected by a decaying (stable) or growing (unstable) exponential. The mode shape is independent of time and it's given by vectors {A} and {B} which correspond to the real and imaginary parts, respectively, of the eigenvector {V}. Each mode is characterized by its "code", which consists in the dominant DoF and the number of peaks or mode order number. The candidate frequencies are selected upon detecting these characteristics on the modal amplitudes in vectors {A} or {B}, of each extracted eigenvector. In summary, the modified p-k method involves three steps:

1. **Mode amplitude inspection**: the amplitudes of the extracted modes corresponding to the DoF of the injected frequency "k" (active DoF) are stored. These modes are referred to either vector {A} or {B}, whichever the amplitude is the greatest

2. **Mode shape detection**: the order numbers of the modes from step 1 are stored. These numbers are obtained by calculating the number of times each mode curve crosses the horizontal axis and are representative of its shape

3. **Mode candidate selection**: the modes whose orders' numbers match those of the active mode are stored, and the one whose amplitude is the greatest is selected as best candidate

After finding the best candidate, the relative error between the old "k" and the new one is calculated and the whole process is repeated until convergence. The full modified p-k method is illustrated in the flowchart of Figure 11:
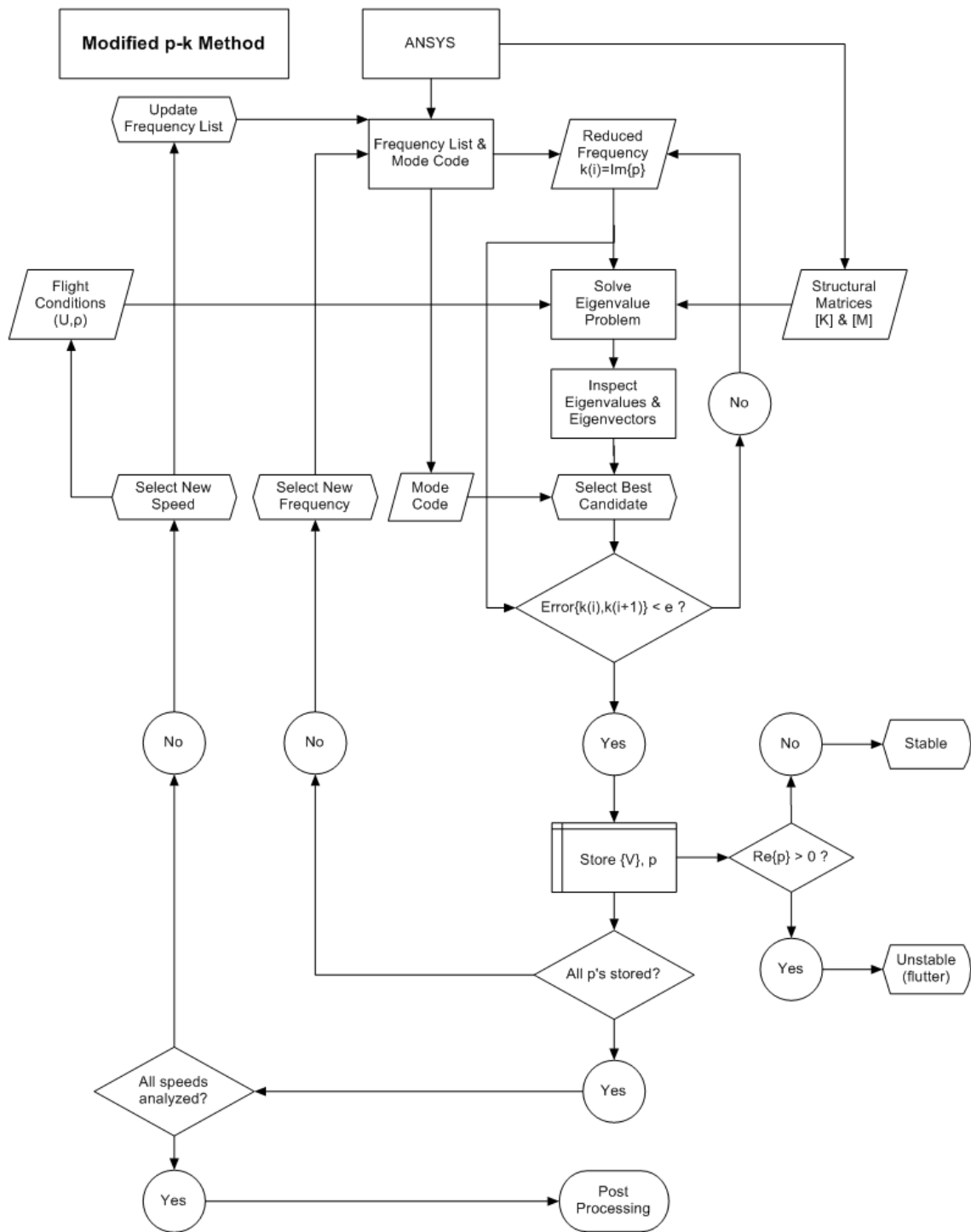
Figure 11: flowchart depicting the several stages and processes involved in the modified p-k method for flutter speed determination

5 CONVERGENCE STUDY

A convergence study is necessary in order to gain some insight about the quality of the mesh used. There are two main parameters that determine the accuracy of the solution: the number of integration points and the number of panels. The former is required because the integrals are performed by pure numerical means and should be analyzed in the first place. The latter is highly dependent on the surface geometry and must only be studied once the integrals are considered accurate enough.

5.1 THE EFFECT OF THE NUMBER OF INTEGRATION POINTS

There are two rules of numerical integration used in this work:

1. **Trapezium Rule**: this direct method of integration is only used in the triangular panels and in the case of self-influence, i.e., when the integration is over the influencing panel itself. This is also a singular integral and is performed in polar coordinates (see Appendix A)
2. **Gauss Quadrature**: the integration is performed in the reference geometry (a square) and it is usually much faster than the previous rule

The model used is the high aspect ratio wing from reference [30] and a rather coarse mesh was chosen. The number of points for each element is independent of its size therefore bigger elements in a coarse mesh may suffice for the purpose of this study. A frequency corresponding to the fourth structural mode in magnitude (1st torsion) was selected for being representative of a highly oscillating mode. The wing and all the relevant parameters are specified in the following table:

Table 3: computational setup for the convergence study

Computational Setup			
Airfoil	NACA 0012		
Aspect Ratio	24	U_∞	20 m/s
Sweep angle	0°		
Chord	1 m		
Semi-span	16 m	ρ_∞	0.088 kg/m^3
"nseg_X"	5		
"nseg_Y"	5	**Number of**	**Matrix B**	**Matrix C**
"nseg_wake"	0	**integration points**	[5, 150]	[5, 300]
Frequency		31.54 rad/s	

The influence of the number of integration points is measured by calculating the variations in the entries of the source and doublets matrices B and C, respectively, while increasing the number of points from 5 to 300. These matrices are the key elements for this analysis because they store every integral performed by the program. The procedure is the following:

1. For each number of integration points, both matrices (B and C) are stored into two arrays of matrices
2. The real and imaginary parts are stored into new arrays of matrices
3. The relative variation of both real and imaginary parts of both matrices with respect to the previous number of integration points is stored in 4 final arrays of matrices

4. The relative variations of a selection of entries are inspected and studied in detail

5.1.1 The Source Integrals Matrix – B

```
>> BR_ERROR_III(1:12,1:12,1)
```

	1st ring of panels		2nd ring of panels
	upper side	lower side	upper side
-18.0158 -40.7699 -4.8094 -0.6178 -0.2023	-0.2019 -0.6105 -4.5819 -33.3083 -71.6086	0.0003 0.0003
-30.2595 -6.4923 -16.9512 -1.6718 -0.5049	-0.5018 -1.6059 -13.1475 -40.4737 -26.3890	0.0003 0.0003
-3.5873 -13.5206 -4.0043 -13.1285 -3.1214	-3.0862 -11.6850 -37.5078 -11.2423 -3.4552	0.0001 0.0002
-0.5523 -1.6459 -16.0072 -6.0666 -27.5835	-26.9397 -56.2693 -14.3801 -1.5890 -0.5466	-0.0000 0.0000
-0.2011 -0.5532 -4.1320 -37.7854 -16.8519	-84.9702 -36.8051 -4.0860 -0.5499 -0.2007	-0.0001 -0.0000
-0.2007 -0.5499 -4.0860 -36.8051 -84.9702	-16.8519 -37.7854 -4.1320 -0.5532 -0.2011	-0.0001 -0.0000
-0.5466 -1.5890 -14.3801 -56.2693 -26.9397	-27.5835 -6.0666 -16.0072 -1.6459 -0.5523	-0.0000 0.0000
-3.4552 -11.2423 -37.5078 -11.6850 -3.0862	-3.1214 -13.1285 -4.0043 -13.5206 -3.5873	0.0001 0.0002
-26.3890 -40.4737 -13.1475 -1.6059 -0.5018	-0.5049 -1.6718 -16.9512 -6.4923 -30.2595	0.0003 0.0003
-71.6086 -33.3083 -4.5819 -0.6105 -0.2019	-0.2023 -0.6178 -4.8094 -40.7699 -18.0158	0.0003 0.0003
0.0003 0.0003 0.0001 -0.0000 -0.0001	-0.0001 -0.0000 0.0001 0.0003 0.0003	-18.0158 -40.7699
0.0003 0.0003 0.0002 0.0000 -0.0000	-0.0000 0.0000 0.0002 0.0003 0.0003	-30.2595 -6.4923

```
>> BI_ERROR_III(1:12,1:12,1)
```

	1st ring of panels		2nd ring of panels
	upper side	lower side	upper side
-35.1912 0.0000 -0.0000 -0.0000 -0.0000	-0.0000 -0.0000 -0.0000 -0.0000 0.0000	-0.0000 0.0000
0 -17.9245 -0.0000 -0.0000 0	0 0.0000 -0.0000 0.0000 -0.0000	0.0000 0.0000
-0.0000 -0.0000 -11.8720 -0.0000 -0.0000	0.0000 -0.0000 0 -0.0000 -0.0000	-0.0000 0
0 -0.0000 -0.0000 -16.9691 -0.0000	0 0.0000 -0.0000 -0.0000 -0.0000	-0.0000 0
-0.0000 -0.0000 -0.0000 0 -33.9949	0.0000 0.0000 -0.0000 -0.0000 -0.0000	0.0000 0
-0.0000 -0.0000 -0.0000 0.0000 0.0000	-33.9949 0 -0.0000 -0.0000 -0.0000	0.0000 -0.0000
-0.0000 -0.0000 -0.0000 0.0000 0	-0.0000 -16.9691 -0.0000 -0.0000 0	0.0000 0
-0.0000 -0.0000 0 -0.0000 0.0000	-0.0000 -0.0000 -11.8720 -0.0000 -0.0000	-0.0000 0
-0.0000 0.0000 -0.0000 0.0000 0	0 -0.0000 -0.0000 -17.9245 0	0.0000 -0.0000
0.0000 -0.0000 -0.0000 -0.0000 -0.0000	-0.0000 -0.0000 -0.0000 0.0000 -35.1912	-0.0000 -0.0000
-0.0000 0 -0.0000 0.0000 -0.0000	0 0.0000 0.0000 -0.0000 0	-35.1912 0.0000
0 0.0000 -0.0000 0.0000 0.0000	-0.0000 -0.0000 0.0000 -0.0000 0.0000	0 -17.9245

*Figure 12: relative variations of the real (**upper**) and imaginary (**lower**) parts of the entries of matrix B calculated with n_div=10 integration points with respect to the case with n_div=5*

The numbers in Figure 12 represent the variation in percentage of the real and imaginary parts of matrix B with n_div=10 with respect to the same matrix computed with only 5 integration points. Although most of the variations are quite large, one can observe that even with a few integration points, several of the entries have a negligible variation. The variations are larger in the diagonal (self-induction) and between adjacent panels. A rough estimate of the behavior of the increments with the distance indicates that a gap of two or more panels provides variations inferior to 1% when using just 5 integration points. Also, the variations are approximately zero between panels of different rings (spaced in the Y direction), as the numbers covered by the green lines suggest. This is not relevant because in this particular case, the spanwise array of panels are very narrow and its centers highly spaced, giving rise to slow varying integrands near the influenced panels. The imaginary part of B (Figure 12 - bottom) requires special attention: the entries only seem to change along the diagonal being the remainder very close to zero. The same matrices for 60 integration points are repeated in Figure 13 below:

```
>> BR_ERROR_III(1:12,1:12,6)
```

	1st ring of panels		2nd ring of panels
	upper side	lower side	upper side
-0.2408 0.0937 0.0000 0.0000 -0.0000	-0.0000 -0.0000 0.0000 0.0202 [0.8697]	-0.0000 -0.0000
0.0024 -0.0413 0.0007 0.0000 -0.0000	-0.0000 0.0000 0.0001 0.0152 0.0006	-0.0000 -0.0000
0.0000 0.0000 -0.0216 0.0000 0.0000	0.0000 0.0000 0.0125 0.0000 0.0000	-0.0000 0.0000
-0.0000 0.0000 0.0005 -0.0375 0.0014	0.0011 [0.2080] 0.0002 -0.0000 -0.0000	-0.0000 -0.0000
0.0000 0.0000 0.0000 0.0686 -0.2088	[2.0861] 0.0575 0.0000 -0.0000 0.0000	-0.0000 -0.0000
0.0000 -0.0000 0.0000 0.0575 2.0861	-0.2088 0.0686 0.0000 0.0000 0.0000	-0.0000 -0.0000
0.0000 -0.0000 0.0002 0.2080 0.0011	0.0014 -0.0375 0.0005 0.0000 -0.0000	-0.0000 -0.0000
0.0000 0.0000 0.0125 0.0000 0.0000	0.0000 0.0000 -0.0216 0.0000 0.0000	-0.0000 -0.0000
0.0006 0.0152 0.0001 0.0000 -0.0000	-0.0000 0.0000 0.0007 -0.0413 0.0024	-0.0000 -0.0000
0.8697 0.0202 0.0000 -0.0000 -0.0000	-0.0000 0.0000 0.0000 0.0937 -0.2408	-0.0000 -0.0000
-0.0000 -0.0000 -0.0000 -0.0000 -0.0000	-0.0000 -0.0000 -0.0000 -0.0000 -0.0000	-0.2408 0.0937
-0.0000 -0.0000 -0.0000 -0.0000 -0.0000	-0.0000 -0.0000 -0.0000 -0.0000 -0.0000	0.0024 -0.0413

```
>> BI_ERROR_III(1:12,1:12,6)
```

| 1st ring of panels | | | | | | | | | | 2nd ring of panels | |
upper side					lower side					upper side	
-1.1620	-0.0000	-0.0000	-0.0000	-0.0000	-0.0000	-0.0000	-0.0000	-0.0000	0.0000	-0.0000	-0.0000
-0.0000	-0.1765	-0.0000	-0.0000	0.0000	-0.0000	-0.0000	-0.0000	-0.0000	-0.0000	0.0000	-0.0000
-0.0000	0.0000	-0.0856	-0.0000	-0.0000	-0.0000	-0.0000	-0.0000	-0.0000	-0.0000	-0.0000	-0.0000
-0.0000	-0.0000	-0.0000	-0.1587	-0.0000	-0.0000	-0.0000	-0.0000	-0.0000	-0.0000	-0.0000	0.0000
-0.0000	-0.0000	-0.0000	-0.0000	-1.0048	-0.0000	-0.0000	-0.0000	-0.0000	-0.0000	-0.0000	-0.0000
-0.0000	-0.0000	-0.0000	-0.0000	-0.0000	-1.0048	-0.0000	-0.0000	-0.0000	-0.0000	-0.0000	-0.0000
-0.0000	-0.0000	-0.0000	-0.0000	-0.0000	-0.0000	-0.1587	-0.0000	-0.0000	-0.0000	0.0000	-0.0000
-0.0000	-0.0000	-0.0000	-0.0000	-0.0000	-0.0000	-0.0000	-0.0856	0.0000	-0.0000	-0.0000	-0.0000
-0.0000	-0.0000	-0.0000	-0.0000	0.0000	-0.0000	-0.0000	-0.0000	-0.1765	-0.0000	-0.0000	0
0.0000	-0.0000	-0.0000	-0.0000	-0.0000	-0.0000	-0.0000	-0.0000	-0.0000	-1.1620	-0.0000	-0.0000
-0.0000	-0.0000	-0.0000	-0.0000	-0.0000	-0.0000	-0.0000	-0.0000	-0.0000	-0.0000	-1.1620	-0.0000
0	-0.0000	-0.0000	-0.0000	-0.0000	-0.0000	-0.0000	-0.0000	0	-0.0000	-0.0000	-0.1765

*Figure 13: relative variations of the real (**upper**) and imaginary (**lower**) parts of the entries of matrix B calculated with n_div=60 integration points with respect to the case with n_div=50*

From 50 to 60 integration points the maximum variations are around 2% in the real part and 1% in the imaginary part. Despite some isolated cases, the majority of the entries changes by less than the percentage. In order to understand the effect of the number of integration points on the accuracy of the integrals, 3 pairs of panels of each matrix with the highest errors in magnitude (rectangles in Figure 13) are selected and both increments and value of the entries are tracked in the following plots (Figure 14):
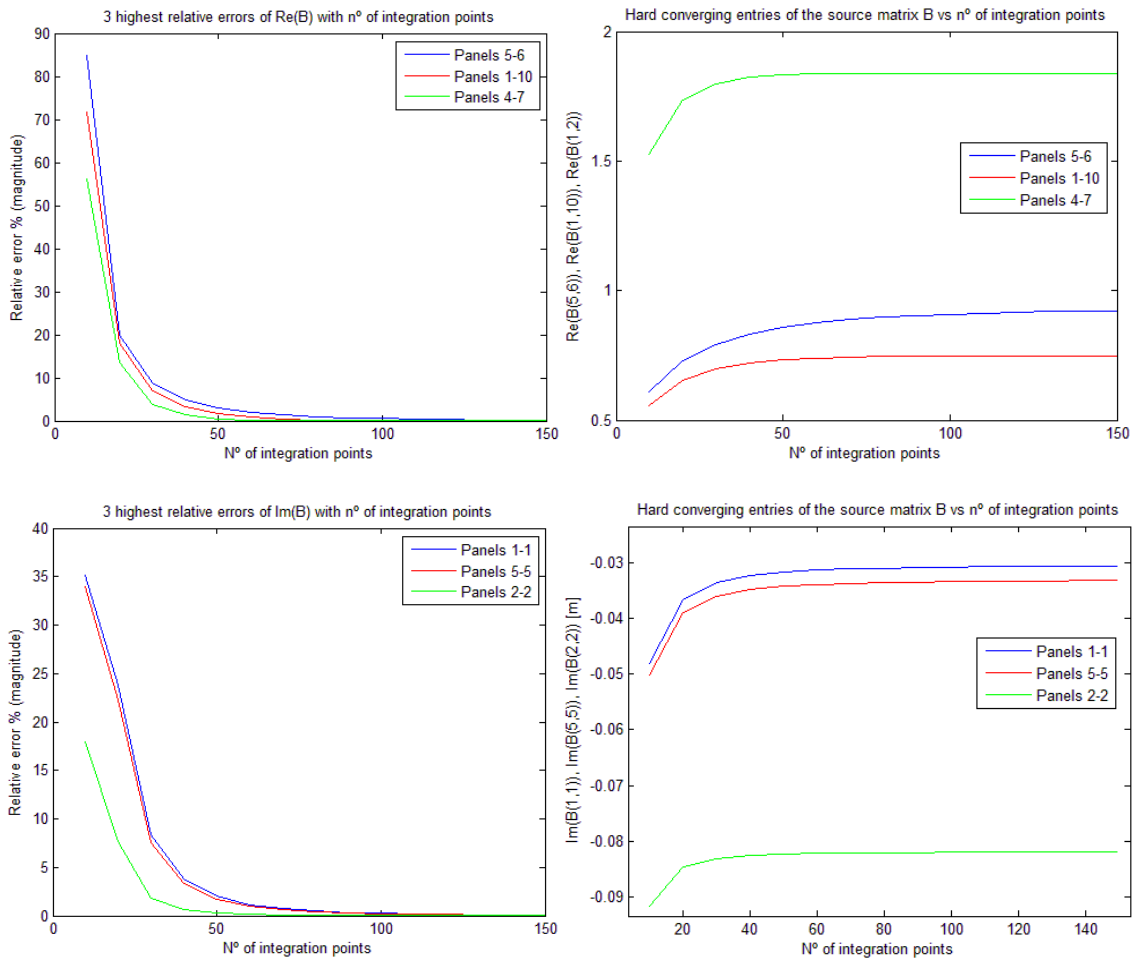
*Figure 14: relative variations and absolute values of the real (**upper**) and imaginary (**lower**) parts of three hard converging entries of matrix B versus the number of integration points*

47
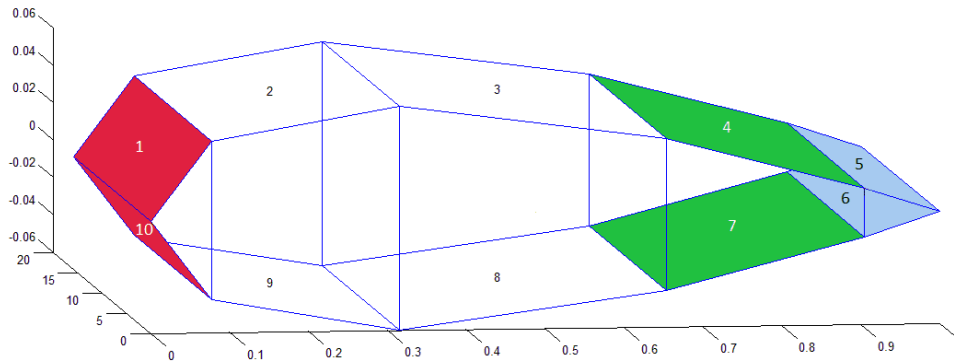
Figure 15: geometrical view of the three pairs of panels from Figure 14, referring to the real part of matrix B

As expected, the increments decay to zero as the number of integration points increases. The pairs of panels with the highest variations of the real part are illustrated in Figure 15 with matching colors. The wing was re-scaled for a better view of the geometry. The variations are bigger when the panels' centers are closer. However, this is not necessarily the case of adjacent panels. Panels 4 and 7 (green) do not share a common boundary but still have the 3rd highest relative variation. Taking the entries with 150 points as fully converged integrals, the true error can be estimated for both real and imaginary parts:

Table 4: relative increments and estimated error in percentage of the three critical entries of both real and imaginary parts of matrix B

Entries of B	Nº of integration points				
	5	60	90	110	150
Re{B(5,6)}	4.0435	0.8758	0.9044	0.9133	0.9218
Estimated true error %	342.7351	-4.9887	-1.8843	-0.9152	0
Re{B(1,10)}	1.9531	0.7402	0.7467	0.7476	0.7480
Estimated true error %	161.1096	-1.0496	-0.1832	-0.0559	0
Re{B(4,7)}	3.4935	1.5093	1.8391	1.8393	1.8393
Estimated true error %	89.9364	-0.1574	-0.0142	-0.0029	0
Im{B(1,1)}	-0.0743	-0.0313	-0.0308	-0.0307	-0.0306
Estimated true error %	142.8105	2.4583	0.8595	0.4195	0
Im{B(5,5)}	-0.0760	-0.0339	-0.0334	-0.0333	-0.0332
Estimated true error %	128.9157	2.0982	0.7307	0.3561	0
Im{B(2,2)}	-0.1118	-0.0822	-0.0820	-0.0820	-0.0819
Estimated true error %	36.5079	0.3427	0.1167	0.0565	0

Comments:

- With only 5 integration points per panel, the error is very high reaching the hundreds of percentage. Although 5 points are unacceptable for these pairs of panels, it is shown next that 5 points can be adequate for sufficiently separated panels
- 60 points provide a maximum of 5% error for the trailing edge panels 5-6 and an acceptable minimum of 0.16% for panels 4-7
- With 90 points all the errors are below 1% except for the panels 5-6 with almost 2%

- Finally, when using 110 points the error in panels 5-6 drops to 0.91% and despite panels 5-5 with 0.33%, the remaining errors are below 0.1%

The results with 110 points provide a maximum error for both real and imaginary parts of B lower than 1%. This considered an acceptable approximation, at least for the academic purpose of this study. However, not all panels require that amount of integration points since it is known that the integrands decay significantly as the distance between panels increases (with 1/R). In order not to waste additional computational resources while obtaining satisfactory approximations of the integrals, the following rule was implemented:

- $n_{div} = 5$, if the panels' centers are separated by more than twice the maximum distance between any two consecutive chordwise panels (X direction)
- $n_{div} = 110$, if the panels' center are separated by less than half of the maximum distance between two directly opposing panels located in the upper and lower side of each ring of panels (Z direction)
- $n_{div} = 60$ otherwise

```
K>> error(1:12,1:12)
```

	1st ring of panels										2nd ring of panels	
	upper side					lower side					upper side	
0.0803	-0.0773	-0.0000	0.6150	0.2021	0.2017	0.6078	-0.0000	-0.0091	-0.0559	-0.0003	-0.0003
-0.0005	0.0130	-0.0001	0.0000	0.5035	0.5005	-0.0000	-0.0000	-0.0047	-0.0001	-0.0003	-0.0003
-0.0000	-0.0000	0.0068	-0.0000	0.0000	0.0000	-0.0000	-0.0039	-0.0000	0.0000	-0.0001	-0.0002
0.5507	0.0000	-0.0001	0.0118	-0.0003	-0.0002	-0.1574	-0.0000	-0.0000	0.5450	0.0000	-0.0000
0.2008	0.5510	-0.0000	-0.0514	0.0690	-0.9152	-0.0400	-0.0000	0.5478	0.2004	0.0001	0.0000
0.2004	0.5478	-0.0000	-0.0400	-0.9152	0.0690	-0.0514	-0.0000	0.5510	0.2008	0.0001	0.0000
0.5450	-0.0000	-0.0000	-0.1574	-0.0002	-0.0003	0.0118	-0.0001	0.0000	0.5507	0.0000	-0.0000
0.0000	-0.0000	-0.0039	0.0000	0.0000	0.0000	-0.0000	0.0068	-0.0000	-0.0000	-0.0001	-0.0002
-0.0001	-0.0047	-0.0000	-0.0000	0.5005	0.5035	0.0000	-0.0001	0.0130	-0.0005	-0.0003	-0.0003
-0.0559	-0.0091	-0.0000	0.6078	0.2017	0.2021	0.6150	-0.0000	-0.0773	0.0803	-0.0003	-0.0003
-0.0003	-0.0003	-0.0001	0.0000	0.0001	0.0001	0.0000	-0.0001	-0.0003	-0.0003	0.0803	-0.0773
-0.0003	-0.0003	-0.0002	-0.0000	0.0000	0.0000	-0.0000	-0.0002	-0.0003	-0.0003	-0.0005	0.0130

```
K>> error(1:12,1:12)
```

	1st ring of panels										2nd ring of panels	
	upper side					lower side					upper side	
0.4195	-0.0000	-0.0000	0.0000	-0.0000	-0.0000	0.0000	-0.0000	0.0000	-0.0000	-0.0000	-0.0000
0.0000	0.0565	0.0000	-0.0000	0.0000	-0.0000	0	0.0000	-0.0000	-0.0000	0.0000	0.0000
-0.0000	0.0000	0.0271	0.0000	-0.0000	-0.0000	0.0000	-0.0000	-0.0000	0.0000	-0.0000	-0.0000
-0.0000	0.0000	-0.0000	0.0507	0.0000	-0.0000	-0.0000	-0.0000	-0.0000	0.0000	0.0000	0.0000
-0.0000	-0.0000	-0.0000	0.0000	0.3561	-0.0000	-0.0000	-0.0000	0.0000	0.0000	-0.0000	-0.0000
0.0000	0.0000	-0.0000	-0.0000	-0.0000	0.3561	0.0000	-0.0000	-0.0000	-0.0000	-0.0000	-0.0000
0.0000	-0.0000	-0.0000	-0.0000	0.0000	0.0000	0.0507	-0.0000	0.0000	-0.0000	-0.0000	0.0000
0.0000	-0.0000	-0.0000	0.0000	-0.0000	-0.0000	0.0000	0.0271	0.0000	-0.0000	-0.0000	0.0000
-0.0000	-0.0000	0.0000	0	-0.0000	0.0000	-0.0000	0.0000	0.0565	0.0000	0.0000	0.0000
-0.0000	0.0000	-0.0000	0.0000	-0.0000	-0.0000	0.0000	-0.0000	-0.0000	0.4195	-0.0000	0.0000
-0.0000	-0.0000	-0.0000	0.0000	0.0000	0.0000	-0.0000	0.0000	0.0000	-0.0000	0.4195	-0.0000
0.0000	0.0000	0.0000	0.0000	0.0000	0.0000	0.0000	-0.0000	0.0000	0.0000	0.0000	0.0565

*Figure 16: estimated error in percentage of the real (**upper**) and imaginary (**lower**) parts of the entries of the source matrix B calculated with the criterion defined*

The matrices in Figure 16 were obtained after the implementation of the defined criterion and represent the estimated true error of each entry. The estimated error is below 1% in the whole matrix, even though some of the integrals were calculated with only 5 integration points. The CPU time concerning the calculation of the full matrix B with different number of integration points is presented below:

Table 5: computation time and maximum absolute estimated error for the calculation of matrix B using different number of integrations points

Nº of integration points	CPU time (s)	Maximum estimated error |%|
5	4.30	342.74
60	43.73	4.99
90	94.37	1.88
110	139.83	0.92
5 or 60 or 110	8.29	0.92

The advantages of using the selective integration points' criterion are evident in the table above. This technique allows a dramatic decrease of the computational cost while keeping the maximum estimated error below 1%. For these reasons, the defined criterion is accepted and considered suitable for further calculations.

5.1.2   The Doublet Integrals Matrix – C

The relative variations from 5 to 10 integration points are the following:

```
>> CR_ERROR(1:12,1:12,1)
                                1st ring of panels                                      2nd ring of panels
                upper side                                 lower side                        upper side
        0  -95.4743  -31.5608   -5.1727   -1.7608   -1.7574   -5.1124  -30.2513  -89.9545  -99.3289      NaN    0.0135
 -82.8911        0  -72.8966  -12.5767   -4.1225   -4.0983  -12.1042  -61.6876  -90.5430  -77.7548   0.0137      NaN
 -22.1143  -60.4269        0  -59.9033  -19.8957  -19.7014  -54.9917  -89.4865  -53.1312  -21.4270   0.0082   0.0115
  -4.4623  -12.3284  -70.8049        0  -80.2694  -79.3303  -97.5217  -66.2925  -11.9390   -4.4183   0.0024   0.0053
  -1.7468   -4.6519  -28.0734  -94.4129        0  -99.9474  -93.7902  -27.8135   -4.6254   -1.7436   0.0004   0.0023
  -1.7436   -4.6254  -27.8135  -93.7902  -99.9474        0  -94.4129  -28.0734   -4.6519   -1.7468   0.0004   0.0023
  -4.4183  -11.9390  -66.2925  -97.5217  -79.3303  -80.2694        0  -70.8049  -12.3284   -4.4623   0.0024   0.0052
 -21.4270  -53.1312  -89.4865  -54.9917  -19.7014  -19.8957  -59.9033        0  -60.4269  -22.1143   0.0080   0.0112
 -77.7548  -90.5430  -61.6876  -12.1042   -4.0983   -4.1225  -12.5767  -72.8966        0  -82.8911   0.0135   0.0141
 -99.3289  -89.9545  -30.2513   -5.1124   -1.7574   -1.7608   -5.1727  -31.5608  -95.4743        0   0.0146   0.0134
      NaN    0.0135    0.0082    0.0025    0.0004    0.0004    0.0025    0.0081    0.0134    0.0146        0  -95.4743
   0.0137      NaN    0.0114    0.0053    0.0022    0.0022    0.0052    0.0111    0.0141    0.0135  -82.8911        0
```

```
>> CI_ERROR(1:12,1:12,1)
                                1st ring of panels                                      2nd ring of panels
  1.0e-09 *         upper side                                 lower side                        upper side
      NaN   -0.0255    0.0002    0.0019    0.0001   -0.0003    0.0006   -0.0036    0.0277   -0.1538      NaN    0.0000
   0.0093      NaN    0.0023   -0.0027   -0.0001    0.0006   -0.0007    0.0057    0.0714   -0.0157   -0.0002      NaN
  -0.0008    0.0036      NaN    0.0010    0.0032   -0.0016    0.0078   -0.0067   -0.0020   -0.0014    0.0000   -0.0001
   0.0029    0.0008    0.0100      NaN   -0.0188   -0.0037   -0.0118    0.0145   -0.0003   -0.0013   -0.0001   -0.0003
   0.0005   -0.0019    0.0005   -0.0455      NaN   -0.6593   -0.0910   -0.0030   -0.0002    0.0001   -0.0000    0.0001
   0.0001   -0.0003   -0.0029   -0.0910   -0.6593      NaN   -0.0455    0.0005   -0.0019    0.0005    0.0001    0.0001
  -0.0013   -0.0003    0.0145   -0.0118   -0.0037   -0.0188      NaN    0.0100    0.0008    0.0029   -0.0001   -0.0001
  -0.0013   -0.0020   -0.0067    0.0078   -0.0016    0.0032    0.0010      NaN    0.0036   -0.0008        0        0
  -0.0157    0.0714    0.0057   -0.0007    0.0005   -0.0000   -0.0027    0.0023      NaN    0.0093   -0.0002    0.0000
  -0.1537    0.0277   -0.0036    0.0006   -0.0003    0.0001    0.0018    0.0002   -0.0255      NaN   -0.0002    0.0000
      NaN    0.0001    0.0002   -0.0001   -0.0001   -0.0001   -0.0000    0.0001   -0.0000   -0.0002      NaN   -0.0260
  -0.0002      NaN   -0.0001   -0.0001    0.0003    0.0002   -0.0001    0.0000    0.0001   -0.0001    0.0155      NaN
```
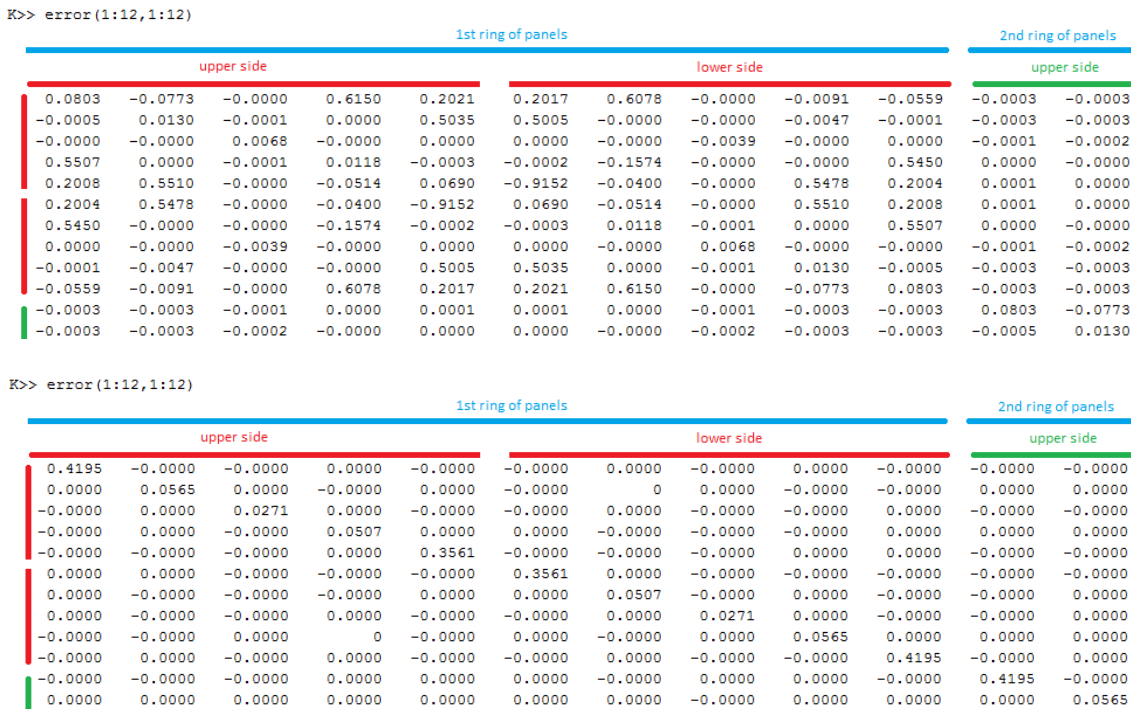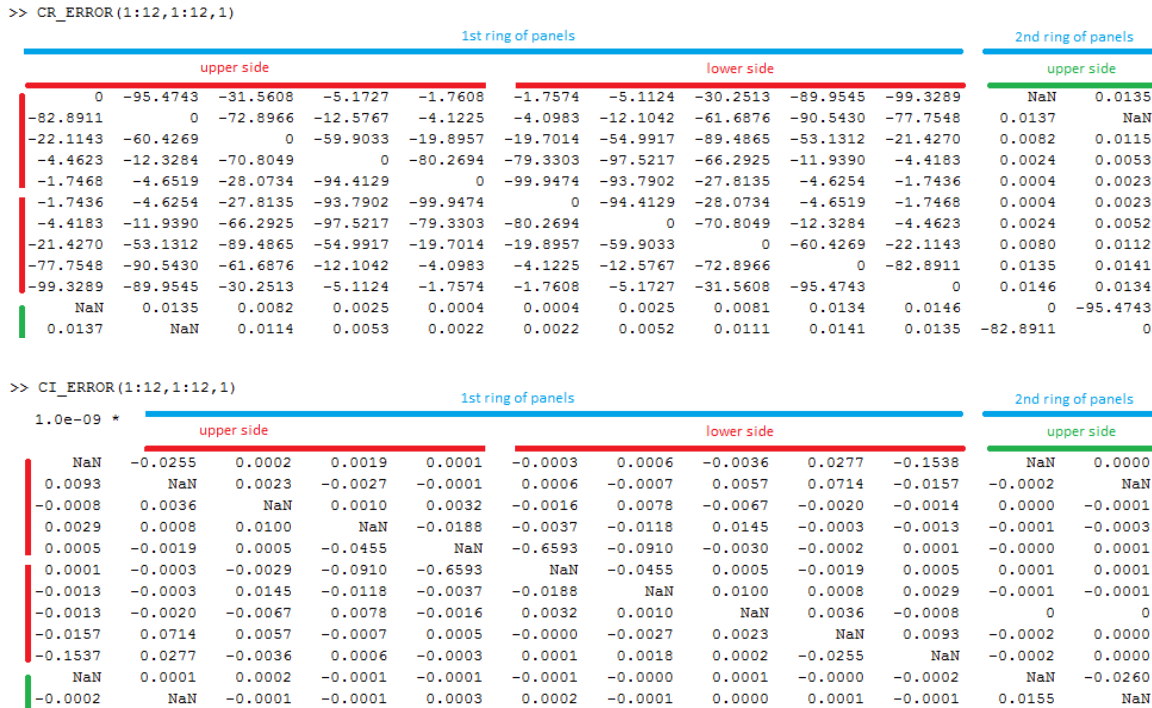
*Figure 17: variations in percentage of the real (**upper**) and imaginary (**lower**) parts of the entries of the doublet matrix C calculated with n_div=10 integration points with respect to the case with n_div=5*

Starting with the real part (Figure 17 - upper), and in comparison with the source matrix B, it is seen that the variations are much higher, ranging from 2% to 99% among the first ring on panels. The zeros in the diagonals refers to exact integrals equal to the real constant -2π (see Appendix B), and the "NaN" symbol refers to integrals that are constant and equal to zero resulting in a 0/0 division. On the other side, the imaginary part experiences residual variations in all the entries. For this reason, the remainder of this study will focus only the real part Re{C}. Figure 18 depicts the relative variations from 50 to 60 integration points (only real part). The three highest variations in magnitude are marked with a rectangle:

```
>> CR ERROR(1:12,1:12,6)
```

			1st ring of panels								2nd ring of panels	
		upper side					lower side				upper side	
0	3.9277	0.0000	-0.0000	-0.0000	-0.0000	0	0.0000	0.8654	13.1592	NaN	-0.0000
0.0833	0	0.0463	0.0000	0.0000	-0.0000	0.0000	0.0038	0.4135	0.0191	-0.0000	NaN
0.0000	0.0024	0	0.0024	0.0000	0.0000	0.0007	0.3851	0.0004	0.0000	-0.0000	-0.0000
-0.0000	0.0000	0.0313	0	0.0522	0.0400	4.6837	0.0121	0.0000	-0.0000	-0.0000	-0.0000
-0.0000	-0.0000	0.0000	3.0896	0	27.5155	2.6075	0.0000	-0.0000	-0.0000	-0.0000	-0.0000
-0.0000	-0.0000	0.0000	2.6075	27.5155	0	3.0896	0.0000	-0.0000	-0.0000	-0.0000	-0.0000
-0.0000	0.0000	0.0121	4.6837	0.0400	0.0522	0	0.0313	0.0000	-0.0000	-0.0000	-0.0000
0.0000	0.0004	0.3851	0.0007	0.0000	0.0000	0.0024	0	0.0024	0.0000	-0.0000	-0.0000
0.0191	0.4135	0.0038	0.0000	-0.0000	0.0000	0.0000	0.0463	0	0.0833	-0.0000	-0.0000
13.1592	0.8654	0.0000	0	-0.0000	-0.0000	-0.0000	0.0000	3.9277	0	-0.0000	-0.0000
NaN	-0.0000	-0.0000	-0.0000	-0.0000	-0.0000	-0.0000	-0.0000	-0.0000	-0.0000	0	3.9277
-0.0000	NaN	-0.0000	-0.0000	-0.0000	-0.0000	-0.0000	-0.0000	-0.0000	-0.0000	0.0833	0

Figure 18: variations in percentage of the entries of the real part of the doublet matrix C calculated with n_div=60 integration points with respect to the case with n_div=50

Although most of the entries have negligible variations (under 0.1%), some entries still vary in the order of the percentage and even in the dozens of percentage. The entries of the 3 highest variations were selected and its actual values are plotted versus the number of integration points in Figure 19:
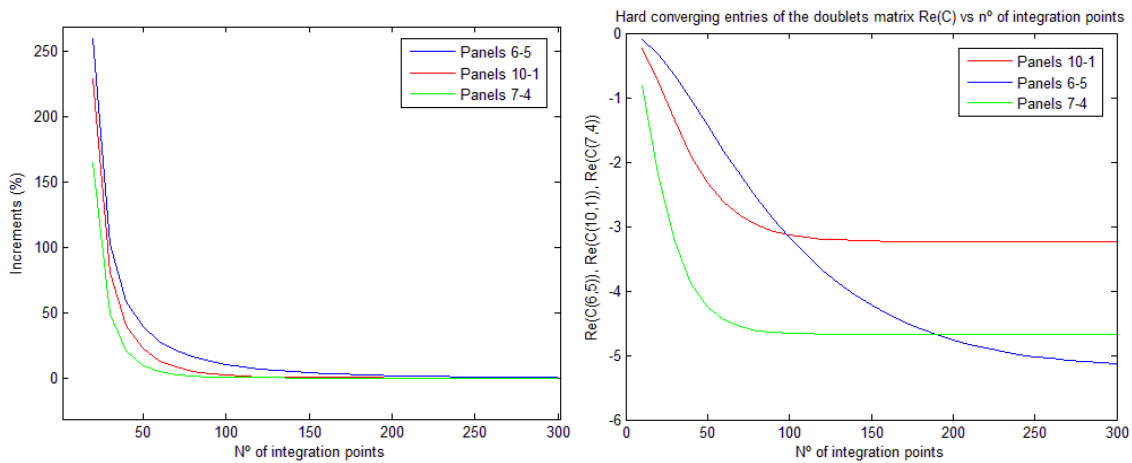

Figure 19: relative variations and absolute values of three entries of matrix C versus the number of integration points

The affected panels are the same as in the B matrix but the convergence rate is much slower in this case. By looking at Figure 19 – right plot, only the trailing edge panels 6 and 5 (blue) have not yet stabilized by 300 integration points. Despite the extremely slow convergence rate, its value at 300 points will be taken as a reference for error estimation. The estimated errors for some selected number of integration points are shown in Table 6:

Table 6: relative increments and estimated error (%) of the three critical entries of the real and part of matrix C

$Re\{C(i,j)\}$	Nº of integration points						
	10	50	90	150	200	280	300
$(6,5)$	-0.08966	-1.434	-2.878	-4.223	-4.763	-5.101	-5.137
Estimated error %	-98.25	-72.09	-43.97	-17.80	-7.30	-0.71	0
$(10,1)$	-0.2296	-2.323	-3.072	-3.226	-3.235	-3.236	-3.236
Estimated error %	-92.91	-28.22	-5.07	-0.33	-0.032	0.00	0
$(4,7)$	-0.8225	-4.255	-4.642	-4.671	-4.671	-4.671	-4.671
Estimated error %	-82.39	-8.90	-0.61	0.00	0.00	0.00	0

Comments:

- Up to 50 points, the error is considered very high, reaching 72% in the trailing edge panels
- The first integral to converge is the pair (4,7) with 90 points
- With 150 points the leading edge panels (10,1) converge with estimated error lower than 1%
- The trailing edge panels require at least 280 integration points for an estimated error lower 1% (error greater than 1% with 270 panels but it is not shown in the table

The same threshold of a maximum estimated error of 1% will be used to formulate a criterion for integration. Similar to the source integrals, the criterion is based on the relative distances between panels on each ring of panels:

- $n_{div} = 10$, if the panels' centers are separated by more than twice the maximum distance between any two consecutive chordwise panels (X direction)
- $n_{div} = 280$, if the panels' center are separated by less than half of the maximum distance between two directly opposing panels located in the upper and lower side of each ring of panels (Z direction)
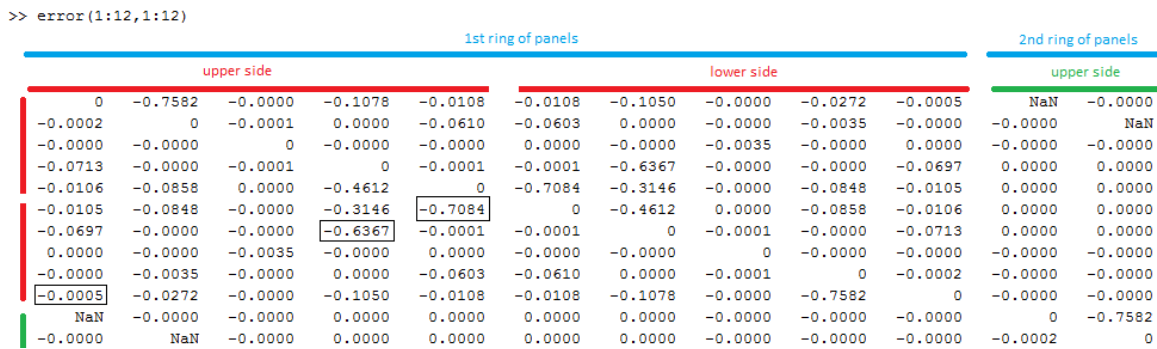- $n_{div} = 90$ otherwise

```
>> error(1:12,1:12)
```

	1st ring of panels									2nd ring of panels	
	upper side				lower side					upper side	
0	-0.7582	-0.0000	-0.1078	-0.0108	-0.0108	-0.1050	-0.0000	-0.0272	-0.0005	NaN	-0.0000
-0.0002	0	-0.0001	0.0000	-0.0610	-0.0603	0.0000	-0.0000	-0.0035	-0.0000	-0.0000	NaN
-0.0000	-0.0000	0	-0.0000	-0.0000	0.0000	-0.0000	-0.0035	-0.0000	0.0000	-0.0000	-0.0000
-0.0713	-0.0000	-0.0001	0	-0.0001	-0.0001	-0.6367	-0.0000	-0.0000	-0.0697	0.0000	0.0000
-0.0106	-0.0858	0.0000	-0.4612	0	-0.7084	-0.3146	-0.0000	-0.0848	-0.0105	0.0000	0.0000
-0.0105	-0.0848	-0.0000	-0.3146	-0.7084	0	-0.4612	0.0000	-0.0858	-0.0106	0.0000	0.0000
-0.0697	-0.0000	-0.0000	-0.6367	-0.0001	-0.0001	0	-0.0001	-0.0000	-0.0713	0.0000	0.0000
0.0000	-0.0000	-0.0035	-0.0000	0.0000	-0.0000	-0.0000	0	-0.0000	-0.0000	-0.0000	-0.0000
-0.0000	-0.0035	-0.0000	0.0000	-0.0603	-0.0610	0.0000	-0.0001	0	-0.0002	-0.0000	-0.0000
-0.0005	-0.0272	-0.0000	-0.1050	-0.0108	-0.0108	-0.1078	-0.0000	-0.7582	0	-0.0000	-0.0000
NaN	-0.0000	-0.0000	0.0000	0.0000	0.0000	0.0000	-0.0000	-0.0000	-0.0000	0	-0.7582
-0.0000	NaN	-0.0000	0.0000	0.0000	0.0000	0.0000	-0.0000	-0.0000	-0.0000	-0.0002	0

Figure 20: estimated error in percentage of the entries of the real part of the doublet matrix B calculated with the criterion defined

Figure 20 depicts the estimated error for the first ring of panels after the implementation of the defined criterion. The 3 hard converging panels are marked with a rectangle. All the entries are below 1%. It is important to notice that the three hard converging entries are no longer the highest errors in the matrix. The criterion's selective integration imposes a different number of points depending on distances allowing the error to grow unevenly in the matrix. The CPU time concerning the full C matrix with different number of integration points is presented in Table 7:

Table 7: computation time and maximum absolute estimated error for the calculation of matrix C using different number of integrations points

Nº of integration points	CPU time (s)	Maximum estimated error |%|
10	6.10	98.25
50	89.01	72.09
90	283.92	43.97
150	760.48	17.80
200	N.A.	7.30
280	N.A.	0.71
300	2907.20	0
10 or 90 or 280	47.79	0.76

The chosen criterion greatly reduces the computational cost and provides a maximum estimated error below 1%. Therefore, the criterion is accepted and considered suitable for further calculations.

5.2 THE EFFECT OF THE NUMBER OF PANELS

It is known from the integral formulas of section 4.2.1 that an exact solution requires an infinite amount of panels covering the whole physical domain constituted by the wing surface and the infinite (plain) wake. Since such requirement is impossible to fulfill, a finite number of panels must be used instead. The aim of this section is to determine the number of panels such that the estimated error of the solution is considered small enough in the academic point of view of this thesis.

For a given wing geometry, there are four parameters that independently control the number and size of each panel: "nseg_X", "nseg_Y", "nseg_wake" and "length_wake".

Table 8: aerodynamic mesh parameters for the paneling of the wing and wake

Surface	Wing	Wake
Parameters	"nseg_X"	"nseg_wake"
	"nseg_Y"	"length_wake"

5.2.1 Wake Panels

The influence of the wake is transmitted into the wing panels by means of the Kutta condition (see section 4.2.2). After the wake integrals are calculated for each wing panel, its contribution is summed and added to the influence of both upper and lower trailing edge panels. Concerning the wake calculations, only the doublet matrix C is affected, therefore no further computations are required for this study. The wing and flight conditions are the same as the previous study with both chordwise and spanwise number of panels equal to 5.
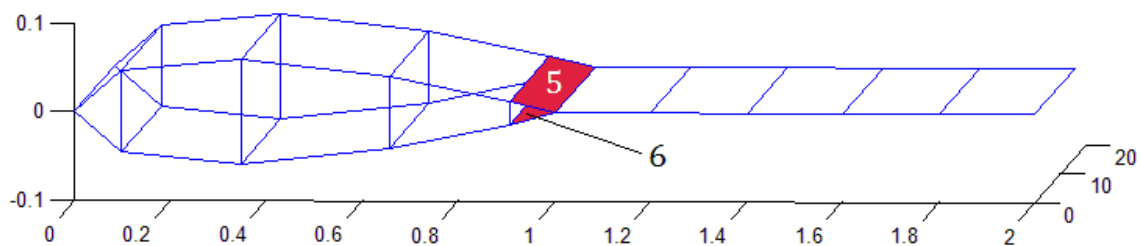
Figure 21: geometrical view of the trailing edge panels for the first ring of panels

Computational procedure:

1. **Panel selection**: the critical panels for this study are those closer to the wake where its influence is the greatest – the trailing edge panels. Since the wing is symmetric, any of these are suitable. The upper panel was chosen (see Figure 21)

2. **Parametric study**: by sweeping both number of wake elements and wake length, the wake influence coefficient is stored in a matrix

3. **Post-computations**: the data in the previous matrix is inspected by making plots of both real and imaginary parts
4. **Convergence criterion**: by analyzing the results, a search for a convergence trend with both wake parameters is performed
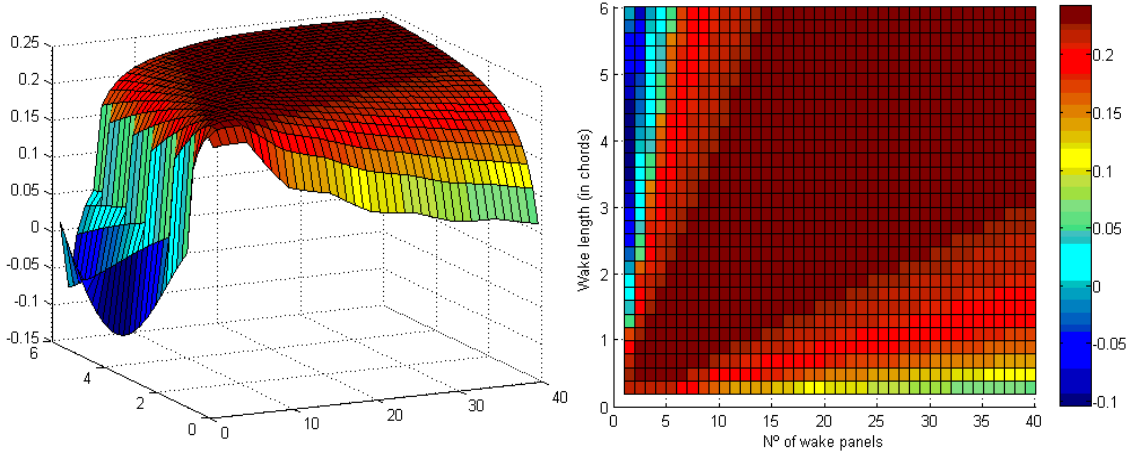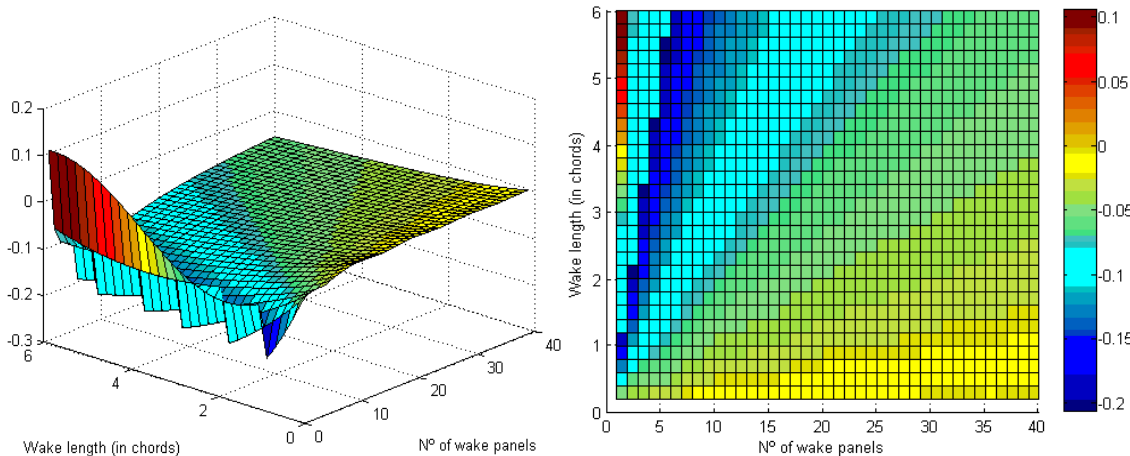5. **Conclusion**: finally, a decision is made concerning the two wake parameters

Figure 22: real part of the wake influence on the upper trailing edge panel (number 5) versus the wake length and number of wake panels

The real part of $C_{wake}(5,5)$[4] is depicted above vs the two wake parameters. For a fixed wake length, the wake influence seems to have a local maximum for a given number of panels. The same behavior occurs the other way around, by fixing the number of wake panels and sweeping the wake length. These two parameters control the density of doublets along the finite plain wake. While the local maximum may be ill-interpreted as a sign of lack of convergence, they only appear as one of the parameters is held constant and are a consequence of the oscillating nature of the integrands. Depending on the doublet density, the integral amplitude varies locally therefore allowing coalescence in a certain region of the parametric domain. Mathematically, the solution should not converge by fixing a parameter but rather by increasing both simultaneously towards the limit of an infinite wake with a continuous distribution of doublets. Consider the following plots in Figure 23:

---
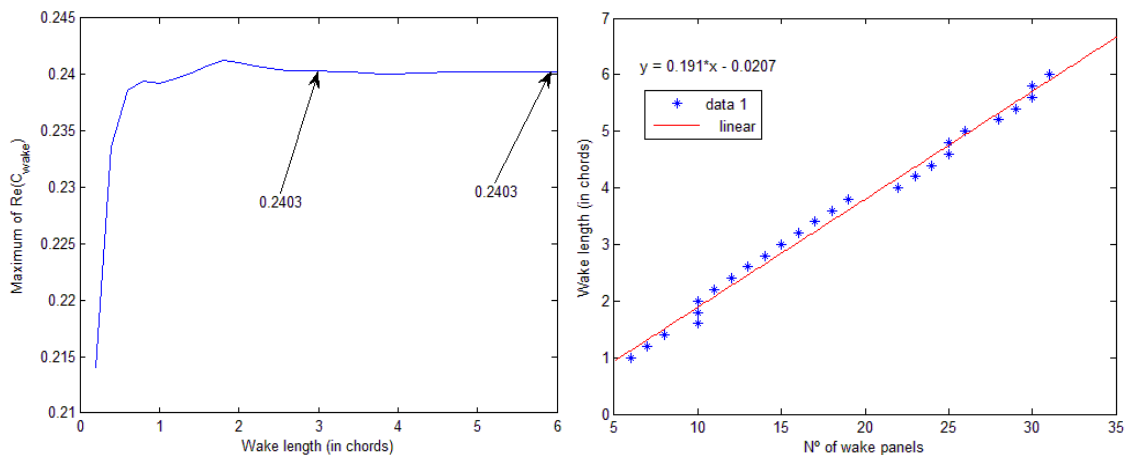
[4] This entry refers to the influence of the whole wake on panel 5, after the Kutta condition has been enforced

The left plot was obtained by calculating the maximum of the real part of $C_{wake}(5,5)$ for each wake length. After 2 chords, the maximum rapidly converges to 0,2403. The right plot features a linear least squares fit of the pairs of wake parameters that lead to the local maximum expressed in the left plot. As expected, convergence occurs by increasing both parameters at the same time. The excellent linear fitting suggests an optimal ratio between the wake length and number of panels that foretells wake convergence for this wing. This ratio corresponds to the slope of the curve and has units of wake length per panel. The inverse relation gives more physical insight and can be stated as the required number of panels per unit of wake length:

$$\text{slope}^{-1} = \frac{1}{0.191} = 5.2356 \left[\frac{\text{panels}}{\text{wake length}} \right] \tag{134}$$

This optimum ratio predicts that if the wake measures 1 chord (1 m), then it should be covered by 5.2356 panels that are approximately the number of panels in the chordwise direction on each side of the wing. In other words, the wake panels should have approximately the same streamwise length (X direction) as those along each side of the wing for wake convergence. This ratio guarantees the correct convergence direction. However, according to Figure 23 – left, convergence only occurs after a certain wake length, typically 3 units of chord. The imaginary part of $C_{wake}(5,5)$ is depicted below:

Figure 24: imaginary part of the wake influence on the upper trailing edge panel (number 5) versus the wake length and number of wake panels

The imaginary part is depicted in Figure 24 and it is harder to analyze because there is no local maximum or minimum for a fixed wake parameter. However, there is clearly a region around the curve $\text{length} = 0.2 * \text{N}$ where the wake influence is nearly constant. Plotting the wake coefficient vs the wake length such that $\frac{\text{length}}{\text{N}} = 0.2$ (Figure 25):
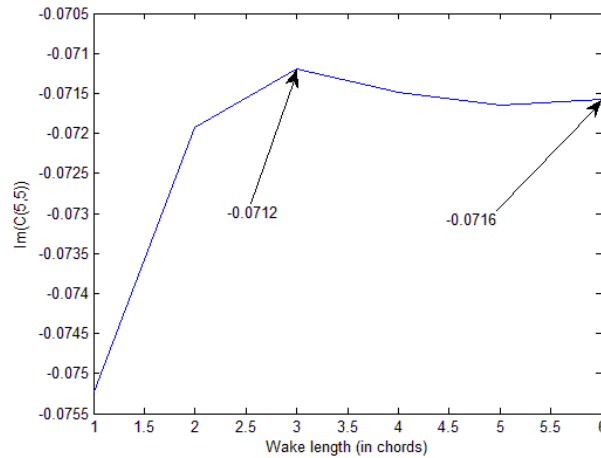
Figure 25: imaginary part of the wake influence on panel 5 versus the wake length.

The values in Figure 25 were extracted from the plot in Figure 24 along the line length = 0.2 * N. This line is roughly the maximum region considered in the plots of Figure 22. After 3 chords of wake length, the wake influence does not varies significantly. Since the real part provided the same minimum wake length for convergence, it is accepted as a length threshold for the wake. In conclusion, the estimated optimal wake should be defined with the following parameters (Table 9):

Table 9: advisable wake discretization parameters for convergence

Wake parameters	Value
"length_wake"	$\geq$ 3 chords
"nseg_wake"	$\cong$ (nseg_X/chord)*length_wake

The optimal number of streamwise wake panels "nseg_wake" are mainly based on the results from Figure 23 and equation (134). In practice, this criterion for convergence suggests a wake panel length equal to average chordwise length of the wing panels, if a uniform mesh were to be used.

5.2.2 Wing Panels

The number of panels along chord and span directions define the quality of the wing's surface mesh and represent the most critical parameters concerning the final solution of the problem. Since the aim of the code is to determine the flutter speed by performing an eigenvalue analysis, this study will focus mainly on a specific eigenvalue and its variation with the number of panels. In order to avoid an unnecessary amount of computation time while covering a wide range of panel's aspect ratio, the wing used in the previous study was shortened to 5 meters of span length. This will naturally increase the wing's stiffness and thus the 1st torsion mode used before corresponds now to an increased natural frequency. The computational parameters are shown in Table 10:

Table 10: computational setup for the convergence study concerning the number of wing panels

Wing Geometry			
Airfoil	NACA 0012		
Aspect Ratio (span)	10	V_∞	20 m/s
Sweep angle	0°		
Chord	1 m	ρ_∞	0.088 kg/m^3
Semi-span	5 m		

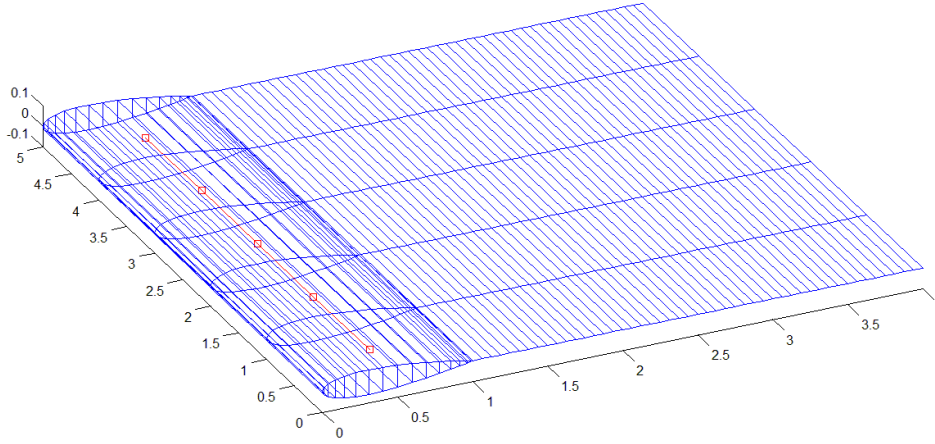| Length wake	3 m		
nseg_X	[4,20]		
nseg_Y	[4,40]	**M**	0.0678
"nseg_wake"	(nseg_X/chord)*length_wake		
Frequency (1st torsion)		100.89 rad/s	

Figure 26: five meter semi-span wing used in the wing mesh convergence study with complete paneling scheme display

5.2.2.1   Computational Procedure

This study has been performed by taking the following steps:

1. For each number of spanwise panels "nseg_Y" both stiffness and mass matrices are calculated using ANSYS, and stored in several txt files. Recall that the parameter "nseg_Y" also represents the number of nodes in the equivalent beam structural mesh

2. Selecting a number of chordwise panels "nseg_X" and spanwise panels "nseg_Y", the aerodynamic matrices are calculated and the structural matrices K and M are read from the files to fulfill the eigenvalue problem equation:

$$s^2[M] + \frac{1}{2}\rho_\infty U_\infty^2 \frac{s}{\omega}[AIC_I] + [K] + \frac{1}{2}\rho_\infty U_\infty^2[AIC_R] = 0 \tag{135}$$

3. The eigenvalue equation is solved iteratively for the dimensional eigenvalue "s" (p-k method)

4. The converged eigenvalue corresponding to the selected mode (1st torsion) is stored

5. Steps 2 to 4 are repeated for the entire range of chordwise and spanwise parameters "nseg_X" and "nseg_Y" respectively

6. Both real and imaginary parts of "s" are plotted vs the number of panels

7. The results are further analyzed performing several cuts to the previous plots and a decision is made concerning the best number of panels for convergence

5.2.2.2   Parametric Study

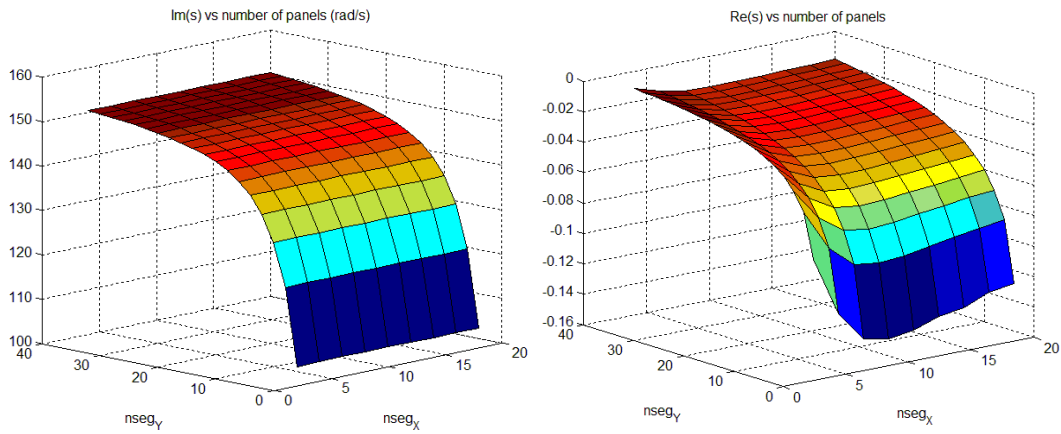The plots in Figure 27 are a result of a parametric study of Re{s} and Im{s} versus the number of panels:

*Figure 27: tridimensional plot of the imaginary (**left**) and real (**right**) parts of the eigenvalue "s" versus the mesh parameters "nseg_X" and "nseg_Y"*

While both plot show signs of convergence, the imaginary part distribution (frequency) seems smoother and faster to converge. This can be seen in the top right corner of the left plot where a large portion of the surface plot is dark red, indicating a nearly constant value for the frequency. In the right plot (damping), such behavior is less obvious. Consider the two pairs of plots in Figure 28 depicting several cuts of the surface plots in Figure 27 by making one of the two mesh parameters constant:
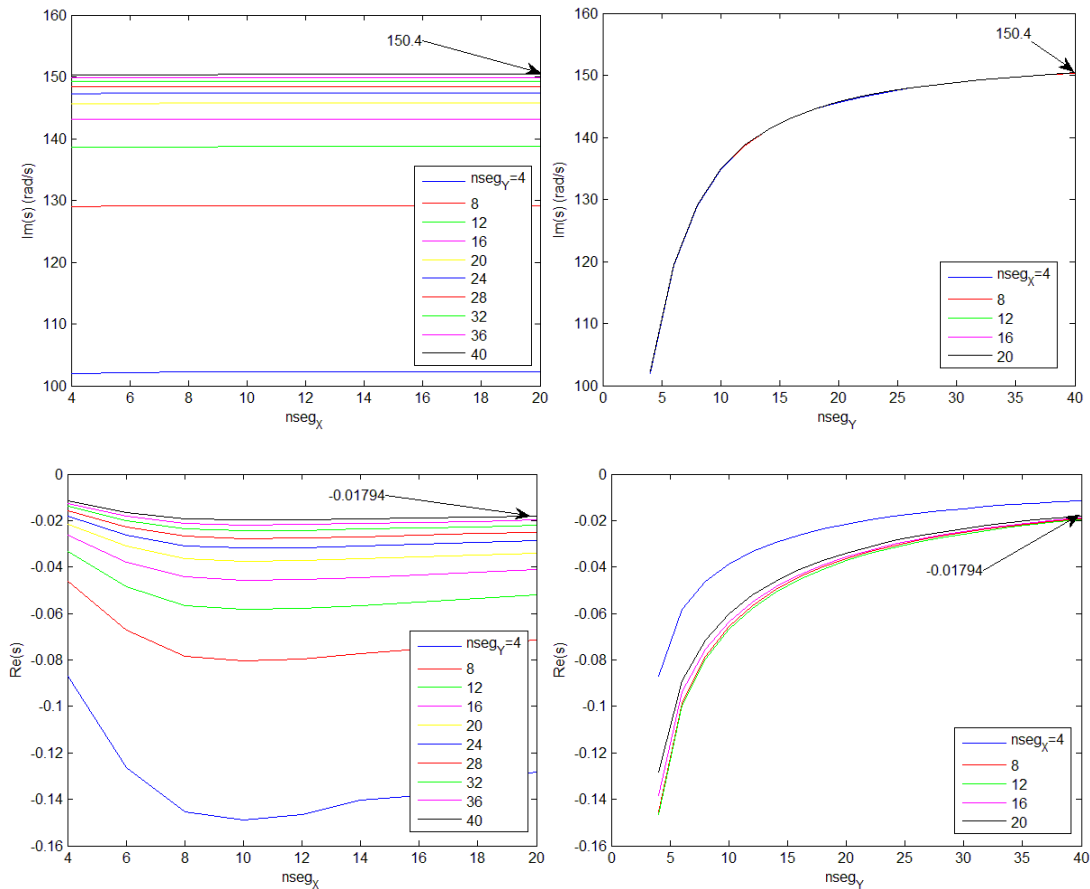
*Figure 28: different sectional views of the plots in Figure 27. **Top left** – imaginary part of "s" (frequency) versus "nseg_X" for several constant "nseg_Y". **Top right** – imaginary part of "s" versus "nseg_Y" for several constant "nseg_X". **Bottom left** – real part of "s" (damping) versus "nseg_X" for several constant "nseg_Y". **Bottom right** – real part of "s" versus "nseg_Y" for several constant "nseg_X"*

Comments (Figure 28):

- The top left plot represents the imaginary part of "s" (frequency) versus the number of panels for different number of spanwise panels "nseg_Y". According to this plot there is little effect on the frequency as the number of chordwise panels "nseg_X" increases
- The top right plot depicts the frequency versus the number of spanwise panels for different number of chordwise panels "nseg_X". As the top left plot suggested, all lines are stacked together indicating a high level of independence with respect to the number of chordwise panels. The convergence is smooth and slow as the number of spanwise panels "nseg_Y" increases
- The two bottom plots concern the real part of "s" (damping). For a constant "nseg_X", the effect of increasing the number of spanwise panels is to decrease the damping (magnitude). The opposite is also true, for a given "nseg_Y", increasing the chordwise number of panels leads to a decrease of the damping in magnitude. In this case, such behavior is less evident and it is only present for "nseg_X" above 10
- Above 8 chordwise panels, adding more panels in this direction has little effect on the damping. This can be seen in the bottom right plot where the several curves are packed together for a large range of spanwise panels. Such behavior is more evident for high "nseg_Y", typically above 20
- In general, both real and imaginary parts seem to be more sensitive to the number of spanwise panels "nseg_Y" than the number of chordwise panels "nseg_X"

In order to evaluate the convergence rate, the relative variations of the real and imaginary parts for 20 chordwise panels along the full range of spanwise panels were calculated and are shown in the plots below (Figure 29):
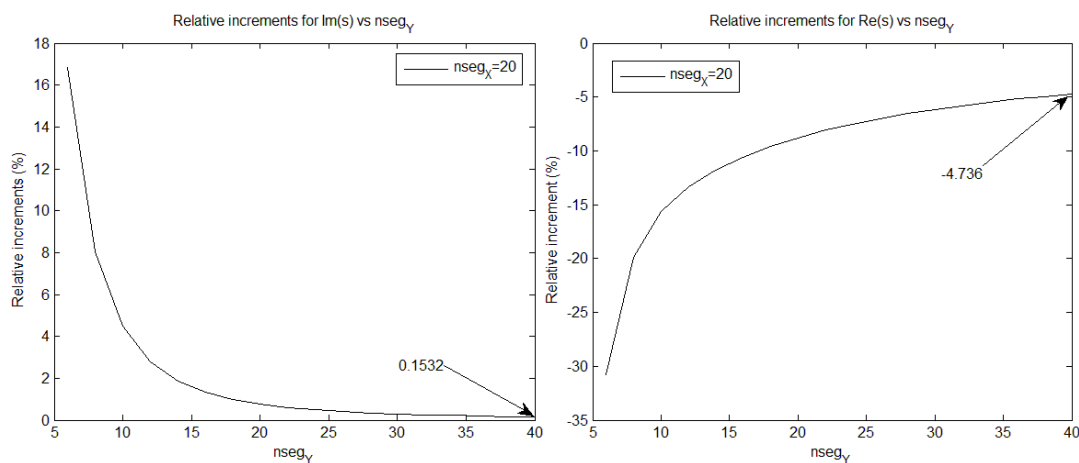

*Figure 29: relative variations in percentage of the imaginary (**left**) and real (**right**) parts of eigenvalue "s" versus the spanwise number of panels "nseg_Y" for the maximum number of chordwise panels "nseg_X"*

Comparing the two plots in Figure 29, it is clear that the real part converges much slower than the imaginary part. From 38 to 40 spanwise panels the damping varies by almost 5% while for the frequency this variation is well below 1%. As seen in the damping plot, the convergence rate is very low and tends to decrease with increasing number of spanwise panels. In the absence of any numerical instability

phenomena, the plot suggests that a variation lower than 1% would require a huge amount of panels along the span (probably more than 100). Considering the computational resources at hand and the academic purpose of this thesis, the convergence study will be limited to the presented range of mesh parameters and its conclusions will be referred to these only.

5.2.2.3   Conclusions and Criteria for Convergence

In this subsection, the complex eigenvalue "s" has been calculated for several combinations of chordwise ("nseg_X") and spanwise ("nseg_Y") panels. The imaginary part represents a frequency and the real part a measure of the aerodynamic damping. After plotting both these quantities versus the number of panels, it became clear that the number of spanwise panels are more important than the number of chordwise panels in terms of convergence. The frequency is nearly independent of the number of panels along the chord for a constant number of spanwise panels but varies significantly the other way around, i.e., by fixing the number of chordwise panels. The damping is substantially more sensible to both mesh parameters than the frequency. The variations are small along the number of chordwise panels for a fixed number of spanwise panels, especially for "nseg_X" > 8 and "nseg_Y" > 20. On the other hand, by fixing the number of panels along the chord, the damping slowly decreases in magnitude as the number of spanwise panels increases. Finally, by inspecting the plots of the relative increments of both real and imaginary parts of "s" it follows that the damping is considerably harder to converge and therefore its results are of greater relevance toward the definition of a criteria for convergence.

Clearly, convergence is not yet achieved with 40 spanwise panels. However, since no further calculations have been performed, "nseg_Y"=40 has been accepted as the best candidate for this wing. The number of chordwise panels however, is less important on the accuracy of the solution and a number below 20 may be enough. The following plots in Figure 30 display the damping and its relative increments for 40 spanwise panels versus the number of chordwise panels:
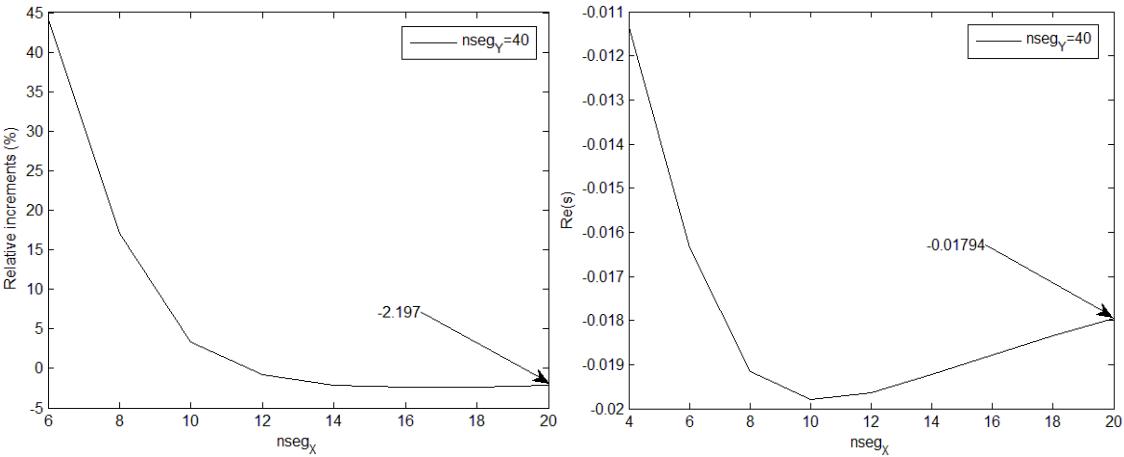

*Figure 30: relative variations in percentage (**left**) and absolute value (**right**) of the real part of the eigenvalue "s" (damping) versus the chordwise number of panels "nseg_X" for the maximum number of spanwise panels "nseg_Y"*

In the left plot of Figure 30, the arrow points to the relative increment of -2.2% from 18 to 20 chordwise panels which is considered high for convergence matters. In addition, the damping plot (Figure 30 –

right) does not shows signs of convergence with a nearly constant slope as the number of panels increases. However, since the magnitudes of these variations are substantially smaller in comparison to those with the number of spanwise panels (see Figure 28), such conclusions may be disregarded. In this view, any of the above numbers of chordwise panels lead to a fair estimation of the damping for the current wing and flight conditions. The decision concerning the number of chordwise panels has been based on the panels' average aspect ratio. These are obtained dividing the mean chordwise panel length by the spanwise panel length. Consider Table 11:

Table 11: panels' mean aspect ratio for several numbers of chordwise panels "nseg_X" for the maximum number of spanwise segments "nseg_Y"

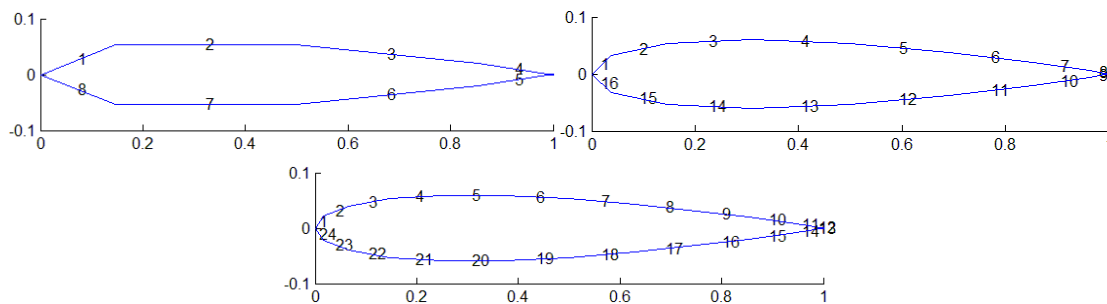| "nseg_X"	Re(s)	Mean Panel aspect ratio	Chord	
4	-0.0114	0.50	1 m	
6	-0.0164	0.75		
8	-0.0192	1.00		
10	-0.0198	1.25		
12	-0.0196	1.50	Half-span	"nseg_Y"
14	-0.0192	1.75	5 m	40
16	-0.0188	2.00		
18	-0.0183	2.25		
20	-0.0179	2.50		

*Figure 31: airfoil discretization with different number of chordwise panels "nseg_X". **Top left** – 4 panels, **top right** – 8 panels and **bottom** – 12 panels*

Mathematically speaking, since the integrals are performed using the same number of points in both directions, the best case would correspond to a square panel with aspect ratio equal to one. However, unless the number of spanwise panels is increased, the airfoil would be discretized with only 8 segments per side which may not be enough for stressing the differences between results of similar airfoils (see Figure 31 – top right. On the other hand, a high number of chordwise segments would lead to very thin panels plus unnecessary increases in the computation time. Choosing 12 chordwise segments leads to an average aspect ratio of 1,50 which is considered a good compromise for the purpose of this work. Finally, a rule that best suits convergence can be defined concerning both mesh parameters (Table 12):

Table 12: advisable wing discretization parameters for convergence

Convergence rule	
Panel Aspect Ratio (PAR)	1.50
"nseg_X"	12
"nseg_Y"	Span/(chord/nseg_X*PAR)

This rule has been applied henceforward for the remaining geometries of interest throughout this thesis.

5.3 REMARK

As a final remark, it should be noted that the convergence criteria established in this chapter do not guarantee convergence, and are optimistic at best. Complete convergence studies would require an extension of the current study for other flight conditions, wing geometries and possibly other frequencies. In addition, extra CPU time would be needed to extend the calculations for finer meshes. Considering the preliminary character of the developed aeroelastic code and its inherent academic purpose, the current convergence study may prove appropriate.

6 EFFICIENT AIC MATRIX CALCULATION

The AIC matrix is the ultimate goal of the aerodynamic calculations and must be calculated several times in the iterative process of determining the wing flutter speed. However, the process of obtaining this matrix is lengthy and its computation time can range from minutes to hours depending on the quality of the mesh used. One basic technique for estimating this matrix without recalculating the full aerodynamics is by interpolation. Such method has been implemented successfully in the aeroelastic commercial codes of NASTRAN® and ZAERO®. The aim of this chapter is to perform a parametric study of the AIC matrix and then to develop a methodology for estimating the entries of this matrix using proper interpolation rules.

6.1 PARAMETRIC STUDY OF THE AIC MATRIX

For a given geometry and mesh, there are two parameters that define the AIC matrix: the reduced frequency "k" and the Mach number "M". If the entries of the matrix (coefficients) vary smoothly over these two parameters, it is possible to approximate them locally by simple interpolation functions such as low order polynomials. It is shown here that this is indeed the case. The setup for this study is the following:

1. **Geometry selection**: in order to evaluate the effect of the geometry on AIC matrix, two wings of different aspect ratios have been used
2. **Mesh selection**: since this study is rather qualitative than quantitative, there is no need of using a high quality mesh. The purpose of this study is to evaluate the smoothness (curve shape) of the aerodynamic coefficients with both frequency and Mach number and not its numerical values
3. **AIC calculation**: for each geometry, the AIC matrix is calculated for a wide range of k and M parameters and is stored in matrix arrays
4. **Plot drawing**: for each wing and for each Mach number, several coefficients are selected and its values are plotted versus the reduced frequency "k". After inspecting these plots, the ones who depict the different curve behaviors are selected for analysis
5. **Parametric analysis (reduced frequency)**: the selected plots are analyzed and compared
6. **Parametric study (Mach number)**: Steps 4 and 5 are repeated for constant "k"
7. **Conclusion** and main remarks of the parametric analysis

The computational parameters for parametric study are shown in Table 13:

Table 13: geometrical, computational and aerodynamic parameters used in the parametric study of the AIC matrix

	Chord (m)	Span (m)	Aspect Ratio	Airfoil
Wing 1	1	16	16	NACA 0012
Wing 2	1	5	5	NACA 0012
Aerodynamic Mesh				
"nseg_X"	5			
"nseg_Y"	5			
"nseg_wake"	15			
"wake_length" (m)	3			

Parametric Study		
	Constant Mach	**Constant frequency**
	[0.1; 10.1]	(1, 3, 5, 7)
Reduced Frequency "k"	**Natural frequencies (rad/s)**	
	1st spanwise bending	2.243
	2nd spanwise bending	14.064
	1st chordwise bending	31.341
	1st torsion	31.523
Mach number "M"	**Constant frequency**	**Constant Mach**
	[0.034; 0.54]	(0.07, 0.14, 0.27, 0.54)
Altitude (m)	20000	
Air density (kg/m³)	0.0880	
Speed of sound (m/s)	295.1	

6.1.1 Influence of the Reduced Frequency

The plots in Figure 32, Figure 33 and Figure 34 depict the behavior of some aerodynamic coefficients versus the reduced frequency for several Mach numbers and for the two wings. The plots are stacked in groups of four, each group associated with one particular coefficient. The plots on the left side refer to the high aspect ratio wing (AR=16) and the plots on the right side refer to the low aspect ratio wing (AR=5). The real and imaginary parts are located on the top and bottom plots respectively. Each coefficient has been normalized with respect to the absolute maximum of its distribution over the reduced frequency "k", therefore the values shown are non-dimensional. The horizontal bars in each plot are the reduced frequency bands for each Mach number ranging from the first to the fourth wing's natural frequency. Even though only a few entries of the AIC matrix are considered, their progress along "k" and "M" is representative of the global trend of the full matrix with these parameters.
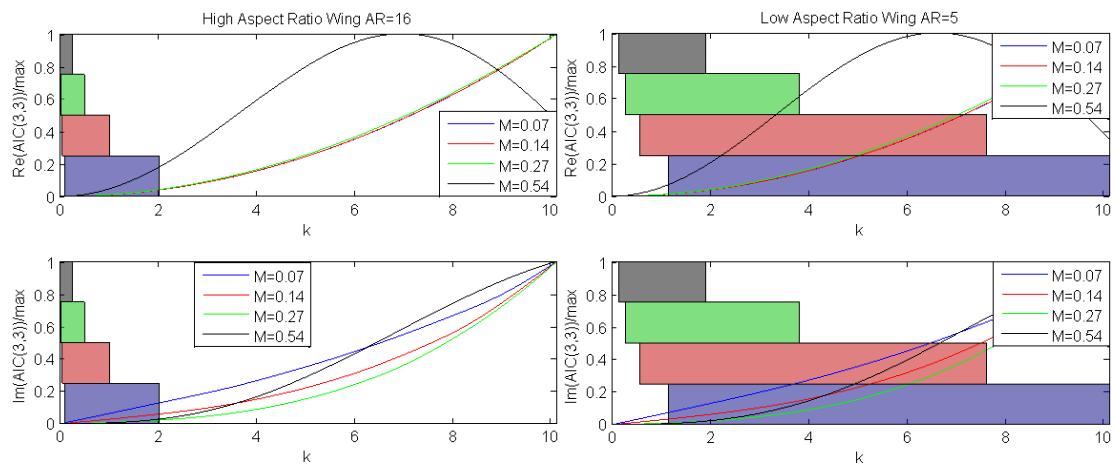

Figure 32: vertical displacement coefficient (UZ) for the vertical force (FZ) of the first structural node AIC(3,3) versus the reduced frequency for several Mach numbers

The first group of plots (Figure 32) corresponds vertical displacement (UZ) coefficient for the vertical force (FZ) of the first structural node AIC(3,3). Starting with the longest wing (left side), it is evident that there is a slow and monotone variation of the coefficient with the reduced frequency for both real and imaginary parts and for every speed. Only the real part at the highest speed (black line M=0.54) seems to behave differently by changing the sign of the slope around k=7. The high aspect ratio wing has its natural frequencies bands closely spaced located on the far left part of the plot, in a zone where the distributions are well behaved. The shortest wing (right side) provides very similar plots in comparison

to the longest wing for both k and M parameters. The major difference resides in the natural frequency bands which are dramatically wider in this case. The curves are still well behaved at each respective natural frequency band location, at least for the last three speeds. For the first speed (M=0.07) the natural frequency band extends beyond the limits of the plot and the behavior of the respective distribution (blue) becomes unclear.
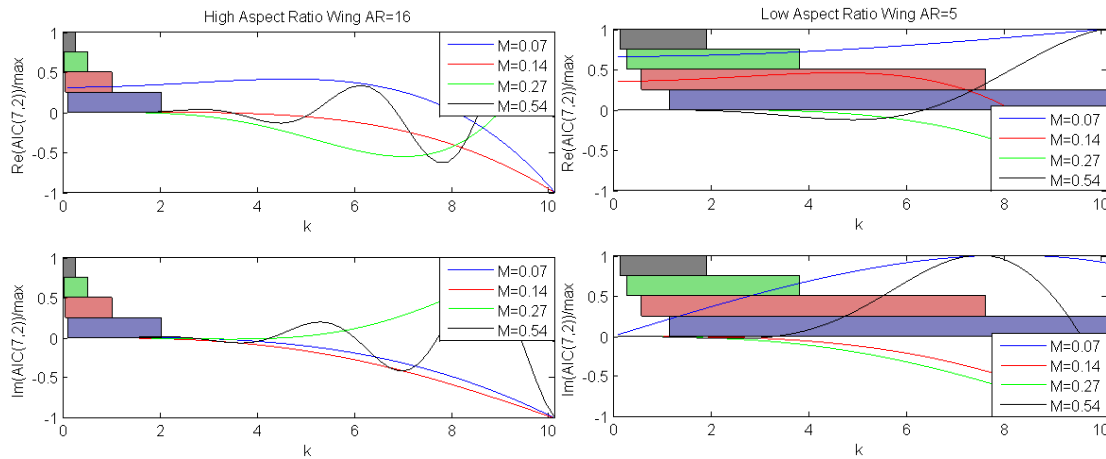

Figure 33: lateral displacement coefficient (UY) for the streamwise force (FX) of the second structural node AIC(7,2) versus the reduced frequency for several Mach numbers

The second set of plots (Figure 33) corresponds to the lateral displacement coefficient (UY) for the chordwise force (FX) of the second structural node AIC(7,2). In the high aspect ratio wing, both real and imaginary parts behave smililarly, with slow and monotone curves up to k=7 for the first three speeds. The black curve (M=0.54) also behaves as such but only up to k=3; for k>3 oscillations are observed for this speed. Nevertheless, all the curves are monotone and vary slowly in their respective bands of natural frequencies. The shorter wing provides slower varying curves for both real and imaginary parts, but not all the curves are monotone over their respective frequency bands. The imaginary part of the lower speed plot has a maximum around k=8, well inside the horizontal blue bar representative of this speed's natural frequency band.
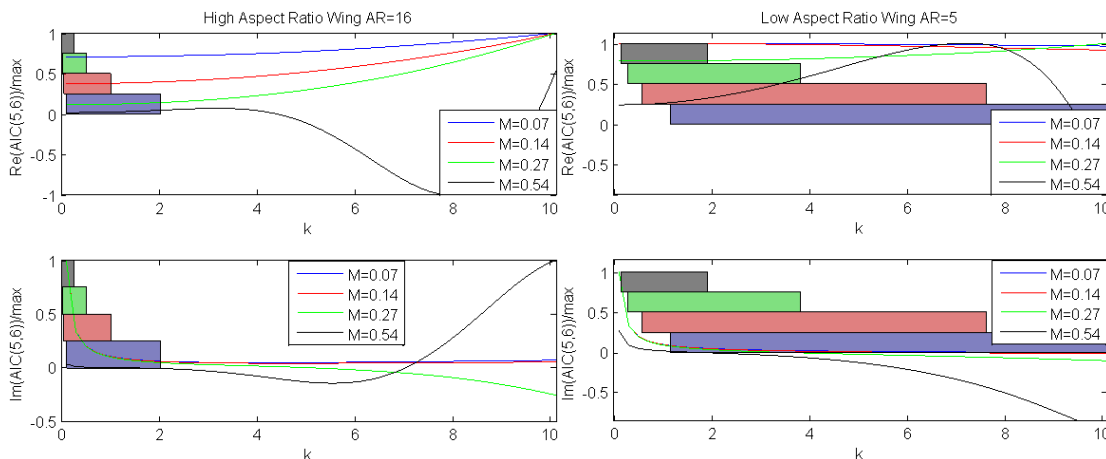

Figure 34: yaw rotation coefficient (ROTZ) for the pitching moment (MY) of the first structural node AIC(5,6) versus the reduced frequency for several Mach numbers

Finally, the yaw rotation coefficient (ROTZ) for the pitching moment (MY) of the first structural node is shown in Figure 34. Observing the real part (top plots), the variations are greater in the high aspect ratio wing but, excluding the highest speed (M=0.54), both wings provide a slow and monotone curves. The imaginary part (bottom plots) shows in general slow and monotone behavior for the first three speeds and for a wide range of reduced frequencies except on the critical set of lower frequencies that goes up to k=2. In this region and for both wings, the imaginary part decays quickly from higher values at k=0.1 to steady values at k=2. Such behavior seems to be independent of the Mach number, at least up to M=0,27. Surprisingly, the curve for M=0.54 is slow varying and monotone here. Unlike the previous analyzed coefficients, the high aspect ratio wing shows stronger sensibility at lower speeds within its natural frequencies band. This is most critical for the lower speed (M=0.07) where the natural frequency band covers the entire sensible region from k=0.1 to k=2 (blue bar).

6.1.2   Influence of the Mach Number

In order to clarify the influence of the Mach number, the aerodynamic coefficients were calculated for several speeds and plotted in separate curves of constant reduced frequency. The chosen coefficients are the same as in the previous section and are plotted in Figure 35, Figure 36 and Figure 37:
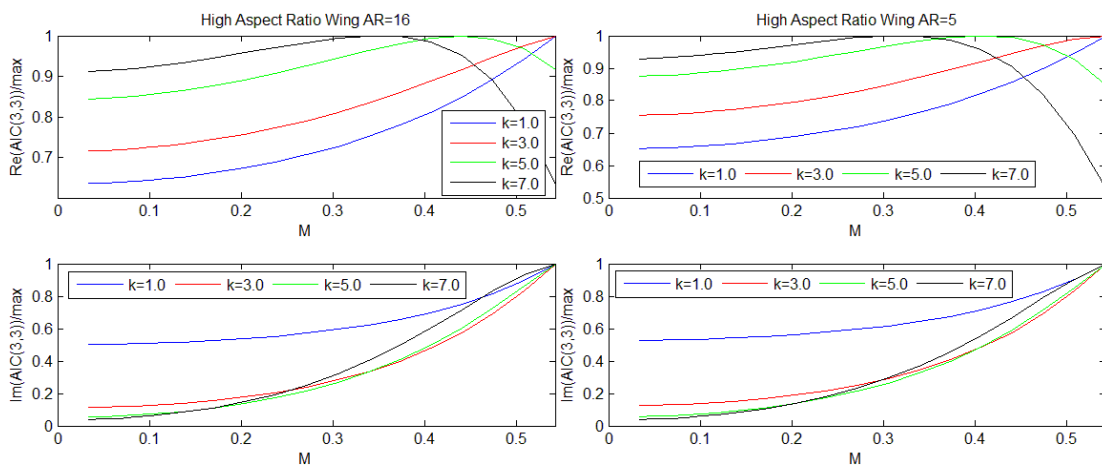

Figure 35: vertical displacement coefficient (UZ) for the vertical force (FZ) of the first structural node AIC(3,3) versus the Mach number for several reduced frequencies.
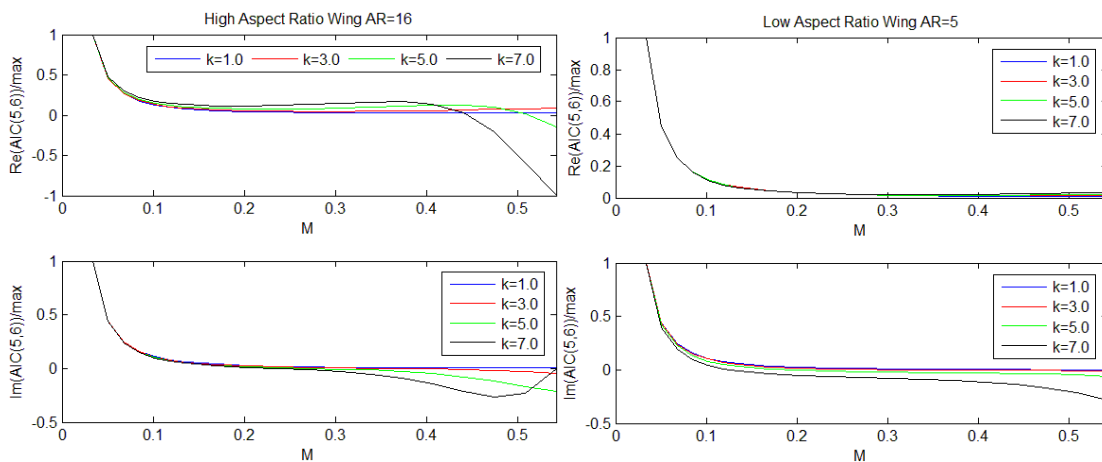

Figure 36: yaw rotation coefficient (ROTZ) for the pitching moment (MY) of the first structural node AIC(5,6) versus the Mach number for several reduced frequencies
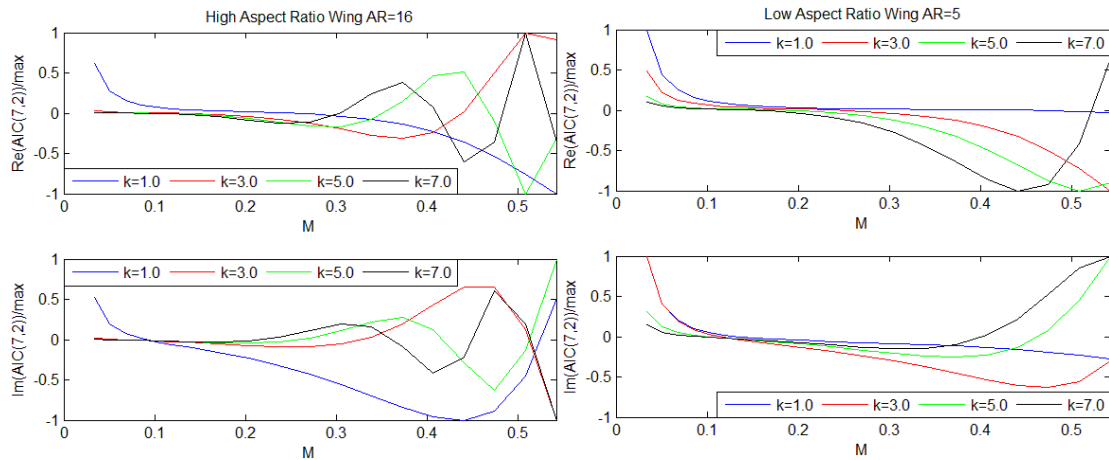
Figure 37: lateral displacement coefficient (UY) for the streamwise force (FX) of the second structural node AIC(7,2) versus the Mach number for several reduced frequencies

Comments:

- The variations are continuous and slow in virtually in all plots except AIC(7,2) for the high aspect ratio wing. In this case, oscillations begin at M=0.3 and k=5

- The curves are similar in shape for both wings in the real and imaginary parts. Again, this is not the case for the AIC(7,2) for all frequencies

- Most of the curves are not monotone and contain relative maxima/minima in the high speed region. This is not necessarily an issue since in general the slopes are of low magnitude

- The AIC(5,6) plots exhibit an abrupt decay for all frequencies and for both wings in the low speed region. This can also be seen in the AIC(7,2) plots although at a smaller scale

6.1.3   Final Remarks Concerning the Parametric Study

The parametric study of the AIC matrix led to some favorable conclusions about the feasibility of using interpolation techniques. First of all, the shape of the obtained curves did not change significantly between wings of very different aspect ratio. This is especially true for the combination of low frequencies and low Mach numbers. Outside these boundaries, it appears that the longer wing coefficients become more sensible with the frequency and Mach than in the shorter wing case. Second, every obtained curve along "k" or "M" is in general well behaved by having relatively low slopes, with few or none local extremes and without any source of singularity/discontinuity. Mathematically, such curves can be treated as continuously differentiable functions and therefore are suitable for being interpolated, at least in a local sense. Third, for each Mach number, the natural frequency band for the high aspect ratio wing is much narrower than in the low aspect ratio wing case. This proximity allows the construction of high quality low-order interpolation functions over the entire reduced frequency band of interest. On the other hand, the shorter wing provides very wide natural frequency bands and in order to obtain close approximations to the curves along these frequencies, higher order interpolation functions are required. This suggests that interpolation schemes are more suitable for longer and thinner wings than with shorter and thicker ones. Finally, for constant reduced frequency, and irrespective of the wing, interpolation along the Mach number can also be very effective provided that both reduced frequency and Mach number are not too high.

There are exceptions to these well behaved curves, appearing in the plots in Figure 34 from the constant M study, and in the plots in Figure 36 and Figure 37 from the constant k study. In these plots, at the beginning of the curves (either low k, or low M), there is a steep variation of the coefficients and especial attention is required concerning the closeness of the interpolation points and the interpolation functions themselves. These issues are addressed in the next section.

6.2 INTERPOLATION SCHEMES

As the parametric study suggests, there are two different ways of interpolating the AIC matrix:

1. **Frequency interpolation**: for a certain Mach number, the aerodynamic coefficients are estimated locally by a continuous function of the reduced frequency
2. **Velocity interpolation**: for a certain reduced frequency, the aerodynamic coefficients are estimated locally by a continuous function of the Mach number

The interpolations are performed by steps according to the p-k method for determining the flutter speed. The aeroelastic stability analysis starts by solving the flutter equation at a low speed for a given set of reduced frequencies. Since the speed is low, it is expected that the reduced frequencies found by solving the eigenvalue problem are close to the structure's natural frequencies. Accordingly, the first interpolation would be a frequency interpolation over this set of natural frequencies (natural frequency band). Once the interpolation function for every entry of the AIC matrix is known, there is no further need of recalculating the AIC matrix inside the frequency band and in its immediate vicinities. Ideally, this covers the entire iterative frequency matching process for all the reduced frequencies of interest at a certain Mach number. The second interpolation is another frequency interpolation performed at a higher speed. Here, the new frequency band covers the set of converged reduced frequencies found at the previous, lower Mach number. The frequency interpolation is extremely advantageous when the system is being solved for several frequencies that are packed together in a narrow band – a characteristic of a high aspect ratio wing.

After performing some frequency interpolations at different speeds, it becomes possible to resort to the second type of interpolation – the velocity interpolation. This interpolation attempts to find the aerodynamic coefficients for a certain reduced frequency as a function of the Mach number. Although attractive in terms of CPU time saving, the velocity interpolations are considerably dangerous because they rely on the accuracy of several frequency interpolations.
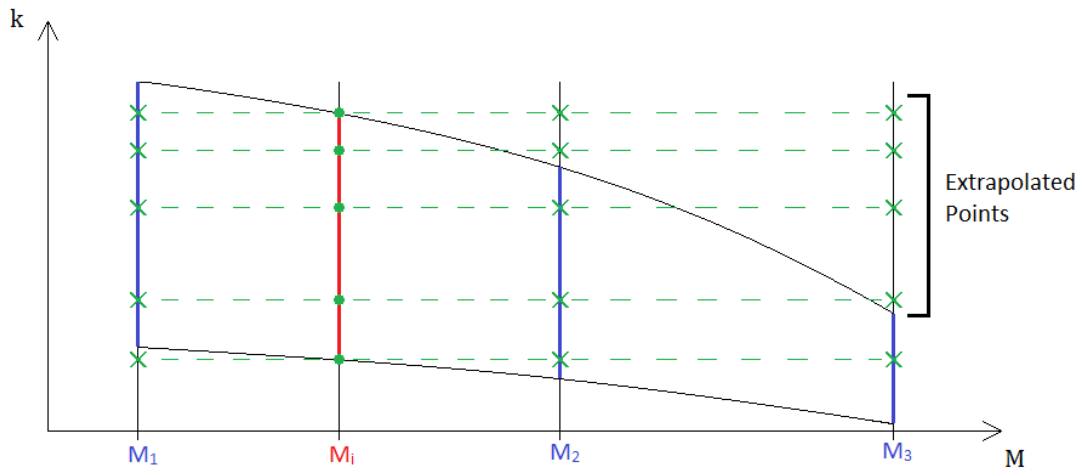
Figure 38: possible evolution for the reduced frequency band (blue and red lines) for different Mach numbers

For a certain intermediate Mach number M_i, it is first required to calculate an estimate of the reduced frequency band (red line Figure 38) containing the frequencies of interest to be converged by the p-k method. Then the velocity interpolation is performed for the reduced frequencies (green dots Figure 38) inside the estimated frequency band using interpolated data (green crosses Figure 38) from other Mach numbers. However, since the reduced frequency band changes with the Mach number, the required data may refer to reduced frequencies not contained in these frequency bands, thus leading to low quality interpolations (extrapolated points Figure 38).

6.2.1   Choice of Interpolation Functions

The interpolation functions are based on the best fitting curve that minimizes the error. The technique adopted here is the least squares fitting using polynomials as approximation curves. Some of the results from the parametric study (section 6.1) have been reviewed for the best curve fitting and the interpolation functions have been chosen after these.

6.2.1.1   Frequency Interpolation

The ideal frequency interpolation requires a function that closely approximates the coefficients for the full reduced frequency band at each speed. At lower speeds these frequencies are similar to the wing's natural frequencies therefore they can be used as a reference for this study. The plots in Figure 39, Figure 40 and Figure 41 correspond to M=0.07 and the blue region depicts the reduced natural frequency band covering the first four natural frequencies at this speed. In these figures, the bar plots refer to the numerical differences (residuals) between the set of AIC points and the points from the obtained curve fit.
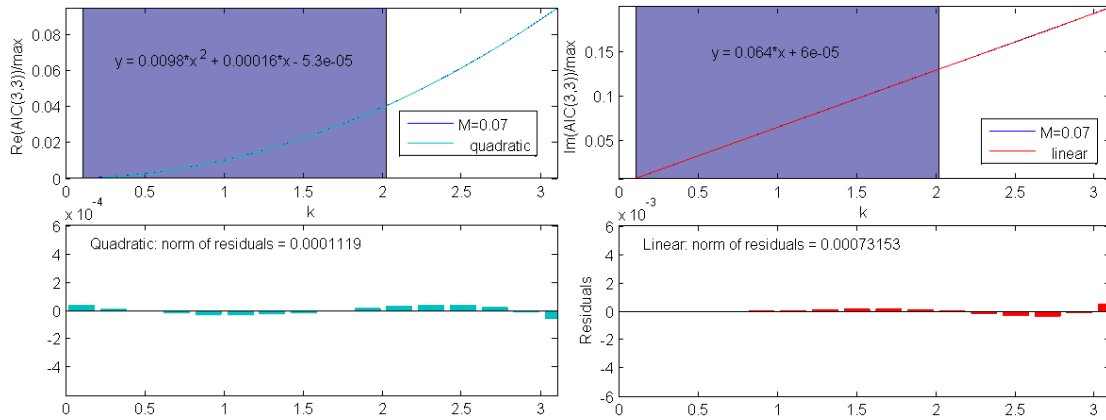
*Figure 39: different curve fittings with residuals for the frequency interpolation of the real (**left**) and imaginary (**right**) parts of AIC(3,3) for a representative Mach number*
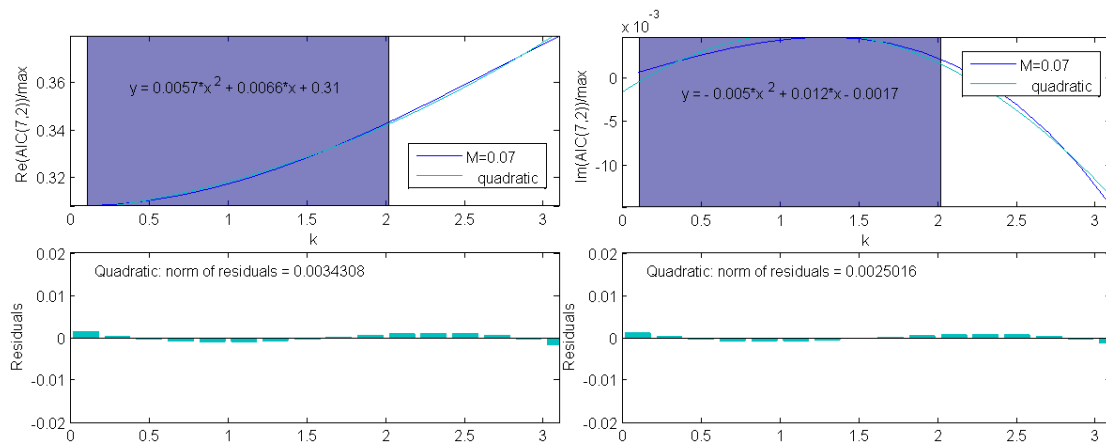

*Figure 40: curve fittings and residuals for the frequency interpolation of the real (**left**) and imaginary (**right**) parts of AIC(7,2) for a representative Mach number*

Observing the curve fittings in Figure 39 and Figure 40 and inspecting the residuals it can be concluded that quadratic interpolations provide excellent approximations to both real and imaginary parts of the coefficients over the entire range of the reduced natural frequencies. It should be noted that these curve shapes are representative of the behavior of most entries of the AIC matrix. The exceptions to these can be seen on AIC(5,6) as detected before on the parametric study (Figure 41):
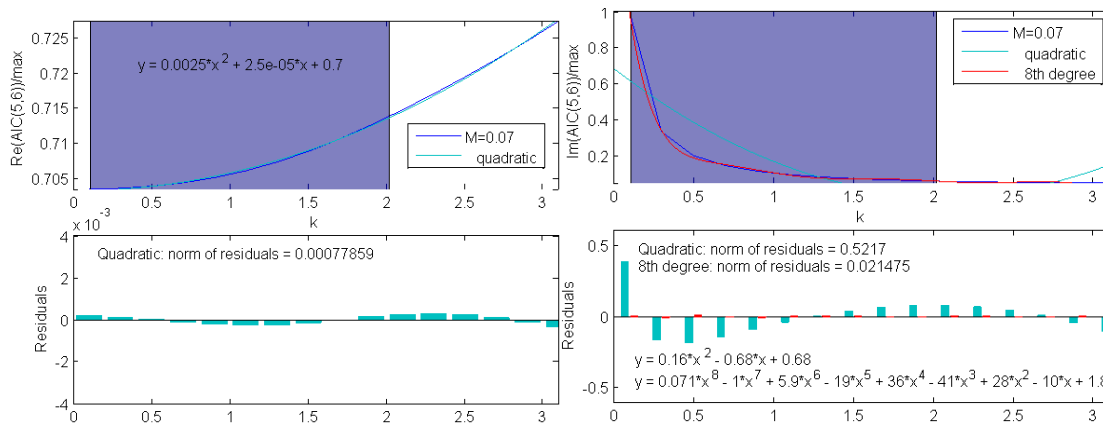

*Figure 41: different curve fittings and residuals for the frequency interpolation of the real (**left**) and imaginary (**right**) parts of AIC(5,6) for a representative Mach number*

While the real part can be accurately approximated by a 2nd degree polynomial, the imaginary part cannot, and requires at least an 8th degree polynomial to do so (Figure 41 – right plot). Since it is not feasible to resort to such high degree polynomials, an alternative technique is sought. One simple way of overcoming this issue is by using two interpolations inside the natural frequency band. However, such would be only justified for some coeficients and there is no way of doing it without recalculating the full aerodynamic matrix. Additional points can be avoided if the two interpolating functions are connected by a common point. For this particular curve shape two linear functions can be used, one for the near vertical part, and the other for the near horizontal segment, connected by the middle point at k≈1 (Figure 42 – left):
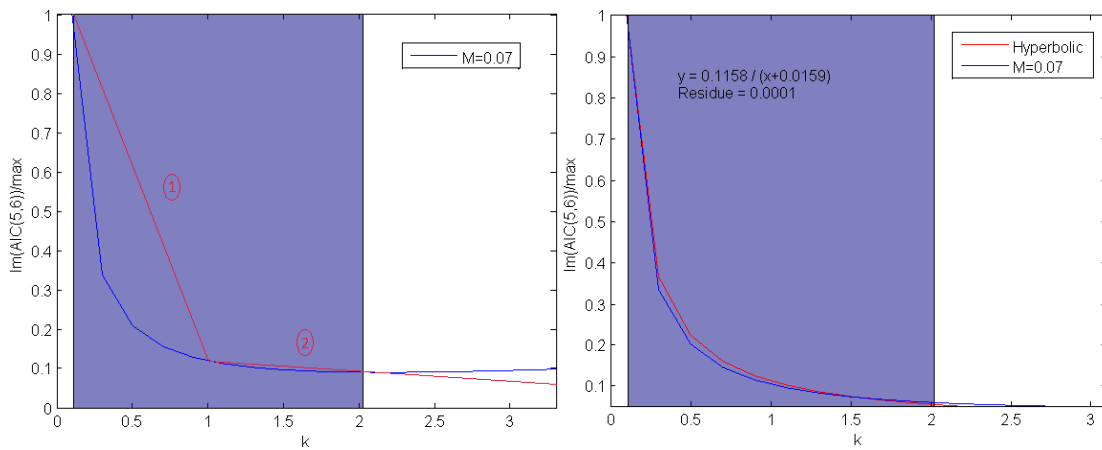

*Figure 42: alternative curve fittings for the imaginary part of AIC(5,6). **Left** side – two-branch linear curve fit with intersection at k=1. **Right** side – rectangular hyperbola curve fit*

This approach tends to favor one half of the curve, depending on the k value where the slope changes significantly (k=0.5 here) and on the length of the frequency band. Another possibility, consists in interpolating this curve with a rectangular hyperbola. In the right plot, a rectangular hyperbola was successfully fit to the curve by solving a non-linear least squares problem using 3 equidistant points.

Concerning the frequency interpolation, two types of functions will be used to estimate the aerodynamic coefficients. In most cases, the variations are slow and a 2nd degree polynomial is considered accurate enough for representing the behavior of the true function AIC(M=cte,k). This can be achieved by simply calculating the coefficients at 3 different reduced frequency values and then the 3 polynomial coefficients are obtained using the general quadratic formula. If otherwise the variations are very steep, a rectangular hyperbola is fit instead. In order to use the same 3 points (k,AIC(k)), a non-linear least squares problem must be solved first.

Table 14: final reduced frequencies and CPU times for an analysis performed with and without the k-interpolation scheme for the high aspect ratio wing

$U_\infty = 10 \, m/s$	No interpolation	k-Interpolation	Relative Error (%)
k_1	0.2243	0.2243	0.00
k_2	1.4982	1.4982	0.00
k_3	3.1368	3.1368	0.00
k_4	3.1649	3.1649	0.00
k_5	4.7533	4.7533	0.00
CPU Time (s)	1043.8531	260.3236	-75.06

"nseg_X"	12
"nseg_Y"	5
Half-span (m)	16

The advantages of the frequency interpolation are evident in Table 14 referring to a single velocity analysis where five frequencies were converged resorting to both standard and k-interpolation methods. The k-interpolation allowed a decrease of 75% in the computational cost while obtaining virtually the same values for the five reduced frequencies.

6.2.1.2 Velocity Interpolation

Interpolation along the Mach number is riskier because it is highly dependent on the frequency interpolation. There are two major issues concerning this type of interpolation:

1. **Local curve behavior**: similar to the frequency interpolation, special attention is required around certain Mach numbers where the variations are higher

2. **Traveling frequency band**: increasing the speed directly influences each aeroelastic mode by changing the value of its frequency. This allows the reduced frequency band to shift sideways for increasing Mach. Also, since the reduced frequency depends on $1/U_\infty$, the frequency band becomes narrower as the Mach number increases (see Figure 38)

The impact of both issues can be minimized by taking small Mach steps between each AIC calculation point. The following plots represent the typical behavior of the aerodynamic coefficients versus the Mach number, for several reduced frequencies:
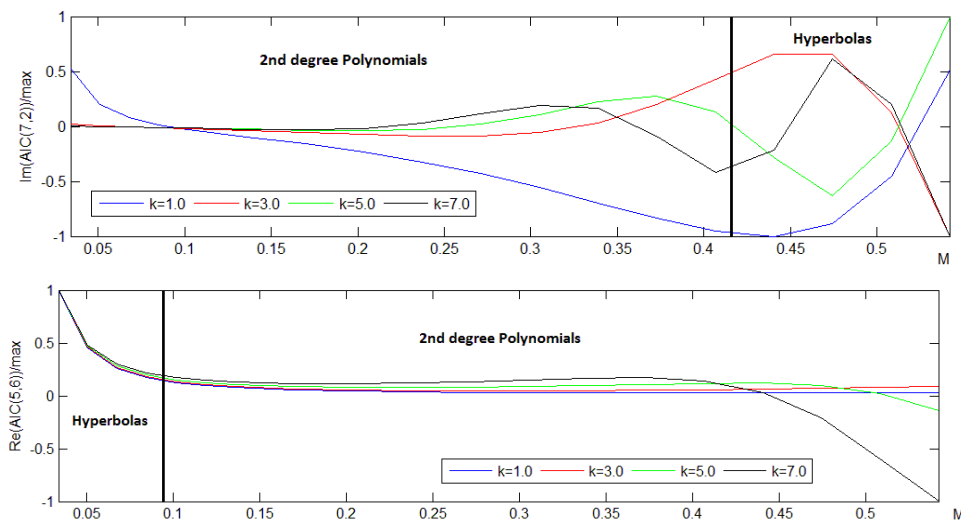

Figure 43: possible velocity interpolation schemes for the different regions of Mach number

For each frequency, the coefficients behave differently depending on each Mach number region. The low and high Mach number regions can lead to slow or abrupt changes in the coeficients, requiring different interpolation functions. On the other hand, in the intermediate region the variations are generaly slow and smooth. It is important to notice that a large range of slow variations does not implies better approximation functions over larger Mach steps. The reduced frequencies can change siginificantly from one speed to another as mentioned in issue number 2 above.
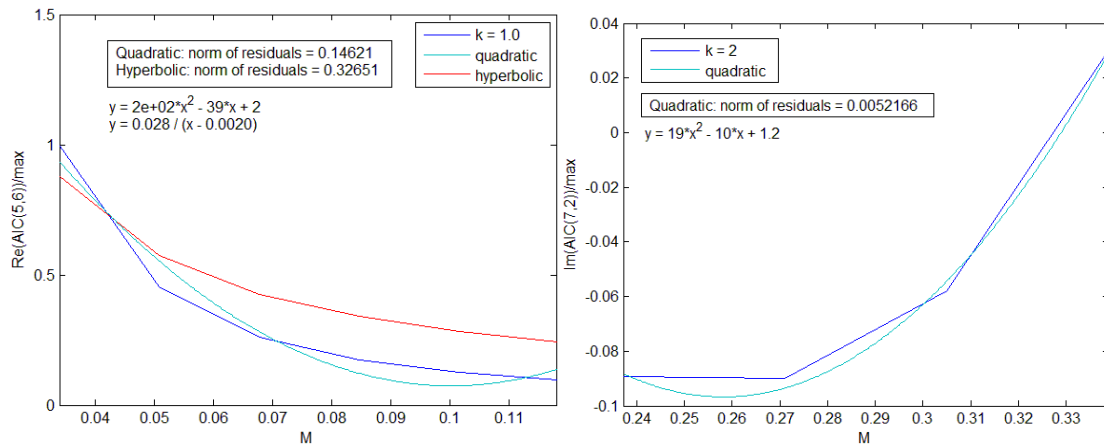
*Figure 44: quadratic (**left**) and hyperbolic (**right**) curve fittings applied to certain regions from the plots in Figure 43 with the corresponding residuals*

The two plots above are extractions from the plots in Figure 43 covering approximately a range of 0,1 Mach. The left plot depicts the low Mach number region for k=1. In this particular case the quadratic interpolation is actually better as can be seen by the shape of the curves and respective norm of residuals. The right plot depicts an higher Mach number region for k=2. The least squares fit with a 2nd degree polynomial are considered satisfactory therefore the curve may be well interpolated with this kind of function.

There is a lot of uncertainty concerning the type of interpolation functions and the length of the Mach step taken. In addition, for most frequencies of interest at a given Mach number, the velocity interpolation depends on several frequency interpolations performed at other Mach numbers. As a first insight about the system aeroelastic behavior, the speed interpolation might be usefull because it can sweep a wide range of Mach numbers extremely fast. However, if high accuracy is intended, such procedure should be avoided.

7 CODE VALIDATION

The validation of the code was performed by modelling a prototype high aspect ratio wing that has been extensively studied and reported in the open literature. An aeroelastic analysis was conducted in the exact same conditions as in the selected case study and the available results such as the flutter speed and respective mode frequency were compared.

7.1 CASE STUDY

The case study is the wing present in the paper by Patil *et al* [30]. In this work, the authors study the effect of initial deformation and angle of attack on the flutter speed of a high aspect ratio wing. The calculations were based on two complementary theories: a mixed variational formulation for beams in moving frames and finite-state airloads for deformable airfoils on fixed and rotating wings. Even though these theories are intrinsically non-linear, a preliminary linear analysis was performed in which the flutter speed was calculated for the undeformed wing. Since the structural model is compatible with the one dimensional beam model used in this thesis, and all the required structural data was provided, this case study was considered suitable for comparison and validation of the results obtained by the program. The structural and aerodynamic data is presented in Table 15.

7.1.1 Wing Model Data

Table 15: wing model input data required for performing the linear flutter analysis present in [30]

Geometry	
Half-span	16 m
Chord	1 m
Given Material Proprieties	
Mass per unit length, $\lambda = \rho_{wing} * b * h$	0.75 kg/m
Moment of Inertia (50% chord), $I = \frac{\lambda}{12}(b^2 + h^2)$	0.1 kg m
Spanwise elastic axis	50% chord
Center of Gravity	50% chord
Bending Rigidity, $EI_{xx} = E * I_{xx}$	2E4 N m²
Torsional Rigidity, $GJ = G * J$	1E4 N m²
Bending Rigidity (chordwise), $EI_{zz} = E * I_{zz}$	4E6 N m²
Calculated Structural Proprieties	
Equivalent beam width, $b = \left[12I\left(\lambda\left(1 + \frac{EI_x}{EI_z}\right)\right)^{-1}\right]^{\frac{1}{2}}$	1.262 m
Equivalent beam height, $h = b\sqrt{\frac{EI_x}{EI_z}}$	8.922E-2 m
Elastic Modulus, $E = \frac{12EI_x}{bh^3}$	267.823 MPa
Torsional Constant, $J \cong bh^3\left(\frac{1}{3} - 0.21\frac{h}{b}\left(1 - \frac{1}{12}\left(\frac{h}{b}\right)^4\right)\right)$	2.854E-4 m⁴
Shear Modulus, $G = \frac{GJ}{J}$	35.039 MPa
Flight Condition	
Altitude	20 km
Air Density	0.0889 kg/m³
Speed of Sound	295.1 m/s

7.1.2 Preliminary Modal Analysis

In order to validate the structural model, a modal analysis was performed using ANSYS® and the first five natural frequencies were extracted. The results are organized in Table 16:

Table 16: wing's first five natural frequencies calculated using ANSYS® and comparison with the same ones obtained in [30]

	Present Analysis	**Patil *et al* [30]**	**Relative Error (%)**
1st spanwise bending	2.243	2.247	-0.18
2nd spanwise bending	14.064	14.606	-3.71
1st chordwise bending	31.341	31.739	-1.25
1st torsion	31.523	31.146	1.21
3rd spanwise bending	39.445	44.012	-10.38

Despite the 3rd Spanwise bending, the frequencies are very similar with relative errors below 5%. Also, each frequency correspond to the same mode on either analysis. An exception occurs in the 3rd and 4th frequencies that seem to be swapped in position. However, since they are numerically very close, such may not be an issue concerning the following aeroelastic analysis.

7.1.3 Aeroelastic Results

This case study was simulated in MATLAB® with the mesh parameters based on the conclusions of the convergence study (see section 5.2.2.3). The first five natural frequencies were tracked for a wide range of flight speeds in search of the flutter boundary defined by the zero damping condition. Since no information was given about the angle of attack or the airfoil used, the angle of attack was set to zero and a symmetrical airfoil was chosen. The complete list of MATLAB® input parameters is shown in Table 17:

Table 17: input computational parameters used in MATLAB® for the present flutter analysis

Aeroelastic Analysis		
Angle of Attack	0	
Airfoil	NACA 0012	**Assumptions**
Critical Mach[5] (NACA 0012)	0.818	
"nseg_X"	12	
"nseg_Y"	128	**Mesh parameters**
"nseg_wake"	36	
"n_panels"	3132	
k-interpolation	Yes	**Interpolation Scheme**
M-interpolation	No	
"n_freqs"	5	
Mach step (Speed step)	0.0339 10 m/s	**Search Parameters & Computational Cost**
Mach range (Speed range)	[0.0339; 0.9149] (10; 270) m/s	
Mach Loops	27	
CPU time (equivalent time)	311631 seconds (3d 14h 33min 51s)	

The final results are depicted in Figure 45 and Figure 46:

---

[5] Critical Mach estimated using NACA 0012 in JavaFoil [45]
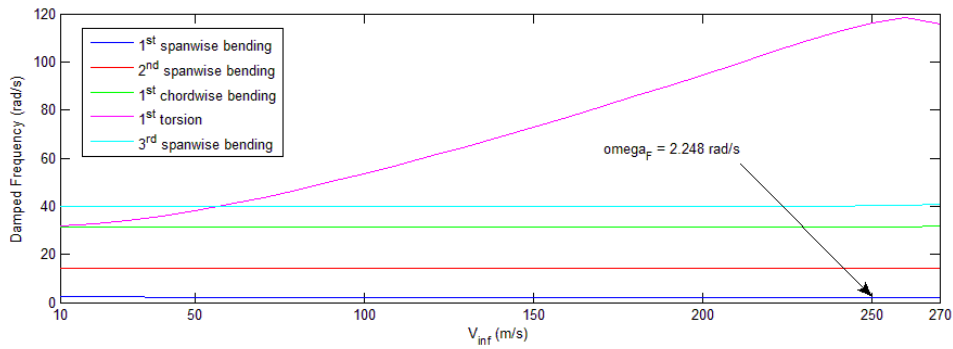
Figure 45: imaginary part of the dimensional part of "p" corresponding to the aeroelastic damped frequencies versus the flight speed
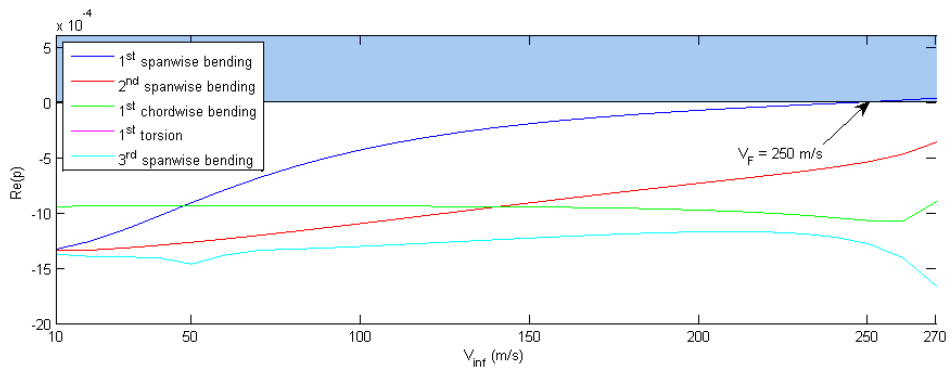

Figure 46: real part of "p" corresponding to the aeroelastic damping versus the flight speed

Table 18: aeroelastic results for both studies and comparison

	Present Study	Patil *et al* [30]	Relative Error (%)
Flutter speed U_F (M_F)	250 m/s (0.8472)	32.21 m/s	676.16
Flutter Frequency	2.243 rad/s (1st bending)	22.61 rad/s (?)	-90.08

7.1.4   Comments

In Figure 46 the blue region marks the instability zone where the damping is positive. The intersection of the instability zone with the damping curves defines the flutter speed and it is marked with an arrow. For this wing, the 1st bending mode (Figure 46 – blue curve) is the first mode to become unstable, occurring at a flight speed of 250 m/s. By inspecting Figure 45, the damped frequency corresponding to the 1st bending at 250 m/s is approximately 2.248 rad/s. However, these values are an order of magnitude above the ones obtained for the exact same wing by Patil *et al* (Table 18). In addition, the calculated flutter speed is clearly in the transonic regime which is beyond the linear scope of the theory in use. The results obtained so far have not been useful to validate the developed flutter code. There are several possible causes that could justify the discrepancy in the results. Consider the following:

1. **Number of modes**: in aeroelastic stability analysis, flutter occurs at the minimum speed at which one of the modes becomes unstable. It is possible (but very unlikely) that the first unstable mode is not one of the five modes tracked in this analysis. In his work, Patil *et al* only mention the value of the flutter frequency and not the type of its mode, but he does mention the same first five modes tracked by the current code. Therefore it was assumed that these modes were enough for correctly determining the flutter speed

2. **Airfoil selection**: being a tridimensional theory, the results also depend on the chosen airfoil. Provided that the airfoil is not too thick nor the camber too high, perturbations in the flow field remain small and the current linear theory should, in principle, still be adequate for predicting linear stability. Considering the magnitude of the error and the chosen thin and symmetrical NACA 0012 airfoil, this is believed to not be the source of the error

3. **Bad interpolation scheme**: in this calculation, the k-interpolation described in chapter 6.2.1.1 was used extensively for each Mach number. It may have happened that the interpolation functions were not accurate enough for predicting the AIC matrix over the reduced frequency range of interest for each speed. In the 3rd spanwise bending damping curve (light blue curve, Figure 46), there is an odd depression in the curve around 50 m/s which breaks the overall smooth behavior of the curve. This is most likely a consequence of a bad interpolation. However, this only happens for this mode which is most likely the least important concerning the flutter instability

4. **DoFs incompatibility**: since the structural mesh is one dimensional, and the aerodynamic mesh is two dimensional, a DoF compatibility relation was necessary. This has been accomplished using simple linear cinematic relations assuming a rigid connection between each panel and the nearest structural node. In addition, there was a need to resort to finite differences in order to estimate the aerodynamic rotations $\left(\frac{\partial u}{\partial x}, \frac{\partial v}{\partial x}, \frac{\partial w}{\partial w}\right)_A$ which are prone to numerical errors. If the connection between the two DoFs systems is not well established, the AIC matrix is directly affected resulting in erroneous results

5. **Theoretical formulation**: the theoretical foundation of the program is an integral equation (section 4.2.1) relating the aerodynamic potential φ and its normal derivative $\frac{\partial \varphi}{\partial n}$ on the physical boundaries of the system. While most of the theoretical is based on the text of reference [38], the complete methodology was unavailable thus leaving some technical details to be decided by the author of this thesis. Examples of these undefined aspects are the construction of the numerical matrices, the generation of the aerodynamic DoFs via the normal perturbation speed $\frac{\partial \varphi}{\partial n}$, and the (numerical) calculation of the source and doublet integrals

6. **Implementation errors**: the full MATLAB® and ANSYS® scripts containing the aeroelastic flutter code have been developed from scratch by the author of this thesis alone. Its development involved numerous stages from the definition of a quadrilateral panel to the assembly of the final AIC matrix. The code was reviewed, debugged and altered multiple times before its definitive form. However, there might be still some numerical irregularities resulting from the transition of the analytical expressions to the computational ones (implementation) that went undetected

Despite the unacceptable numerical error, there is a possibility of validating the program from a qualitative point of view. In another publication, Patil & Hodges [31] provided the unsteady pressure coefficient curve along the span for the same high aspect ratio wing. The same plot was obtained using the MATLAB® script and it is shown below for comparison (Figure 47):
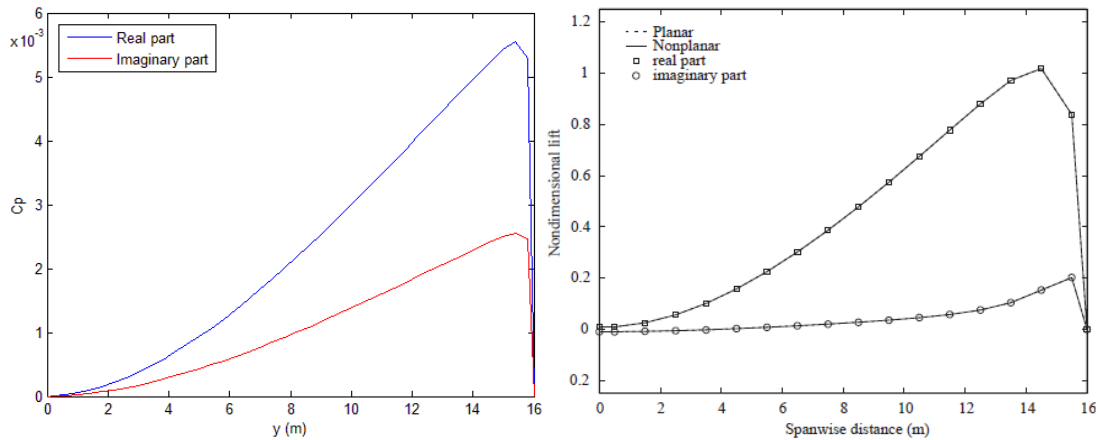
*Figure 47: spanwise unsteady lift corresponding to the 1st spanwise bending and k=0,4. The **left** plot was generated by the current analysis and the **right** one was extracted from reference [31]*

It is important to notice that despite the difference by several orders of magnitude, both real and imaginary parts behave similar in shape for the two analysis. The pressure increases slowly from zero at the wing root and drops quickly after the peak just before the wing tip. This similarity does support the qualitative value of the present work.

7.2 VALIDATION WITH THE STRIP THEORY

In order to gain access to other quantities and then attempt to further validate qualitatively the program, a new aeroelastic analysis of the same high aspect ratio wing has been performed resorting to a rather simpler approach – the strip theory (see chapter 4.1.1). This theory has been implemented in a new MATLAB® script with most of the algebraic formulas obtained using Wolfram Mathematica. The numerical aspects are summarized in Table 19:

Table 19: shape functions and numerical parameters required for performing the aeroelastic analysis using the Strip Theory in conjunction with the Rayleigh-Ritz method

Structural theory			
Model	1D elastic beam-rod		
Virtual displacements	Heave h_i and pitch α_i about the elastic axis		
Shape functions	$h_m(y,t) = \sum_{m=1}^{N_h} \left(\frac{y}{L}\right)^{m+1} \bar{h}_m(t)$ $\alpha_n(y,t) = \sum_{n=1}^{N_\alpha} \left(\frac{y}{L}\right)^{n} \bar{\alpha}_n(t)$		**Ritz method**
Number of shape functions	$N_h = 10$ $N_\alpha = 10$		
Input material proprieties (same as in the panel method)	**Bending rigidity**	EI_{xx}	
	Torsional rigidity	GJ	
	Wing density	λ	
Input geometrical proprieties (same as in the panel method)	**Chord**	c	
	Half span	L	
	Elastic axis	50% chord	
	Mass axis	50% chord	
	Aerodynamic axis	25% chord	
Aerodynamic theory			
Geometric model	2D infinite flat plate		**Strip theory**

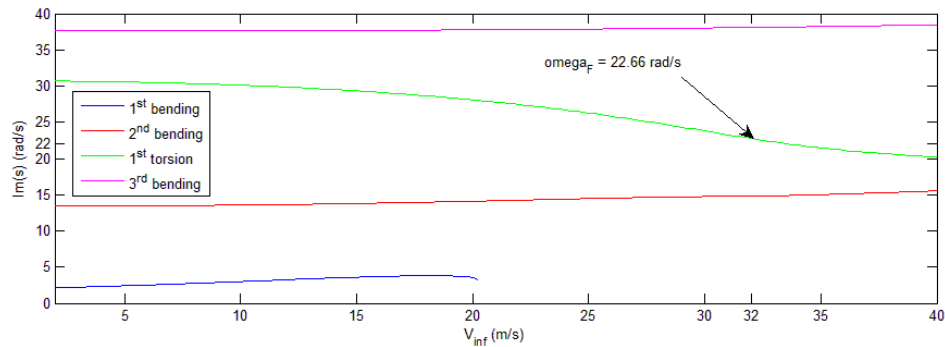|		
Flow model	2D incompressible potential flow	
Wake model	Infinite plain vortex wake	
Aeroelastic analysis		
Objective	Dynamic stability (flutter speed)	
Number of modes	4	
Speed range	[2,40] m/s	
Speed step	0,25 m/s	**Modified p-k**
Speed loops	153	**method**
k-interpolation	No	
V-interpolation	No	
CPU time	216s (3min 36s)	

Figure 48: imaginary part of the dimensional part of "p" corresponding to the aeroelastic damped frequencies versus the flight speed, calculated with the Strip Theory
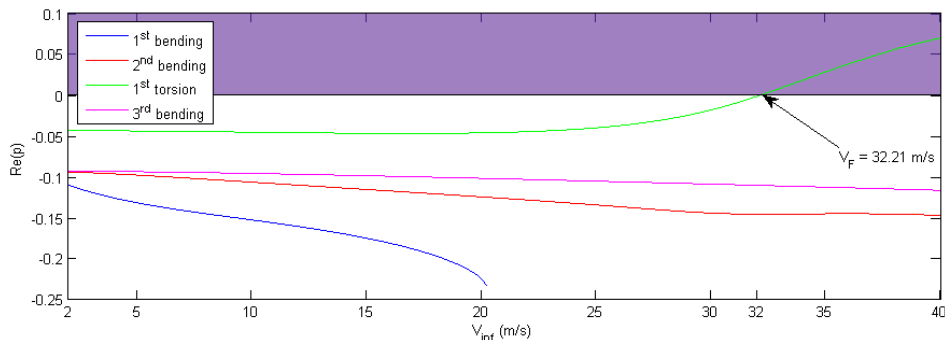

Figure 49: real part of "p" corresponding to the aeroelastic damping versus the flight speed, calculated with the Strip Theory

The plots in Figure 48 and Figure 49 depict the aeroelastic system's first four complex eigenvalues versus the mean airspeed, similar to the plots in Figure 45 and Figure 46 for the panel method. Even though Patil *et al* does not provide such plots for comparison, these results could be close candidates for them as one can infer after detecting the flutter boundary. This theory predicts flutter at $U_F = 32,2134 \text{ m/s}$ as a consequence of the instabillity of the 1st torsion mode with a damped frequency of $\omega_F = 22,6576 \text{ rad/s}$ and are approximately the numbers obtained by Patil in his linear aeroelastic analysis (Table 20).

Table 20: natural frequencies and aeroelastic results obtained by the implemented Strip Theory and comparison with the corresponding values from reference [30]

Structural Results	**Ritz method**	**Patil *et al* [30]**	**Relative Error (%)**
1st spanwise bending	2.243	2.247	-0.1780

2nd spanwise bending	14.056	14.606	-3.7656
1st chordwise bending	N.A.	31.739	N.A.
1st torsion	31.046	31.146	-0.3211
3rd spanwise bending	39.356	44.012	-10.5789
Aeroelastic Results	**Ritz Method + Strip Theory**	**Patil *et al* [30]**	**Relative Error (%)**
Flutter speed (m/s)	32.2134	32.21	0.0106
Flutter frequency (rad/s)	22.6576 (1st torsion)	22.61 (?)	0.2105

Unfortunately, there are few similarities between these results and the ones obtained for the developed panel method. Most importantly, the first instable mode is of a fundamentally different nature being a bending mode according to the panel method and a torsional mode according to the strip theory. Finally, for the sake of completeness, the lift and pitching moment along the span have been obtained and are depicted below:
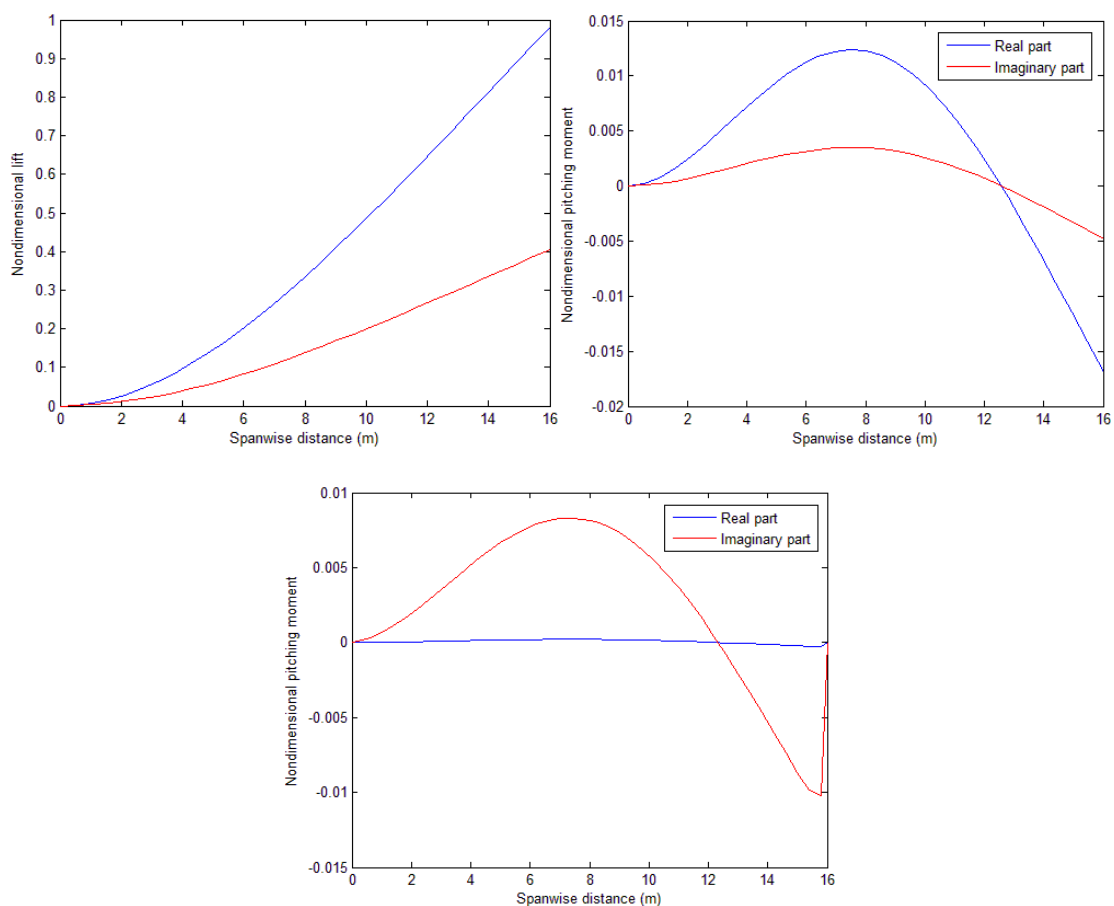

*Figure 50: non-dimensional unsteady lift and pitching moment per unit span calculated due to the 1st spanwise bending and k=0.4 in terms of the real (blue) and imaginary (red) parts. **Top left** – non-dimensional lift per unit span calculated with the Strip Theory. **Top right** – non-dimensional pitching moment per unit span calculated with the Strip Theory. **Bottom** – Non-dimensional pitching moment per unit span calculated with the developed aeroelastic code*

For the strip theory, both unsteady lift and moment spanwise distributions behave like the respective mode shape for the full length of the wing. It is important to stress out the absence of the drop to zero

at the wing tip observed in these plots as otherwise seen[6] in the panel method (Figure 47 left and Figure 50 bottom) and in the paper by Patil *et al* (Figure 47 right). Such behavior is expected since the strip theory is fundamentally two dimensional and the concept of a finite wing has not been taken into account. In the pitching moment plot obtained with the panel method (Figure 50 bottom), the 3D effects are less evident indicating that possibly a finer mesh was required near the wing tip.

---

[6] Actually, since the last structural node is not exactly at the wing tip, the value of the force and moment could not be obtained there and thus the value appearing at y = 16m have been enforced manually. However, the start of the declination to zero can be observed in the plots, for instance in the lift plot of Figure 47 – left side

8 CONCLUSION

A computational tool was developed with the purpose of determining the aeroelastic flutter speed of a 3D aircraft wing. The aeroelastic model was created based on the coupling of a structural model with an aerodynamic model. The structural model consisted in a one-dimensional beam-rod clamped at the aircraft fuselage, and representative of the wing elastic axis. The aerodynamics were modeled according to compressible potential fluid theory in which the pressure forces were calculated based on the 3D geometry of the wing. The methodology of solution consisted in a finite element approach centered at the structural nodes, involving the inertial, elastic and aerodynamic forces, expressed by the mass, stiffness and aerodynamic influence coefficients matrix (AIC), respectively. While mass and stiffness matrices were easily calculated using the finite element software ANSYS®, the AIC matrix was calculated by a panel method, developed and implemented in MATLAB® environment, constituting the main part of the current work. The developed panel method, originally presented by L. Morino [38], is formulated in the frequency domain and it is valid for subsonic flow around closed surfaces within the framework of small disturbances. The method is presented as an alternative to the usual linear flutter calculation methods, such as the DLM, allowing the study of more complex geometries, the inclusion of thickness effects, and free surface discretization schemes. Once the discretized aeroelastic equilibrium system of equations was established, the stability roots were extracted through an iterative process based on the p-k method. The *modified p-k method* was developed in this work in order to avoid losing the track of the correct mode after some frequency or velocity iterations, during the process of searching for the stability boundary.

To validate the computational framework, the linear flutter calculation of a high aspect ratio wing performed by Patil *et al* in [30] was simulated, and the frequency and flutter speed were calculated for comparison. However, even though flutter was evident after inspecting the results, the corresponding values of frequency and speed were far above the ones obtained in [30], with relative deviations around 700% and 90% respectively. In the preliminary modal analysis performed in ANSYS®, the values and types of natural frequencies obtained were similar to the ones provided in [30], suggesting that the error was originated in the aerodynamic calculations.

By comparing the non-dimensional spanwise lift plot with the one provided in [31] corresponding to the same wing (Figure 47), it was possible to notice strong similarities between the curves, indicating that the obtained results may have some qualitative significance. However, the numerical values still revealed great deviation from the reference.

As a way of confirming the source of the error, the same wing was modeled resorting to the Strip-Theory for the aerodynamics and Rayleigh-Ritz for the structure. Since the results were identical to the ones from reference [30], the validity of these results was confirmed and the cause of the discrepancies observed was attributed to possible errors in the developed program.

Among the multiple possible causes or error, the most probable might be related with the force and DoFs transformation from the aerodynamic nodes to the structural ones, seeing that the meshes were

different and the techniques used in this process were somewhat rudimentary. In addition, the code contains issues concerning the numerical efficiency as seen in the excessive computation time required for the validation study. The interpolation methods used were not effective enough to render multiple flutter calculations feasible using the mesh parameters imposed by the convergence study. This was mainly due to the lack of exact formulas for the integral coefficients, thus ending up being calculated exclusively by numerical means.

From a practical point of view, the developed tool did not bring any advantage over the usual methods used today for linear flutter calculation, namely the DLM or even the classical Strip Theory. These methods are known to produce accurate results in linear aeroelasticity and its multiple computer implementations over the last decades have made them superior in terms of efficiency.

From the academic point of view, considering the distinct and broader domain of applicability of the present method over others within the framework of potential aerodynamics, there might be interest in revisiting the methodology implemented in the present work. In a hypothetical future approach, the aspects concerning the theoretical formulation and the implementation procedures of the panel method should be reviewed in order to gain some additional insight about the nature of the errors and, if possible, to increase the overall efficiency.

As a final remark, it is important to stress that, within the field of research of aeroelastic stability, the present work did not constitute a new contribute but was rather an attempt to implement an existing methodology, while resorting to the limited available bibliographical resources. The occasional lack of information led to certain aspects of the implementation of the method to be defined by the author of this dissertation. In this sense, the success or failure of the present work relied heavily not only on the interpretation of the available information, but also on the ability to find solutions when this information revealed scarce.

9 REFERENCES

[1] I. E. Garrick and W. H. Reed III, "Historical Development of Aircraft Flutter," *AIAA Journal,* vol. 18, no. 11, pp. 897-912, 1981.

[2] F. W. Lanchester, "Torsional Vibrations of the Tail of an Aeroplane," *Advisory Committee for Aeronautics R&M 276,* vol. 1, 1916.

[3] L. Bairstow and A. Fage, "Oscillations of the Tail Plane and Body of an Aeroplane," *Advisory Committee for Aeronautics R&M 276,* vol. 2, 1916.

[4] A. G. von Baumhauer and C. Koning, "On the Stability of Oscillations of an Airplane Wing," *NACA TM 223,* 1923.

[5] W. Birnbaum, "Das Ebene Problem des Schlagenden Flügels," *ZAMM,* vol. 4, pp. 277-292, 1924.

[6] H. Wagner, "Dynamische Auftrieb von Tragflügeln (Dynamic Lift of Wings)," *ZAMM,* vol. 5, pp. 17-35, 1925.

[7] H. Glauert, "The Force and Moment of an Oscillating Airfoil," *Advisory Committee for Aeronautics R&M 1242,* 1929.

[8] T. Theodorsen, "General Theory of Aerodynamic Instability and the Mechanism of Flutter," *NACA Report,* vol. 496, 1935.

[9] E. H. Dowell, H. C. Curtiss, R. H. Scanlan and F. Sisto, A Modern Course in Aeroelasticity, Alphen aan den Rijn, The Netherlands: Sijthoff & Noordhoff, 1978.

[10] L. Prandtl, "Wing Theory in a Compressible Medium," *Luftfahrtforschung,* vol. 13, pp. 313-319, 1936.

[11] C. Possio, "Aerodynamic Forces on an Oscillating Profile in a Compressible Fluid at Subsonic Speeds," *Aerotecnica,* vol. 18, pp. 441-458, 1938.

[12] H. G. Küssner, "General Airfoil Theory," *NACA TM-979,* 1941.

[13] C. E. Watkins, H. L. Runyan and D. L. Woolston, "On the Kernel Function of the Integral Equation Relating the Lift and Downwash Distributions of Oscillating Finite Wings in Subsonic Flow," *NACA TN-3131,* 1954.

[14] R. L. Bisplinghoff and H. Ashley, "Lifting Surfaces and Other Configurations in Three-Dimensional Unsteady Flow; Simple Harmonic Motion," in *Principles of Aeroelasticity*, Dover, 1962, pp. 125-130.

[15] E. Albano and W. P. Roddden, "A Doublet Lattice Method for Calculating the Lift Distributions on Oscillating Surfaces in Subsonic Flows," *AIAA Paper, No. 68-73,* pp. 1-12, 1968.

[16] H. T. Vivian and L. V. Andrew, "Unsteady Aerodynamics for Advanced Configurations. Part I - Application od the Subsonic Kernel Function to Nonplanar Lifting Surfaces," *Air Force Flight Dynamics Lab. Report FDL-TDR-64-152,* vol. I, 1965.

[17] MSC.Software Corporation, "MSC.Nastran Version 68 - Aeroelastic Analysis User Guide," 2004.

[18] J. L. Hess and A. M. O. Smith, "Calculation of Potential Flow About Arbitrary Bodies," *Progress in Aeronautical Sciences,* vol. 8, pp. 1-138, 1966.

[19] J. Katz and A. Plotkin, "Unsteady Panel Methods," in *Low-Speed Aerodynamics - From Wing Theory to Panel Methods*, McGraw-Hill, 1991, pp. 495-502.

[20] K. D. Jones and M. F. Platzer, "Time-Domain Analysis of Low-Speed Airfoil Flutter," *AIAA Journal,* vol. 34, pp. 1027-1033, 1996.

[21] J. N. Reddy, "The Ritz Method," in *An Introduction to the Finite Element Method*, McGraw Hill, 2006, pp. 74-76.

[22] C. Hirsch, "The Runge-Kutta Methods," in *Numerical Computation of Internal and External Flows Vol. 1*, John Wiley & Sons, Ltd, 2007, pp. 458-460.

[23] C. Farhat, "AA242B: Mechanical Vibrations - Direct Time-Integration Methods," Stanford University, California, 2014.

[24] J. R. Wright and J. E. Cooper, Introduction to Aircraft Aeroelasticity and Loads, West Sussex, England: John Wiley & Sons Ltd., 2007.

[25] Zona Technology Inc, "Spline Methods for Spline Matrix Generation," in *ZAERO Theoretical Manual 8.5*, 2011, pp. 156-178.

[26] R. L. Harder and R. N. Desmarais, "Interpolation Using Surface Splines," *AIAA Journal,* vol. 9, pp. 189-191, 1972.

[27] D. H. Hodges and G. A. Pierce, Introduction to Structural Dynamics and Aeroelasticity, New York: Cambridge University Press, 2011.

[28] R. H. Scanlan and R. Rosenbaum, "Outline of an Acceptable Method of Vibration and Flutter Analysis for a Conventional Airplane," Airframe and Equipment Engineering Report No. 43, Washington, D.C., USA, 1948.

[29] H. J. Hassig, "An Approximate True Damping Solution of the Flutter Equation by Determinant Iteration," *AIAA Journal,* vol. 8, no. 11, pp. 885-889, 1971.

[30] M. J. Patil, D. H. Hodges and C. E. S. Cesnik, "Nonlinear Aeroelasticity and Flight Dynamics of High-Altitude Long-Endurance Aircraft," *AIAA Journal,* vol. 38, pp. 88-94, 2001.

[31] M. J. Patil and D. H. Hodges, "On the Importance of Aerodynamic and Structural Geometrical Nonlinearities in Aeroelastic Behavior of High-Aspect-Ratio Wings," *Journal of Fluids and Structures,* vol. 19, pp. 905-915, 2004.

[32] C. Xie and C. Yang, "Linearization Method of Nonlinear Aeroelastic Stability for Complete AIrcraft with High-Aspect-Ratio Wings," *Science China - Technological Sciences,* vol. 54, no. 2, pp. 403-411, 2011.

[33] O. O. Bendiksen, "High-Altitude Limite Cycle Flutter of Transonic WIngs," *AIAA Journal,* vol. 46, pp. 123-136, 2009.

[34] W.-k. Gao, "Numerical Simulation of a 3-D Wing Flutter in Time Domain," *Journal of Astronautics (China),* vol. 29, no. 4, pp. 1153-1156, 2008.

[35] M. Bhatia and P. Beran, "Higher-Order Transonic Flutter Solutions," *AIAA SciTech, 55th AIAA/ASMe/ASCE/AHS/SC Structures, Structural Dynamics, and Materials Conference,* pp. 1-14, 2014.

[36] H. A. Carlson, R. Verberg, J. A. Lechniak and K. Bhamidpati, "Flutter Prediction with a Reduced-Order Aeroelastic Model," *50th AIAA Aerospace Sciences Meeting including the New Horizons Forum and Aerospace Exposition,* pp. 1-8, 2012.

[37] K. L. Lai, X. Q. Zhang and T. Kim, "Numerical Study of Effect of Control Surface on Wing Flutter in Transonic Flow," *AIAA,* 2014.

[38] L. Morino, "NASA CR - 2464: A General Theory of Unsteady Compressible Potential Aerodynamics," Langley Research Center, Hampton, Virgina, 1974.

[39] K. Watanabe, "Green's Functions for Laplace and Wave Equations," in *Integral Transform Techniques for Green's Function*, Springer International Publishing, 2014, pp. 11-42.

[40] E. C. J. Yates, H. J. Cunningham, R. N. Desmarais, W. A. Silva and B. Drobenko, "NASA TM-84485: Subsonic Aerodynamic and Flutter Characteristics of Several Wings Calculated by the SOUSSA P1.1 Panel Method," Langley Research Center, Hampton, Virginia, 1982.

[41] H. J. Cunningham, "NASA TP-2736: Steady and Unsteady Aerodynamic Forces from the SOUSSA Surface-Panel Method for a Fighter Wing with Tip Missile and Comparison with Experiment and PANAIR," Langley Research Center, Hampton, Virginia, 1987.

[42] Ü. Gülçat, Fundamentals of Modern Unsteady Aerodynamics, Maslak, Istanbul, Turkey: Springer-Verlag, 2010.

[43] ANSYS, Inc., "ANSYS Mechanical APDL Structural Analysis Guide," Canonsburg, PA, USA, 2012.

[44] ANSYS, Inc., "ANSYS Mechanical APDL Theory Reference," Canonsburg, PA, USA, 2012.

[45] M. Hepperle, "JavaFoil - Analysis of Airfoils," MH-AeroTools, 2007. [Online]. Available: http://www.mh-aerotools.de/airfoils/javafoil.htm. [Accessed 2014].

APPENDIX A

The method involved in the calculation of the singular source integral is presented here. Consider the following integral, representing the influence of an unsteady source singularity distribution over a flat panel:

$$I_S^Q = \iint \frac{e^{-s_0 r_0}}{r_0} dS_0 = \iint \frac{e^{-s_0\sqrt{(X_Q-x_0)^2+(Y_Q-y_0)^2+(Z_Q-z_0)^2}}}{\sqrt{(X_Q - x_0)^2 + (Y_Q - y_0)^2 + (Z_Q - z_0)^2}} dS_0 \qquad (136)$$

Originally, the Cartesian coordinates are expressed in the transformed global coordinate system. However, being an integral quantity, the integral may be performed in any convenient coordinate system. The logic choice is to use the panel local transformed coordinate system with origin at its centroid. For the current self-influencing case, this choice allows point Q to vanish in the integrand along with the coordinate z_0. In addition, the differential dS_0 is now expressed in terms of the integration variables given by $dx_0 dy_0$. The simplified integral takes the following form:

$$I_S = \iint \frac{e^{-s_0\sqrt{x_0^2+y_0^2}}}{\sqrt{x_0^2 + y_0^2}} dx_0 dy_0 \qquad (137)$$

It is still not possible to evaluate the integral exactly. Also, the singularity is still present within the domain of integration which prevents an efficient numerical integration. It is shown next that a conversion to polar coordinates eliminates the singularity:

$$x_0 = r\cos\theta, y_0 = r\sin\theta \qquad (138)$$

$$|\mathbf{J}| = r \qquad (139)$$

After the coordinate transformation the integral becomes:

$$I_S = \iint \frac{e^{-s_0 r}}{r} r dr d\theta = \iint e^{-s_0 r} dr d\theta \qquad (140)$$

This integrand is defined in every point inside the panel domain allowing any integration scheme to be used. The integration in the radial coordinate can be evaluated exactly by integrating from $r = 0$ to $r = R(\theta)$:

$$I_S = \int_0^{2\pi} \left(\int_0^{R(\theta)} e^{-s_0 r} dr \right) d\theta = \frac{2\pi}{s_0} - \frac{1}{s_0} \int_0^{2\pi} e^{-s_0 R(\theta)} d\theta \qquad (141)$$

The symbol $R(\theta)$ represents the radial distribution of the panel boundaries in terms of the angular coordinate θ. Due to the triangular or quadrilateral shape of the panels, the function $R(\theta)$ must be defined by three or four branches respectively. In Cartesian coordinates, each side of the panel is given by 1st order polynomials:

$$y_i(x) = m_i x + b_i, \quad i = 1, \ldots, 3 \text{ or } 4 \tag{142}$$

$$x = x_i, \quad m_i \to \infty \tag{143}$$

The subscript "i" refer to the 3 or 4 corners of the panel (Figure 51). For instance, m_2 refers to the slope of the side connecting corners number 2 and 3 of the panel. The corresponding boundary functions in polar coordinates are given by:

$$R_i(\theta) = \frac{b_i}{\sin\theta - m_i \cos\theta} \tag{144}$$

$$R_i(\theta) = \frac{x_i}{\cos\theta}, \quad m_i \to \infty \tag{145}$$

After replacing $R(\theta)$ in equation (141) by the above generic formulas, the integral can be evaluated by any standard numerical rule.

$$I_S = \frac{2\pi}{s_0} - \frac{1}{s_0} \sum_{i=1}^{N} \int_{\theta_i}^{\theta_{i+1}} e^{-s_0 \frac{b_i}{\sin\theta - m_i \cos\theta}} d\theta, \quad N = 3 \text{ or } 4 \tag{146}$$
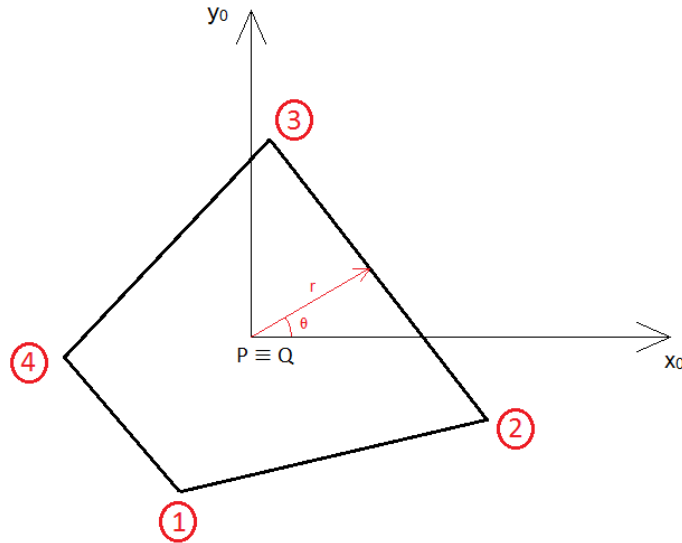

Figure 51: generic quadrilateral panel with local Cartesian and polar coordinate systems. Point Q is placed at point P indicating a self-influence case (singular integral)

This procedure not only eliminates the singularity, but reduces the surface integral to a line integral, therefore significantly reducing the computational cost. As a final remark, it should be noted that the above formulas are only valid for the self-influence case, where the origin of the local coordinate system coincides with point Q.

APPENDIX B

The doublet singular integral is treated here. The influence of an unsteady doublet singularity distribution over a panel on a certain point Q is given by the following integral:

$$I_D^Q = \iint \frac{\partial}{\partial n_Q}\left(\frac{e^{-s_0 r_0}}{r_0}\right) dS_0 = \iint \frac{\partial}{\partial n_Q}\left(\frac{e^{-s_0\sqrt{(x_Q-x_0)^2+(y_Q-y_0)^2+(z_Q-z_0)^2}}}{\sqrt{(x_Q-x_0)^2+(y_Q-y_0)^2+(z_Q-z_0)^2}}\right) dS_0 \tag{147}$$

In general, the above integral has no exact solution and can only be approximated using numerical methods. However, in the self-influence case where point Q is inside the integration limits, the integral becomes singular at that point and numerical methods become highly inefficient. The procedure used here follows a similar approach presented in Appendix A for the source singular integral. It is shown in this appendix that a suitable coordinate transformation can remove the singularity and that ultimately the integral can be evaluated exactly, thus excluding the need of a numerical integration scheme.

Consider the transformed local Cartesian coordinate system with origin at point P, the centroid of the influencing panel. In the self-influence case, the influenced point Q is coincident with point P thus creating a singularity at this point, given by $(x_0, y_0, z_0)_P = (0,0,0) = (x_Q, y_Q, z_Q)$. In this coordinate system, the normal direction is also the vertical z_0 direction so that the derivative can be evaluated directly. Formally, since $z_Q = 0 = z_0$ over the panel surface, the integral being sought can be evaluated by solving the following limit:

$$I_D^Q = \lim_{z_Q \to 0}\left[\iint \frac{\partial}{\partial z_Q}\left(\frac{e^{-s_0\sqrt{(x_Q-x_0)^2+(y_Q-y_0)^2+(z_Q-z_0)^2}}}{\sqrt{(x_Q-x_0)^2+(y_Q-y_0)^2+(z_Q-z_0)^2}}\right) dx_0 y_0\right]_{x_Q=y_Q=z_0=0} =$$

$$= \lim_{z_Q \to 0}\iint -z_Q \frac{e^{-s_0\sqrt{x_0^2+y_0^2+z_Q^2}}}{\left(x_0^2+y_0^2+z_Q^2\right)^{\frac{3}{2}}}\left(1+s_0\sqrt{x_0^2+y_0^2+z_Q^2}\right) dx_0 dy_0 \tag{148}$$

Choosing the polar coordinates (r, θ):

$$x_0 = r\cos\theta, y_0 = r\sin\theta \tag{149}$$

$$|\mathbf{J}| = r \tag{150}$$

The integral becomes:

$$I_D^Q = \lim_{z_Q \to 0}\iint -z_Q \frac{e^{-s_0\sqrt{r^2+z_Q^2}}}{\left(r^2+z_Q^2\right)^{\frac{3}{2}}}\left(1+s_0\sqrt{r^2+z_Q^2}\right) r\,dr\,d\theta \tag{151}$$

Another convenient transformation is the following:

$$R^2 = r^2 + z_Q^2 \Leftrightarrow r = \left| \sqrt{R^2 - z_Q^2} \right| \tag{152}$$

$$dr = \frac{R}{\sqrt{R^2 - z_Q^2}} dR \tag{153}$$

Simplifying the integral in equation (151) to:

$$I_D^Q = \lim_{z_Q \to 0} \iint -z_Q \frac{e^{-s_0 R}}{R^2} (1 + s_0 R) dR d\theta \tag{154}$$

The integrand is similar to the one from the singular source integral except for denominator R^2 or R which prevents any exact integral evaluation. It is possible to go further by expanding the exponential term in an infinite series:

$$e^{-s_0 R} = \sum_{n=0}^{\infty} \frac{(-s_0 R)^n}{n!} \tag{155}$$

After some algebra, retaining the terms up to order 2, the integral becomes:

$$I_D^Q = \lim_{z_Q \to 0} \int_0^{2\pi} \int_{z_Q}^{\sqrt{r^2(\theta) + z_Q^2}} -z_Q * \left(\frac{1}{R^2} - \frac{1}{2} s_0^2 + \frac{1}{3} s_0^3 R - \frac{1}{6} s_0^4 R^2 + O(R^3) \right) dR d\theta \tag{156}$$

It is clear from equation (156) that all the integrals over the radial coordinate are immediate for they can be solved exactly according to the formula:

$$I = \int_{z_Q}^{\sqrt{r^2(\theta) + z_Q^2}} -z_Q * cte(n) * R^m dR = -z_Q * cte(n) * \left[\frac{R^{m+1}}{m+1} \right]_{z_Q}^{\sqrt{r^2(\theta) + z_Q^2}} \tag{157}$$

$$m \in \mathbb{N}^0 \cup \{-2\}, \quad n = m + 2 \tag{158}$$

Then the limit becomes:

$$I_D^Q = \lim_{z_Q \to 0} \int_0^{2\pi} -z_Q * \sum_{n=0}^{\infty} \frac{cte(n)}{m+1} \left[\left(r^2(\theta) + z_Q^2 \right)^{\frac{1}{2}(m+1)} - z_Q^{m+1} \right] d\theta \tag{159}$$

The integral in θ can be performed term by term by moving the integral inside the infinite series. In addition, since the limit does not concerns the index "n" of the series, nor the integration parameter "m", the limit operator can also be calculated term by term by placing it inside the series. There are two different limits to be performed:

$$L_1 = \lim_{z_Q \to 0} \int_0^{2\pi} -z_Q * \left(r^2(\theta) + z_Q^2 \right)^{\frac{1}{2}(m+1)} d\theta \tag{160}$$

$$L_2 = - \lim_{z_Q \to 0} \int_0^{2\pi} -z_Q * z_Q^{m+1} d\theta \tag{161}$$

The limit operator can be interchanged with the integral operator provided that the integrand is bounded for all $\theta \in [0, 2\pi]$. The function $r^2(\theta)$ represents the radial distribution of the boundaries of the panel for

a coordinate system centered at the panel's centroid. This function is a positive number limited by the panel boundaries therefore it is bounded. Since the remaining parameters are constant and $z_Q \to 0 \neq r^2(\theta)$, no singularities are possible. This means that for any "m", the integrands are bounded and the limit can interchange with the integral operator. Consider the following cases for "m":

$$m \geq 0: \begin{cases} L_1 = \int_0^{2\pi} \lim_{z_Q \to 0} -z_Q * \left(r^2(\theta) + z_Q^2\right)^{\frac{1}{2}(m+1)} d\theta = \int_0^{2\pi} 0 * \left(r^2(\theta) + 0\right)^{\frac{1}{2}(m+1)} d\theta = 0 \\ \\ L_2 = -\int_0^{2\pi} \lim_{z_Q \to 0} z_Q * z_Q^{m+1} d\theta = -\int_0^{2\pi} 0 * 0^{m+1} d\theta = 0 \end{cases} \tag{162}$$

$$m = -2: \begin{cases} L_1 = \int_0^{2\pi} \lim_{z_Q \to 0} \dfrac{-z_Q}{\sqrt{r^2(\theta) + z_Q^2}} d\theta = \int_0^{2\pi} \lim_{z_Q \to 0} \dfrac{-1}{\sqrt{\left(\dfrac{r(\theta)}{z_Q}\right)^2 + 1}} d\theta = \int_0^{2\pi} \dfrac{-1}{\infty} d\theta = 0 \\ \\ L_2 = -\int_0^{2\pi} \lim_{z_Q \to 0} -z_Q * \dfrac{1}{z_Q} d\theta = -\int_0^{2\pi} -1 * d\theta = 2\pi \end{cases} \tag{163}$$

As can be seen, only the second limit L_2 provides a result different than zero that occurs when $m = -2$. The respective multiplicative constant $\frac{cte(0)}{-2+1}$ resulting from equation (159) is equal to -1, as can be inferred from the series expansion in equation (156) and the integral formula in equation (157). Therefore, the final result for the singular doublet integral is simply:

$$I_D^Q = -2\pi \tag{164}$$

This concludes the calculation of the singular doublet integral.